Università degli Studi di Ferrara

DOCTORAL COURSE IN ENGINEERING SCIENCE
"SCIENZA DELL'INGEGNERIA"

CYCLE XXXV

DIRECTOR Prof. Stefano Trillo

Metallurgical characterizations of 17-4 PH and WC-Co hard facing Laser-based Direct Energy Depositions: effect of process parameters and post-fabrication heat treatments

Scientific/Disciplinary Sector (SDS) ING-IND/21

Candidate
Dott. Cindy E. Morales Bazaldua

_____
(Signature)

Supervisor
Prof. Gian Luca Garagnani

_____
(Signature)

Co-Supervisor
Prof. Mattia Merlin

_____
(Signature)

Years 2019/2022

DEDICATION

Dedicated to Mommy and Daddy, my siblings,
BRRV and Xana Do

To God

ABSTRACT

Direct Energy Deposition (DED) process is one of the most widespread additive manufacturing (AM) techniques that, in addition to the Powder Bed Fusion (PBF) processes, is commonly used to fabricate metal parts. DED is an AM process in which a focused thermal energy source (e.g., a laser) is used to fuse materials, in the form of powder of wires, by melting them while they are being deposited. This AM technique can be used to build hard-facing coatings onto desired metal substrates of to fabricate near-net-shape metal parts. Hence, this process is also typically used to repair, restore, or add additional material to existing components, so enabling the maximum flexibility to manufacture complex and high-quality parts without using costly and time-consuming conventional processes. Considering these advantages, DED is widely and successfully employed in several industrial fields, such as biomedical, aerospace, automotive, machinery, and tooling.

Among the increasing number of materials that can be processed by AM techniques, high-resistant alloys such as the 17-4 PH stainless steel and WC-12Co are mainly processed by PBF and Binder Jetting (BJ) techniques. The DED process could also be a feasible technique suitable to be used with the above-mentioned materials, allowing to achieve good results in terms of both microstructural and mechanical properties. Nevertheless, the literature is quite scarce on this topic.

Considering the high number of parameters that need to be controlled in the DED process, it is important to deeply understand the effect of the heat source, the scanning strategy, the scanning speed, and the powder or wire feed rate on macro and microstructural features as well as the mechanical behavior of the processed material to guarantee the fabrication of good-quality metal parts.

Hence, the present Ph.D. investigation deals with the characterization of depositions fabricated by Laser-based Direct Energy Deposition (L-DED) in two different materials: the 17-4 PH stainless steel and the WC-12Co cermet. Geometrical features of the depositions, as well as their microstructural and mechanical behavior, were studied to establish the best process conditions, suitable for achieving appropriate industrial requirements. The results demonstrated that, in both cases, the complex microstructure of the depositions and hence their mechanical behavior are highly influenced and controlled by the laser power parameters.

Concerning the 17-4 PH stainless steel, the results showed that when the highest laser energy density values are used, effective improvements in the microstructure in terms of distribution, homogenization, and size of the main phases can be obtained. To better understand the effect of precipitation hardening in 17-4 PH stainless steel deposited by DED, different heat treatment routes were investigated and compared to the most common H900 treatment. The applied post-fabrication heat treatments demonstrated that a direct aging route can be successful in enhancing the hardness of the materials by taking advantage of the level of saturation of the hardening elements.

The analysis of the WC-Co specimens showed that the laser power parameter and the volumetric energy density factor have a strong effect on the distribution, re-precipitation, and dissolution of the main phases in the deposited material. The proper selection of these parameters is extremely important for the hardness evolution of the material. Besides that, the scanning strategy was detected as critical among the selected process parameters because it was identified as the main responsible for porosity formation and thus influencing the microstructure and the hardness behavior of the samples.

SOMMARIO

Il processo denominato *Direct Energy Deposition* (DED) è una delle tecniche di manifattura additiva che, assieme ai processi a letto di polve (PBF), è comunemente impiegato per fabbricare parti in materiale metallico. La tecnologia DED prevede l'utilizzo di una sorgente termica (es: un laser) per fondere un materiale che viene fornito sotto forma di polvere o filo e che fonde mentre viene depositato. Questa tecnica può essere utilizzata per realizzare rivestimenti duri su substrati metallici o per fabbricare parti di geometria prossima a quella finale. Per tale ragione, il processo è tipicamente impiegato per riparare, ripristinare o aggiungere materiale a componenti esistenti. Si tratta di un processo molto flessibile per la realizzazione di parti complesse e di elevata qualità, prevenendo l'utilizzo di processi convenzionali costosi ed onerosi in termini di tempo. Considerando questi vantaggi, il processo DED è impiegato con successo in molti ambiti industriali, come ad esempio quelli biomedicale, aeronautico, *automotive*, della meccanica e dell'utensileria.

All'interno del panorama dei materiali che oramai vengono processati con tecniche di manifattura additiva, le leghe ad alta resistenza come l'acciaio inossidabile 17-4 PH e il metallo duro WC-Co sono utilizzati principalmente in processi sia a letto di polvere (PBF) sia *Binder Jetting* (BJ). Anche il processo DED potrebbe essere utilizzato altrettanto efficacemente con entrambi questi ultimi materiali, consentendo di ottenere ottimi risultati in termini di caratteristiche meccaniche e microstrutturali. Tuttavia, le informazioni disponibili in letteratura sono piuttosto scarse. Considerato l'elevato numero di parametri che devono essere controllati in un processo DED, diventa fondamentale conoscere in maniera approfondita l'effetto che può essere generato della sorgente termica, da entrambe la strategia e la velocità di scansione, e dalla velocità di apporto della polvere o del filo sulle caratteristiche sia meccaniche sia macro e microstrutturali del materiale al fine di produrre dei componenti di buona qualità.

In quest'ottica, il presente lavoro di tesi ha riguardato la caratterizzazione di deposizioni in acciaio inossidabile 17-4 PH e in metallo duro WC-12Co realizzate mediante tecnologia DED avente un laser come sorgente termica. Per stabilire le migliori condizioni di processo in grado di soddisfare appropriati requisiti industriali, sono state indagate sia le caratteristiche geometriche delle deposizioni sia il loro comportamento meccanico e le caratteristiche microstrutturali. Per entrambi i materiali, i risultati hanno dimostrato che la complessa microstruttura tipica di queste deposizioni, e di conseguenza le loro caratteristiche meccaniche, sono fortemente influenzate e controllate dai parametri del laser.

Per quanto riguarda l'acciaio inossidabile 17-4 PH i risultati mostrano che è possibile ottenere miglioramenti della microstruttura in termini di distribuzione, omogeneizzazione e dimensione delle principali fasi, qualora vengano utilizzati valori elevati della densità di energia. Inoltre, per comprendere l'effetto della precipitazione sull'indurimento dell'acciaio 17-4 PH, sul materiale depositato sono stati eseguiti dei trattamenti termici utilizzando parametri sia analoghi sia sperimentali rispetto al convenzionale trattamento denominato H900. I risultati hanno mostrato che, sfruttando il livello elevato di sovrasaturazione degli elementi di lega che caratterizza il materiale allo stato di fabbricazione, l'invecchiamento diretto è una efficace alternativa al fine dell'incremento di durezza del materiale stesso.

Le analisi effettuate sui campioni in WC-12Co hanno dimostrato che la potenza del laser e la densità volumetrica di energia hanno un notevole effetto sulla distribuzione, ri-precipitazione e dissoluzione delle principali fasi presenti nel materiale depositato. La selezione dei due parametri citati risulta importante per controllare l'evoluzione della durezza del materiale. Tuttavia, anche la velocità di scansione è stata individuata come parametro potenzialmente critico in quanto influenza in modo sensibile il contenuto di porosità e di conseguenza anche la durezza e la microstruttura dei campioni.

ACKNOWLEDGEMENTS

My most sincere gratitude is to the Metallurgy Group of this university for letting me be part of their family, work, learn, and grow with them. I would like to enormously thank the head of this research group Prof. Gian Luca Garagnani for giving me one of the most precious opportunities of my life, as well as for the kindness and support during the last few years. *Dear Prof Garagnani: thank you, are two words that don't do justice to the gratitude that I have for you.* Secondly, I would like enormously to thank my second advisor Prof. Mattia Merlin, *Prof. I have no words that express how thankful I am for all the support, knowledge, and guidance you gave me during these years, really BIG BIG thank you.* Thirdly I would like to thank Annalisa Fortini, who during these years has supported me and helped me with no doubt during my academic formation, and beyond. *Sincerely a massive thank you*. And lastly (but not least) I would like to thank Enrico Baroni and Chiara Soffritti, for all the hearings, the friendship, and in general the support given during any and each topic I asked for.

I would like to continue this acknowledgment page by describing a little bit of the background of this journey. As you must know dear reader, I am a foreign student far away from home (9647 km, to be exact) with dreams of growing and learning. You should know that leaving my small town to move to another side of the world, is rough… but also my decision. When I arrived in this country, I did not know anyone, I had zero language knowledge, and to be honest, had tons of uncertainty for the time ahead. However, almost three years later I can say that ALL was worth it, the effort, the hard work, the loneliness, the learning, the growth, the independence, all of it.

For this, for all my past and my future, I would like to acknowledge and dedicate this work to my whole family, even if I know you will never read this, I am extremely grateful for your support, your prayers, and your love GRACIAS. Special thanks to my parents, who against their opinions always and desires support me with all my craziness; to my sisters and brothers, especially to Jody and Nana who support me as nobody else at home. To my niece and nephews that light each Saturday from home, *you should know guys that…nada es imposible.* To my mochi, as I always tell you… even if we don't speak the same language and it seems that I leave you behind, believe me, this is for you, for us, you are always in my mind and my heart Xana.

I would also like to thank my friends here and there, near and far. I am grateful for you, the laughs, the highs, the lows, and the time you gave me to cheer me up when I was feeling blue, especially Laura, Kristell, and my great Mexican friends here in Italy, Edith, and Carlos. What would have done without your support?

I want to dedicate some words to Anna Salò with accent in the ò, I want to say thanks for all; you were with me in the darkest times, and I hope to find you always in the brightest ones il mio Gryffindor preferito. I am so happy and grateful to find you on this journey.

Write this thesis without dedicating also to the Dra. Argelia Miranda is unacceptable because without her inspiration it will never cross my mind to do a Ph.D. abroad, thank you for the support, the advice, and the friendship, you will always be part of my life.

Last but not least I would like to dedicate this as all my academic formation, falls, and achievements, as well as my wins and losses to a very special person, the closest to my heart, my eternal partner, BRRV. It is unnecessary to try to explain how your paper is herein.

You know me better than I know myself, I am eternally thankful for always being unconditionally there when nobody else is, for your love and support, but also for encouraging me to do my best, even when I cannot do it anymore. This is for you, for us ♥.

And here we are, dear reader, this is how my small academic career story ends, or better… starts because this is just the beginning. I am in here behind this computer, trying to hold on to my tears finishing one of the biggest challenges in my personal and academic life.

I remain with the knowledge, the braveness, the experience but also, with the friendship, and the kindness of each person I met during these last years.

As always **don't forget** to *treat people with kindness.*

EXTENDED PREFACE

This Ph.D. thesis collects the activities carried out during the doctoral period, from November 2019 to January 2023. During the first year, from November 2019 to November 2020, the bibliographic research and state-of-the-art analysis of the topics related to the present investigation were carried out at a distance from Saltillo, Coahuila, Mexico. The experimental work was then developed during the following two years and performed at the Department of Engineering (DE) of the University of Ferrara. Most of the activity was carried out within a BiRex/IMA project in collaboration with the Industrial Engineering Department of the University of Bologna (Project AN-MEC - L'Additive Manufacturing nella filiera produttiva dell'industria meccanica: dallo sviluppo del processo alla definizione del business model per la produzione di nuovi componenti", CUP C41J20000030008). Due to the COVID-19 pandemic emergency a 3-month extension under the law of May 2021, no. 69 was requested and authorized.

Prof. Gian Luca Garagnani and Prof. Mattia Merlin from the Department of Engineering of the University of Ferrara were the principal supervisor and co-supervisors, respectively.

The present research investigation is based on the metallurgical and mechanical characterizations of 17-4 PH stainless steel and WC-12Co cermet processed by the Laser Direct Energy Deposition (L-DED) technique and widely employed across the industrial sector. The specimens were produced varying the principal process parameters, such as the laser power, the scanning speed, the powder feed rate (PFR), and the scanning strategies. The main goal was to find out the feasibility of applying this manufacturing process in future industrial applications. The leitmotiv of the research is the correlation between the microstructural characterization, performed by means of optical microscopy (OM), scanning electron microscopy endowed with energy dispersive spectroscopy microprobe (SEM-EDS), X-ray diffraction (XRD), and the performance of the deposited materials also considering the effect of post-fabrication heat treatments. The geometrical features of the deposited layers as well as the microstructure and the hardness of the materials were considered as quality parameters to assess the general performance of depositions.

As a matter of organization, the present work is divided into the following chapters:

Chapter 1 is a literature survey that covers a brief theoretical background of the principal topics of this thesis, as well as the most influential state-of-the-art research studies related to the present work. This chapter introduces the principles of the L-DED process, considering the relationship among the process parameters, the main microstructural and mechanical features, the presence of defects as well as the effects of post-fabrication heat treatments.

Chapter 2 is devoted to the 17-4 PH investigation and the first part covers the material and methods section with the description of the fabricated samples. All the performed analyses and results are then carefully described as concerns geometrical aspects of the deposited single-track layers, the microstructural and the hardness behavior of the tracks according to the different process parameters, and the specifically designed post-fabrication heat treatments. At the end of the chapter, the microstructural and hardness investigations carried out on multi-layer 17-4 PH depositions are also presented and discussed.

Chapter 3 discloses the macro and microstructural analysis, as well as the hardness evolution, of WC-12Co depositions performed with different process parameters on two kinds of substrate. Additionally, a deep investigation of the effect of the scanning strategy across the microstructural and hardness behavior of the deposited material is stated in samples fabricated with the best process conditions and substrate selection.

During the Ph.D. three-year period, the activity related to the doctoral thesis resulted also in the supervision of the following master theses:

Martino Brigo. Master's degree in Mechanical Engineering with the thesis entitled: "Applicazione della tecnologia AM-DED per la deposizione di singole tracce in acciaio 17-4 PH su di un acciaio AISI 316L: analisi microstrutturale e trattamento termico". University of Ferrara, July 2021.

Fuad Debdoubi. Master's degree in Mechanical Engineering with the thesis entitled: "Studio dei parametri di trattamento termico dell'acciaio 17-4 PH processato con tecnologia AM-DED: influenza su microstruttura e durezza", University of Ferrara, June 2022.

Currently, I am the co-supervisor of the bachelor thesis of the following students:

Leonardo Zambello. Bachelor student in Mechanical Engineering, currently developing a thesis based on the study of the heat treatment effect on the microstructural and mechanical features of WC-12Co samples fabricated by DED.

Luca Zatelli. Master student in Mechanical Engineering, currently developing a thesis based on the study of the heat treatment effects on the microstructural and the wear behavior of 17-4 PH multi-layer depositions performed by DED.

Part of the experimental results obtained during the Ph.D. period was presented at the following national and international conferences:

- Conference abstract presented at the Junior EUROMAT 2022 with the work: C. MORALES; M. Merlin, P. Ferrucci, A. Fortini, G.L. Garagnani, A. Fortunato, "WC-Co additive manufactured depositions on an HSS 390 steel substrate: a microstructural investigation", 19 Jul 2022 – 22 Jul 2022. Coimbra, Lisboa.

- Conference poster presented at the Junior EUROMAT 2022 with the work: C. MORALES; M. Merlin, P. Ferrucci, A. Fortini, G.L. Garagnani, A. Fortunato, "17-4 PH SS single-track DED depositions over AISI316L: macro and microstructural investigations", 19 Jul 2022 – 22 Jul 2022. Coimbra, Lisboa.

- Conference paper presented at the 39° Convegno Nazionale AIM (Associazione Italiana di Metallurgia) with the work: C. MORALES; M. Merlin, A. Fortini, G.L. Garagnani, P. Ferrucci, A. Fortunato, "Microstructural analysis of a WC-12Co coating deposited by DED with different scanning strategies", 21 Sep 2022 – 23 Sep 2022. Padova, Italy.

- Conference paper presented at the 39° Convegno Nazionale AIM (Associazione Italiana di Metallurgia) with the work: C. MORALES; M. Merlin, F. Debdoubi, A. Fortini, P. Ferrucci, "The effects of heat treatment on microstructure evolution

of 17-4 PH single tracks deposited by AM-DED", 21 Sep 2022 – 23 Sep 2022. Padova, Italy.

Currently, preliminary results regarding the effect of the heat treatment parameters of the 17-4 PH stainless steel DED depositions have been accepted for publication in:

- C. MORALES, M. Merlin, F. Debdoubi, A. Fortini, P. Ferrucci, "The effects of heat treatment on microstructure evolution of 17-4 PH single tracks deposited by AM-DED", La Metallurgia Italiana, Vol. 114, Issue 2, 2023, p. 42-47.

- C. MORALES, M. Merlin, A. Fortini, A. Fortunato, "Direct Energy Depositions of a 17-4 PH stainless steel: geometrical and microstructural characterizations", submitted to *Coatings*, Special Issue entitled "Surface Treatments for Stainless Steels", Coatings 2023,13, 636. https:// doi.org/10.3390/coatings13030636

Moreover, it is worth noting that, during the Ph.D. period and besides the main research topics on additive manufacturing, some side projects were performed in collaboration with factories. A brief description of each of them is described in the following:

a. Study of the effects of different heat treatment parameters on the microstructural and mechanical properties of wrought aluminum alloy components.

During this experimental project, wrought aluminum alloy components, subjected to different superficial and bulk heat treatment procedures, were analyzed. Microstructure and mechanical behavior were evaluated according to specific conditions of anodizing, painting, heat treatment, and TIG welding. From the study, the optimal process parameters, maximizing the hardness of the alloys, were proposed.

This activity resulted also in the supervision of the following master thesis:

Vittorio Ghelli. Master's degree in Mechanical Engineering with a thesis entitled: "Effetto delle temperature e dei tempi di invecchiamento artificiale sulla durezza di leghe Al-Mg-Si da deformazione plastica", December 2021.

b. Experimental studies on the metallurgical quality of different carbon steels.

Carbon steels of different compositions were studied evaluating the austenitic apparent grain size by different heat treatment methods, as well as the role of the inclusions' content. This activity resulted also in the supervision of the following bachelor thesis:

Enrico Tumiatti. Bachelor's degree in Mechanical Engineering with the thesis entitled: "Analisi di procedure per l'evidenziazione del grano austenitico di un acciaio C10 e influenza sul calcolo del parametro G - Grain size", June 2022.

c. Metallographic investigations of steel automotive components fabricated via powder metallurgy.

During this project, the microstructure of different automotive sintered components was analyzed, and the micro and macro hardness evolution was evaluated as well.

Porosity and apparent density were also measured. This activity resulted also in the supervision of the following bachelor thesis:

Vezzani, Ottavia. Bachelor's degree in Mechanical Engineering with the thesis entitled: "Failure analysis e caratterizzazione microstrutturale comparativa di componenti in acciaio sinterizzato per applicazioni automotive", September 2022.

d. Study of the microstructural and mechanical properties of metallic components produced via SLM additive manufacturing technology.

During this project, the effect of the different process parameters used to print SLM metallic parts was correlated with their microstructural and mechanical behavior. This activity resulted also in the supervision of the following bachelor thesis:

Riccardo Osti. Master's degree in Mechanical Engineering with the thesis entitled: "Studio dei parametri ottimali del processo Selective Laser Melting per gli acciai inox AISI 316L e AISI 430: caratterizzazione meccanica e metallografica", September 2022.

During the doctoral period, another important side project was carried out in collaboration with COMIMSA (Corporacion Mexicana de Investigacion en Materiales), a big research center in Saltillo (Mexico). The study dealt with the EN AW-2024 Friction Stir Welding T-joints produced with different clamping systems and specific optimal process parameters obtained from a radial basis neural network optimization. Moreover, some experimental FSW joints of wrought aluminum alloys have been performed considering the effects of the process parameters, such as both the rotational and the translational speeds, the applied axial force as well as the tool geometry. The effect of the addition of Al_2O_3-SiC powders has also been studied. Microstructural investigations to assess the quality of the obtained joints have been carried out using optical microscopy (OM) and scanning electron microscopy (SEM/EDS). Different mechanical tests (hardness and tensile tests) have been also performed.

This activity resulted also in the supervision of the master thesis of a student of the Department of Engineering of the University of Ferrara, who spent a three-month period in COMIMSA from 15/09/2019 to 15/12/2019:

Stefano Giudici. Master's degree in mechanical engineering with the thesis entitled: "Friction Stir Welding of dissimilar AA2024/AA7075 aluminum alloys: effect of Al_2O_3-SiC powders addition on microstructural and mechanical properties", March 2020.

Results regarding this topic were presented at the following national and international conferences:

- Conference paper presented at the 38° Convegno Nazionale AIM (Associazione Italiana di Metallurgia) with the work entitled: "On the microstructural properties of similar EN AW-2024 T- joints produced by FSW with different clamping setting systems". Telematic edition, 18 Jan 2021 – 19 Jan 2021.

- Conference paper presented at the 38° Convegno Nazionale AIM (Associazione Italiana di Metallurgia) with the work: A. Miranda, C. MORALES, A. Fortini, G.L. Garagnani, S. Giudici, M. Merlin, "Effect of Al_2O_3-SiC powder addition on

the microstructural and mechanical properties of dissimilar AA2024-AA7075 FSW joints". Telematic edition, 25 Jan 2021 – 26 Jan 2021.

- Conference paper presented at the Junior EUROMAT 2021 with the work: A. Miranda, C. MORALES, M. Merlin, A. Fortini, G.L. Garagnani, "Impact behavior of dissimilar AA2024-T351/7075-T651 FSWed butt-joints: effects of Al_2O_3-SiC particles addition". 13 Sep 2021 – 14 Sep 2021

Results regarding this topic led also to the publication of the following journal article:

- C. MORALES, M. Merlin, A. Fortini, G.L. Garagnani, A. Miranda, "Impact behavior of dissimilar AA2024-T351/7075-T651 FSWed butt joints: effects of Al_2O_3-SiC particle addition", Frattura ed Integrità Strutturale, 60, (2022), 504-515. https://doi.org/10.3221/IGF-ESIS.60.34.

TABLE OF CONTENTS

LIST OF FIGURES

LIST OF TABLES

LIST OF EQUATIONS

NOMENCLATURE AND SYMBOLS

AM	Additive Manufacturing
DED	Direct Energy Deposition
PBF	Powder Bed Fusion
BJ	Binder Jetting
WC	Tungsten Carbide
Co	Cobalt
AB	As built
PFR	Powder feed rate
VED	Volumetric Energy Density
LED	Laser Energy Density
OM	Optical Microscope
SEM	Scanning Electron Microscope
EDS	Energy Dispersive Spectroscopy
XRD	X-Ray Diffraction
AISI	American Iron and Steel Institute
AIM	Associazione Italiana di Metallurgia
TIG	Tungsten Inert Gas welding
SLM	Selective Laser Melting
COMIMSA	Corporacion Mexicana de Investigacion en Materiales
FSW	Friction Stir Welding
Al_2O_3-SiC	Alumina with Silicon Carbide reinforcement
T-joints	Joints in T welding geometry
3D	Three dimensions
ASTM	American Society for Testing and Materials
L-DED	Laser based Direct Energy Deposition
CAD	Computer-Aided Design
ISO	International Standards Organization
ME	Material Extrusion
MJ	Material Jetting
VP	Vat Photopolymerization
HAZ	Heat Affected Zone
PH	Hardened precipitated
F	Ferrite solidification mode
FA	Ferrite-austenite solidification mode
A	Austenite solidification mode
AF	Austenite-ferrite solidification mode
δ	Delta ferrite
SLS	Selective Laser Sintering
E-PBF	Electron based Powder Bed Fusion
BJAM	Binder Jetting Additive Manufacturing
EB3D	Electron beam 3D printing
η	Eta phase
α	Martensitic phase
γ	Austenitic phase
LoF	Lack of Fusion

INTRODUCTION

Over the last 10-15 years, Additive Manufacturing (AM) of metals, also known as metal 3D printing, has continuously increased attention and gained a pivotal role in the manufacturing panorama as opposed to conventional subtractive manufacturing methodologies. According to ASTM, AM processes are classified into seven main categories, that are based on digital 3D design data used for layer-by-layer part creation.

Among the seven classifications, Binder Jetting (BJ), Powder Bed Fusion (PBF), and Direct Energy Deposition (DED) technologies are known to be widely employed due to their high capacity to produce fully dense metallic industrial parts. Nevertheless, their different metal delivery and heating mechanism directly influence the part complexity, flexibility, and features of the final part.

Direct Energy Deposition (DED) is one of the most promising AM techniques employed for printing metallic parts because it is not only used for fabricating near-net-shape parts but also as a repairing and re-manufacturing procedure of high-volume components.

In the DED process, a high-density heat source is controlled by an automated digital path plan to melt the deposited material into a required layer geometry. Recently, it gained attention due to its high ability to produce excellent results along with the wide variety of materials that can be processed, such as high speed-steels, tool steels, titanium-based alloys, cobalt-based alloys, shape memory alloys, cermets, and high resistance stainless steels, which are known to be difficult to be printed.

The research of high-resistant AM parts produced with materials such as 17-4 PH and WC-Co is a matter of high interest in the industrial field since their special properties including high mechanical and wear resistance, toughness, and corrosion resistance promote excellent results for mechanical applications. Although DED technology is rapidly growing worldwide, many challenges are remaining in the processing of such alloys in order to obtain good-quality DED parts.

In light of this, in the present research investigation, both 17-4 PH stainless steel and WC-12Co cermet were considered to be deposited via the L-DED technique and according to different process parameters. Specifically designed specimens were fabricated to evaluate their main microstructural features and understand how the microstructure may influence the hardness of the materials. Single tracks of 17-4 PH stainless steels were firstly deposited by DED onto an AISI 316L substrate using different process parameters The most promising process parameters were then selected to perform a deep investigation. Different heat treatment routes were considered as post-fabrication treatments and multi-layer depositions were also fabricated and analyzed. Concerning the WC-12Co depositions, a similar investigation was carried out, also considering the effect of the substrate material across the microstructure and the hardness evolution at different process conditions. Further analyses with different scanning strategies and different numbers of deposited layers were also performed.

CHAPTER 1 THEORETICAL BACKGROUND AND STATE-OF-THE-ART

The present chapter outlines the theoretical background related to the principal topics of the present doctoral thesis including a brief description of the DED additive manufacturing process, its main process parameters, potential defect formation, and commonly employed post-fabrication procedures. A metallurgical description of both 17-4 PH stainless steel and WC-12CO cermet, with emphasis on their solidification features according to the DED process parameters, is discussed. Moreover, at the end of the present chapter, a review of the most recent state-of-the-art publications focusing on the employment of DED for the deposition of different kinds of materials, as well as their microstructural and mechanical performance, also considering post-fabrication heat treatment procedures, is highlighted.

1.1 THE DIRECT ENERGY DEPOSITION PROCESS

According to ASTM [1]– [3], additive manufacturing (AM) is a thermal procedure that built layer-by-layer a tridimensional part from a 3D model data, as opposed to the traditional subtractive produced parts. Although this group of techniques can be classified by how the material is heated and deposited, the ASTM/ISO 52900 [4] identifies seven different classes including Powder Bed Fusion (PBF), Sheet Lamination (SL), Materials Extrusion (ME), Material Jetting (MJ), Binder Jetting (BJ), Direct Energy Deposition (DED) and Vat Photopolymerization (VP). These techniques are employed to print a wide variety of materials for applications that cover several sectors, such as automotive [5]–[7], tooling [6], [8] but also food&beverage and medical [9]–[12].

In this context, it is well known that PFB is one of the most commonly used processes to deposit full-density metal parts with suitable features that are nowadays required by industrial cases [13]–[15]. However, another great candidate to deposit high-quality parts is the Laser Direct Energy Deposition (L-DED) technique. As mentioned by Schindelholz and Herzog [16], [17] these two procedures will be dominant in the next future to obtain high-quality 3D metallic parts, acting as complementary techniques and not as competitors.

Large-scale complex geometry parts are usually fabricated or just repaired with the use of L-DED [18], [19], however, post-fabrication procedures such as machining or thermal treatments are commonly applied in order to achieve the requirements for engineered components.

1.1.1 Overview of Direct Energy Deposition

The DED procedure is mainly classified by the type of the feedstock material, which could be a wire [20], [21] or a powder [22], [23], as well as by the type of the heat source, which could be a laser, an electron beam, or a plasma [24].

L-DED process consists of a machine with a nozzle mounted on a multi-axis arm that deposits the raw material, in the form of powder or wire, onto the substrate while it is melted by the effect of the laser acting as energy heat source [25]–[27].

In Figure 1. 1 the main classification of the DED process is schematized [24]–[26].

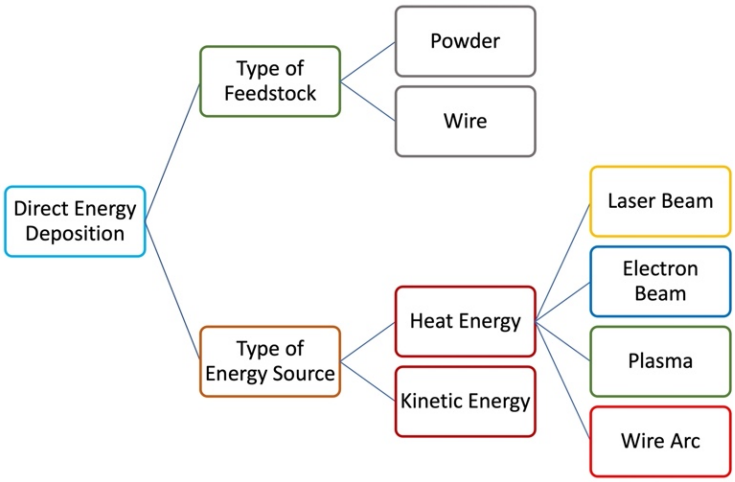

Figure 1. 1 Main classification of direct energy deposition technique. Image inspired by [25].

A DED system usually requires:

- A heat source to melt the feedstock material.

The source could be an electron beam, a laser beam, or a plasma, being the laser beam the most employed in ranges from 500 W to 10 kW.

- A deposited head, that controls the energy source and the direction of the feedstock material.

This one is used to focus the beam on the substrate as the powder is directed for deposition. A shield gas is commonly employed in order to minimize the contamination of the optics, and to protect the molten area.

- A feeding feedstock continuous system.

This is the camera that controls the feeding of the metal guiding it to the nozzle, which can be uniaxial or in a coaxial arrangement. This part also supplies the shield gas.

- Motion system.

When a robot is used as the moving head of the deposition system, a great variety of axes should be controlled to fulfill the accuracy of the deposition.

- Computer controller system.

In most instances, this system controls the path of the heat source as well as the variation of the process parameters.

In the fabrication of a single track, the focused energy melts both the feedstock metal and the substrate, thermally affecting the surrounding metal part and generating the so-called melt pool zone, a thermodynamically unstable region of the superheated molten metal with a typical spherical droplet shape. Once the heat source moves forward, the melt zone solidifies because of heat dissipation and thus forming the first layer.

Figure 1.2 show a simple scheme of the DED process, while in Figure 1.3 a usual image of a DED machine characterized by a uniaxial nozzle feeder is depicted.

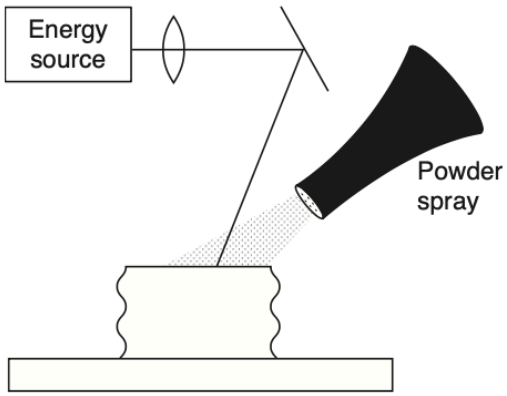

Figure 1.2 Scheme of direct energy deposition process [28].

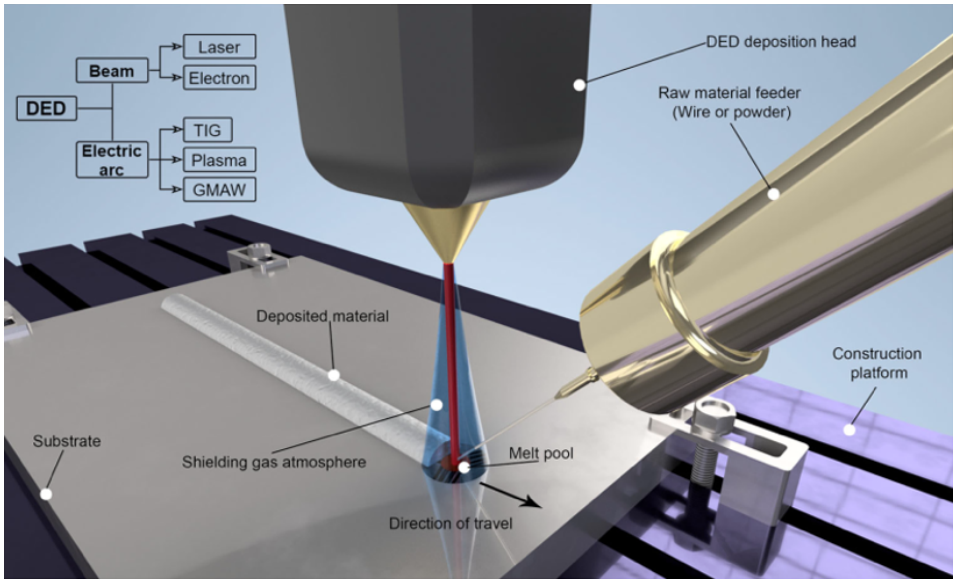

Figure 1.3 Direct energy deposition process diagram [24].

1.1.2 L-DED process parameters

To fabricate a high-quality part through L-DED technology is necessary to analyze the thermal response of the material during the processing since a wide range of variables are strictly correlated with the solidification rates and so with the microstructure of the deposited material. The most common process parameters employed in L-DED are the ones defined in Figure 1.4 including power P provided by the heat source, the velocity V of the heat source, the diameter *dspot* of the energy source, the powder feed rate *PFR* of the provided feedstock material and the space S among the depositions beads (hatch spacing).

In the literature, the suitable window for optimizing the DED process is described by the laser energy density, E (J/mm^2). This factor is a combination of the most important abovementioned process parameters and describes the laser effectiveness during the deposition. It is defined as Equation 1.1, where P is laser power (W), V is scan speed (mm/s) and s is laser spot size (mm) [29]–[31]. Additionally, when multilayer overlapped depositions are produced another important factor inherent to the energy density can be employed to analyze the effect of the total energy per unit volume (VED), Equation 1.2 [32]–[35]. P is the laser power (W), V is the scanning speed (mm/s), t is the layer thickness (mm) and h is the hatch spacing (mm).

Equation 1.1

$$E = \frac{P}{V \cdot s} [J/mm^2]$$

Equation 1.2

$$VED = \frac{P}{V \cdot t \cdot h} [J/mm^3]$$

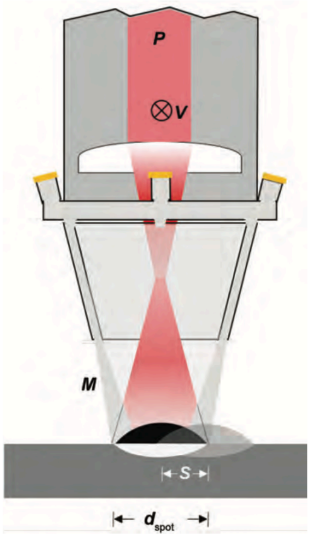

Figure 1.4 Laser-based DED process parameters illustration [28].

The primary process parameters mentioned before are usually employed to establish the principal geometrical features once the first layer is deposited over the substrate as observed in Figure 1.5. Typically, in L-DED the power of the laser and the spot size maximize the deposition width since they determine the amount of the contact area of the laser between the substrate and melted powder. While together the power, powder feed rate, and scan speed determine the height of the bead since regulate the speed of the deposited material. Instead, both laser spot size and power laser have a strong effect on the required melted substrate, also expressed as laser energy density. Meanwhile, the hatch spacing is key to determining the optimal distance between two adjacent deposited tracks.

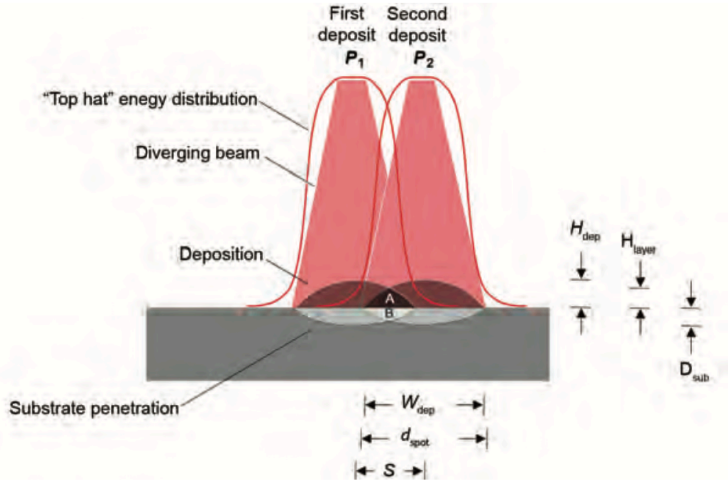

Figure 1.5 Scheme of the process parameters across two laser direct energy depositions [28].

One of the most important aspects of L-DED is the understanding of the effects of different combinations of process parameters on the geometrical characteristics of the single-track clads in order to establish the process parameters to be used in future multi-track

depositions. As can be observed in Figure 1.6, in some studies [36]–[39] the cross-sectional analysis of the deposited tracks is performed to quantitatively measure the geometrical features of single deposited tracks.

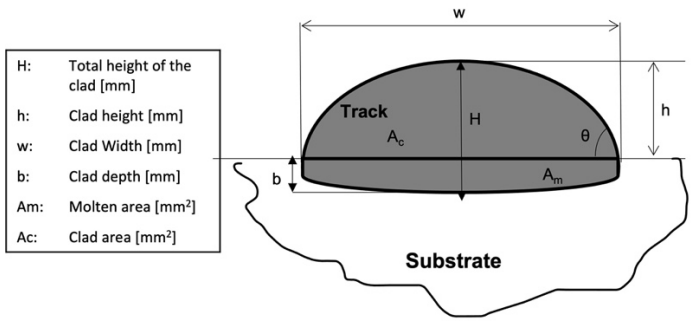

Figure 1.6 Geometrical feature analysis of a laser-clad deposition [38].

As shown in the figure, features such as height, width, and area of the cross-section of the clad, as well as the depth of its penetration in the substrate, are usually measured to calculate the dilution factor. The dilution D [%] is a crucial parameter useful to evaluate the adhesion, bonding, and integrity of the clad deposited onto a substrate material and it is defined by the ratio of the melted substrate area to the total melted zone, as described by Equation 1.3 [39].

Equation 1.3 [39]

$$D\,\% = \frac{A_m}{A_c + A_m} \cdot 100$$

In the study performed by Dass et al [40], it is mentioned that there is a range of acceptance of the dilution parameter to qualify the DED dispositions, which is among 10-30 %. This value is lately corroborated by D. Ahn et al [26], and Bax et al [37]. Eun Mi Lee et al [41] considered the importance of the control of the basic process parameters to determine the best condition for good quality single-track fabrication; in this study, the authors studied the effect of the process parameters on the geometrical features of deposited AISI M4 DED parts (see Figure 1.7). After the performed analysis and its correlation with the main process parameters, i.e. laser power [W], powder feed rate [g/min], and scanning speed [mm/min], it was found that the bead geometry of the clads is positively influenced by an increase in the laser energy density (see Figure 1.8) as well as by the powder deposition efficiency. This kind of analysis was also relevant to be considered for performing potential multi-track depositions but also to reduce the number of defects. The dilution parameter was detected as one of the most important factors to determine the bonding strength among the substrate and the deposited track, as well as to optimize the mechanical and metallurgical properties.

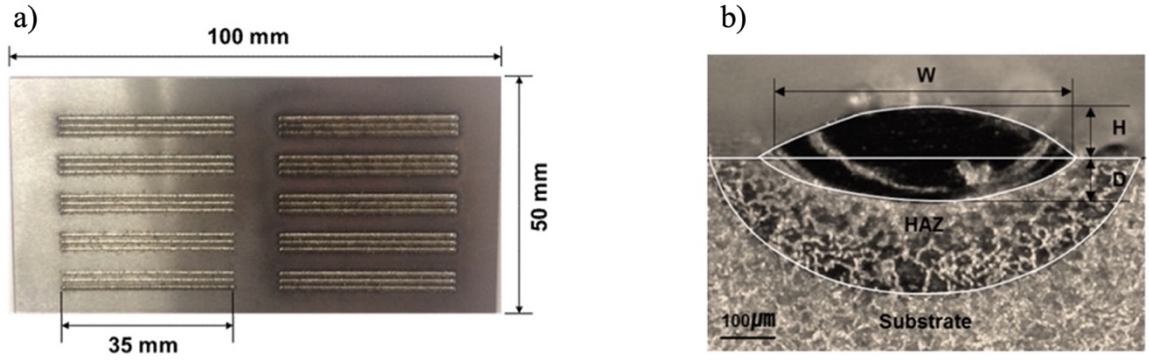

Figure 1.7 a): Deposited single tracks, b): cross-sectional deposited single tracks geometrical analysis [41].

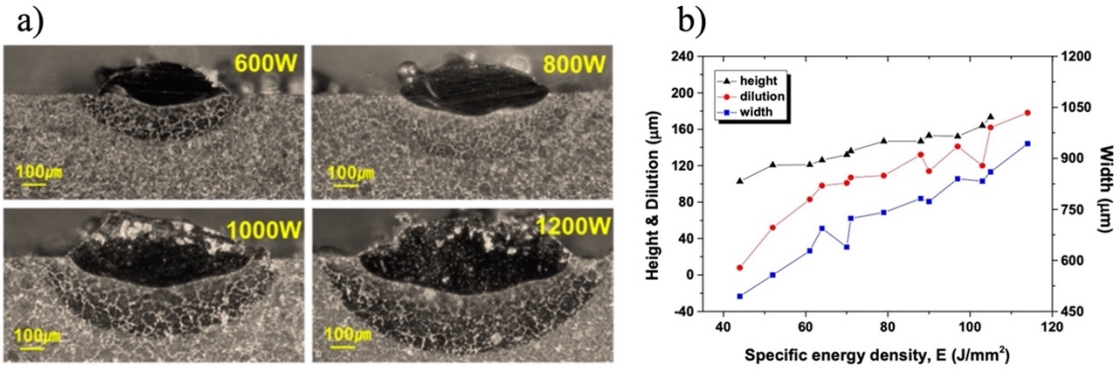

Figure 1.8 a): Geometrical analysis with the laser power effect, b) energy density measurement across the different laser powder variation samples [41].

Another important parameter, which can be strictly correlated to the soundness of the deposition, is the scanning strategy which describes the path that the heat source is following during the deposition of the metal. In the literature, different types of scanning patterns are suggested to be used to reach different and specific results, such as a decrease of the number of defects, thus improving the microstructural features. In Figure 1.9 are collected most of the common scanning strategies. M. O. Gushchina *et al.* [42] investigated the effect of shown scanning strategies on the mechanical properties of a titanium alloy deposited by L-DED. After a deep microstructural and mechanical testing, the authors have found that this parameter is highly important to improve the mechanical behavior of deposition since when the scan strategy changes the thermal history affect directly the hard and brittle structure formation, which consequently initiates the crack propagation. As a result, it was found that when the scanning strategy is continuous in terms of hatching spaces and type of deposition as Type A, the as-built specimens are prompt to develop better mechanical properties and decomposition of the martensite. However, when a heat treatment is applied the scanning strategy releases its stresses producing no specific results.

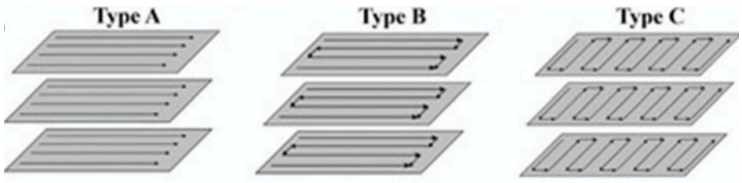

Figure 1.9 Most common DED deposition scanning patterns used in [42]. Type A: raster, type B: bidirectional or zig-zag, type C: variation in the size of the bidirectional scans pattern width [42].

It is worth noting that in the L-DED process, a wide number of variables (see Figure 1.10) should be taken into account and monitored as influencing the microstructure and the material properties [43], [44]. [43], [44]. Nevertheless, many of them are usually considered as a constant because are strictly defined by the specific equipment and or by the powder production.

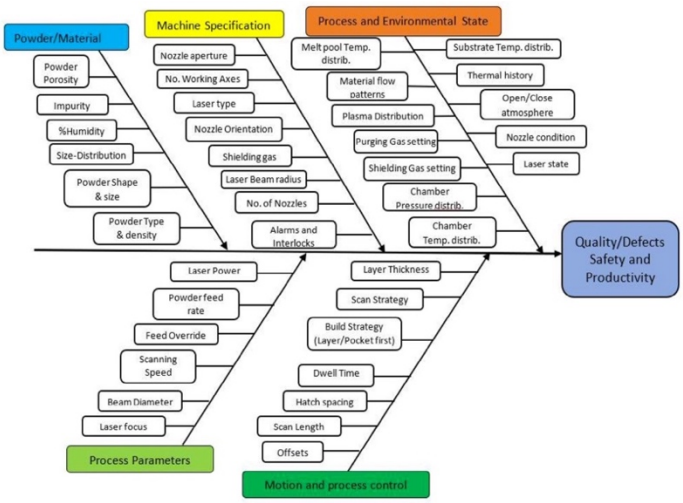

Figure 1.10 Fishbone diagram of the process parameters to be controlled during the DED process [43].

1.1.3 Solidification and microstructure evolution

As already mentioned, during the L-DED process, a laser heat source is used to melt and ri-solidify the feedstock metal, usually supplied as a powder and following specific scanning paths in a layer-by-layer deposition. Heating, melting, vaporization, and solidification are just some of the mechanisms that occur during this process. The response of the metals to the heat source effect starts with a solidification followed by solid-state transformations which occur during subsequent heating and cooling cycles associated with the layer-by-layers fabrication. Both melting and solidification processes that occur during the interaction between the feed of the powder and the heat source are governed by the heat transfer which promotes the particles to travel toward the substrate's surface, forming the molten pool and below it the heat-affected zone (HAZ), Figure 1.11 shows a scheme of the complex inner mechanisms that are involved during the depositions [24], [25], [45].

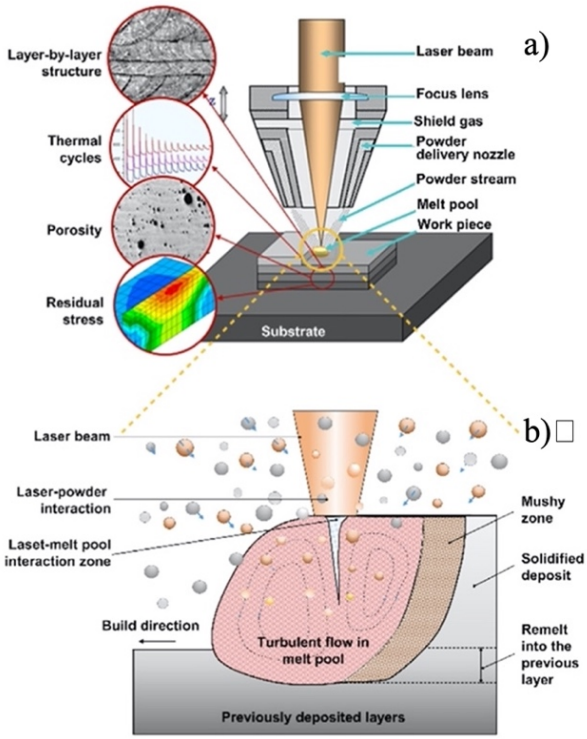

Figure 1.11 Upper; DED process description with lower; a microstructural demonstration of the inner part of a DED deposition [27].

The main microstructural features of the solidified metal can be explained as a direct consequence of both the cooling rate (R) [mm/s] and the thermal gradient (G) [°C/mm]. In fact, the G/R ratio determines the solidification mode and the product GxR governs the size of the solidification structure [46]. Their values promote the different structure morphologies within DED parts: columnar (elongated grains), columnar-plus-equiaxed, or equiaxed (isotropic grains) [47], [48] as observed in Figure 1.12.

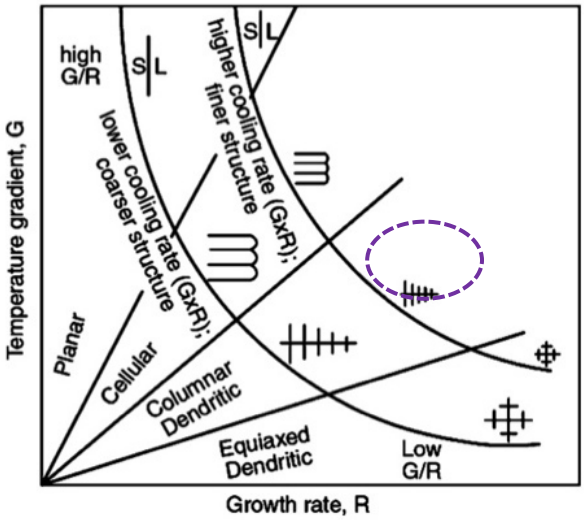

Figure 1.12 Effect of the G/R ratios over the solidified microstructure. Purple dotted lines show the morphology of the L-DED sample microstructure [46].

A typical cooling rate of the L-DED depositions ranges from 10^3 to 10^5 °C/s, promoting a very complex microstructure morphology but in general finer across the printed part. However, in accordance with [46] four mechanisms can occur during laser additive manufacturing processes: 1. dendrite fragmentation, 2) grain detachment, 3) heterogeneous nucleation, and 4) surface nucleation.

1. Dendrite fragmentation:

Within the melt pool of the deposited part different processes occur, causing fragmentation of the tips of the dendrites as observed in Figure 1.13 This fragmentation acts as nuclei for the new grains.

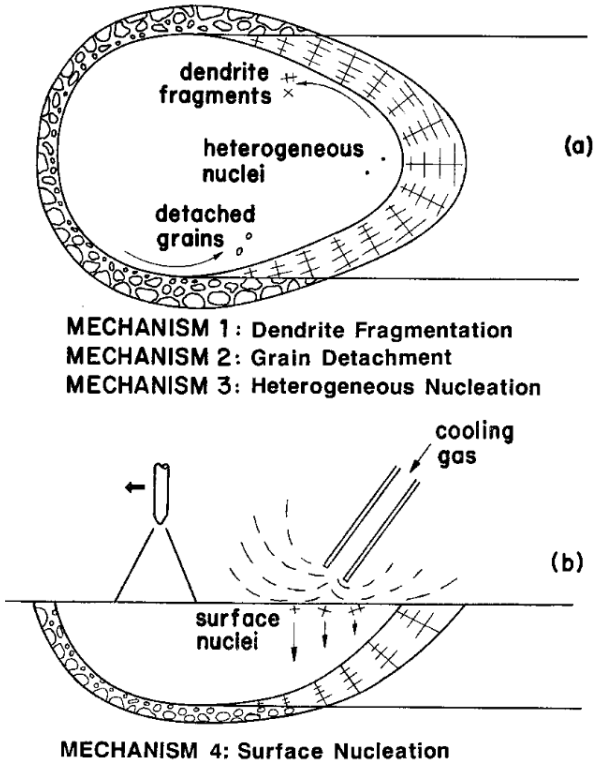

Figure 1.13 Nucleation mechanism during a laser deposition procedure.

2. Grain detachment

Across the molten pool, the convection mechanisms can partially melt the grains to detach them from the solid-liquid mixture within the molten pool, as shown in Figure 1.13 a. As in the last mechanism, if these grains support high temperatures, they can act as nuclei for the formation of new grains.

3. Heterogeneous nucleation

However, if foreign particles are present in the melt pool, the liquid metal can be arranged in a crystalline form acting as heterogeneous nuclei. Figure 1.14 depicts heterogeneous nucleation and the growth of new grains.

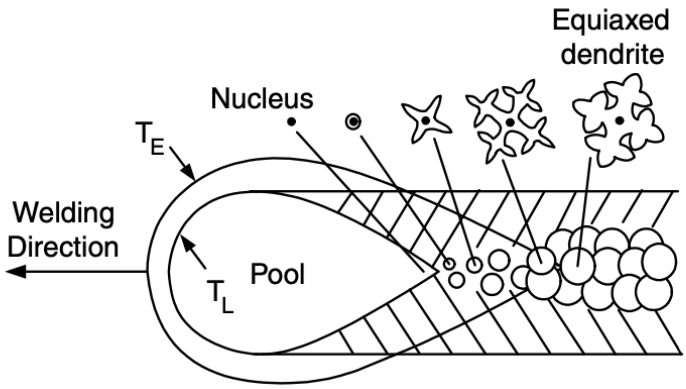

Figure 1.14 Heterogeneous nucleation and formation of equiaxed grains in the processed metal.

4. Surface nucleation

The surface of the molten pool can be undercooled to induce surface nucleation by direct exposure to gas protection or the movement of the heat input source. When this occurs,

solid nuclei can form at the molten pool surface as illustrated in Figure 1.13 b. These solid nuclei then grow and go down to the molten pool due to their high density.

1.1.4 Process defects

The fast-cooling rates and high thermal gradients that occur during L-DED generate a non-equilibrium solidification process. Moreover, the complex laser-matter interaction can lead to a dynamic evolution of the material within the melt pool which is dramatically complex. These non-desirable and non-uniform solidification conditions lead to the degradation of the mechanical behavior and often to the premature failure of the fabricated parts. These negative outcomes can be mitigated with the adjustment of the process building conditions.

There are plenty of works [25]–[27], [43] describing the most important defects that could be induced in the material during the processing of L-DED parts, and the following Table 1.1 are summarized the most common morphological defects that could appear inside the deposited tracks, also with a mention to their main origin.

Table 1.1 Summary of the most frequent defects generated during L-DED and their origin [25]–[27], [43].

Defect	Origin	Defect	Origin
Residual stresses	High cooling rate and thermal gradient	Edge defect	High laser power and laser speed, scanning speed wrongly selected, high thermal gradients
Distortions			
Porosity	High laser energy density, due to gas trapping into the solidifying melt, due to feedstock porosity or from lack of fusion.	Material shrinkage	Slanted edges of the previous layer that cause shrink via dragging
Delamination	Inadequate laser power, residual stresses either high or too low energy input.	Lack of powder fusion	Excessive powder flow rate or lack of energy input may lead to insufficient melting.
High roughness	Variation in powder features, high scanning strategies and/or un-melted fused powder.	Wrapping on top surface	Ineffective laser power and scan speed
Cavities	Gas entrapment during solidification, lack of powder fusion or excessive amount of powder.	Cracking	Solidification of continuous films along grain boundaries or solid shrinkage stresses.

Formation of porosities is rather usual across L-DED parts, and it is strictly correlated to the mechanical properties of the final part. Its formation is usually due to different aspects which are:

- Lack of fusion porosity

This kind of porosity is usually produced due to the lack of a proper energy density that produces the lack of fusion of the powder material. These porosities are distinguishable because of their irregular and elongated shape.

- Gas porosity

This porosity is usually produced due to the gas entrapment into the melt pool that happens during the process and is generally correlated to the lack of a shielded environment, to the humidity of powder or to the porosity itself that may be present in the powder. In this case, the pore is usually very spherical.

- Keyhole porosity

This type of porosity is the opposite of the lack of fusion since it is produced due to the excess of energy density that promotes material evaporation. The shape of the pores is usually similar to the one of gas porosity since they are spherical but with an irregular contour.

Porosity [Ap%] is one of the geometrical features that is commonly measured in order to estimate the porosity content into the clads, as defined by Equation 1.4 [39] in which *Ap* is the area of the pores, *Ac* is the area of the clad and *Am* is the area of the dilution zone [37], [38].

Equation 1.4 [39]

$$Ap\ \% = \frac{A_p}{A_c + A_m} \cdot 100$$

Different studies, such as the ones of C.Zeng [49] and Erfamansech [50], have focused on the effect of the process parameters on the porosity contents inside of single-track depositions. As a result, it has been observed that this defect is not only a consequence of the selection of the process parameters, but it is significantly influenced by the characteristics of the powder. In the work of Zhong [51] the effect of the porosity content into the depositions, when a drying treatment before the deposition is applied, was investigated. The execution of a drying treatment before the deposition leads to a significant reduction of porosity and so promoting better-quality depositions.

1.1.5 Post-fabrication techniques

The L-DED fabricated parts are usually characterized by high levels of thermally induced stresses together with poor surface finishing and a non-uniform roughness. These inhomogeneities decrease the mechanical properties of L-DED parts, which is considered unacceptable for the industrial sector.

To achieve the required functionality of these parts, usually, post-building processing is desirable to relieve the specimens from stresses, tailor their mechanical properties, homogenize their microstructure, and improve the surface characteristics [17]. Figure 1.15 shows an image of the most employed post-processing methods to modify a specific property of additively manufactured parts, i.e., heat treatments, hot isostatic pressing (HIP), and machining/grinding.

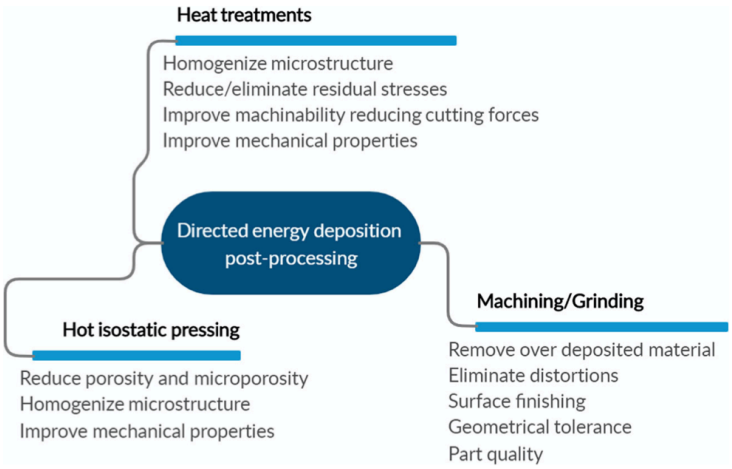

Figure 1.15 Post-processing treatments are usually employed on L-DED printed parts [24].

In accordance with [24] and [28], HIP is the most powerful treatment that can lead to a drastic decrease of porosity. Nevertheless, conventional heat treatments are the commonly employed route to increase the mechanical performance of the parts through microstructure control without the higher costs of the HIP process.

1.2 L-DED DEPOSITIONS OF HIGH-RESISTANCE ALLOYS

The employment of additive manufacturing techniques to produce high-performance parts for the industrial field is a topic of high interest, however, the control of the microstructure and the mechanical properties through a proper selection of process parameters is very challenging. Different studies such as [3], [16], [52] have performed a deep review analysis of the production of parts of materials such as steel, composites, and light alloys through the use of different additive manufacturing processes. The authors pointed out that nowadays the production of metallic parts is widely feasible to obtain via these techniques, nevertheless, the industrial and research field is on continuously searching to optimize their productions and decrease drawbacks with the aim of increasing the quality of the final parts.

In the literature, the number of papers dealing with the investigation of high-resistant alloys processed by L-DED is scarce, so being a great opportunity to explore the feasibility of this AM technology as a complementary process to L-PBF.

1.2.1 Precipitation hardening stainless steels

Precipitation hardening (PH) stainless steels are Fe–Cr-Ni martensitic alloys with precipitation-hardening elements (Ti, Nb, and Cu), widely used in the industrial field due to their high strength and good corrosion resistance. During the hardening process, usually promoted via high-temperature solid solution and subsequent aging heat treatment, the main elements promote their finer precipitation within the martensitic matrix increasing the mechanical behavior of the alloy.

Typical applications of PH stainless steels are aerospace, machinery, medical to chemical, and nuclear industries due to their excellent mechanical properties. However, they are characterized by poor machinability by conventional manufacturing processes due to their high hardness and strength. So, the use of AM processes has increased the ability to fabricate PH parts of complex geometry and excellent mechanical behaviors [53], [54].

1.2.1.1 17-4 PH stainless steel

The 17-4 PH stainless steel is a martensitic steel with 17 wt.% of Cr, 4 wt. % of Ni, and 4 wt. % of Cu that can offer an excellent combination of high mechanical resistance at higher temperatures (until 300 °C), good corrosion resistance, and toughness. Due to these interesting properties, it is widely used in the aerospace industry to produce components that require high strength and good corrosion properties at high temperatures.

The 17-4 PH stainless steel is commonly found in the annealed condition, but the age-hardening treatment is usually applied to accomplish the strength of the alloy. The whole cycle of final heat treatment consists of three major steps: solution treatment, rapid quenching, and subsequent artificial aging.

During solubilization, performed at a specific temperature and for a selected holding time, all the coarse Cu-rich precipitates dissolve into a completely homogenized austenitic matrix. During quenching, after the rapid cooling at room temperature, the alloying elements remain in an oversaturated solid solution. Hence, during the aging treatment, a number of nanometric coherent or semi-coherent Cu-rich precipitates from the oversaturated solid solution, increasing with the mechanical properties of the alloy.

For the analysis of the microstructural evolution of this material during solidification and subsequent solid-state transformations is usually necessary to know the ratio Creq/Nieq considering the amount of ferritizating and austenitizing elements in the chemical. composition [55], [56]. The Creq/Nieq ratio is calculated using the following Equation 1.5 and Equation 1.6:

Equation 1.5

$$Cr_{eq} = \%Cr + \%Mo + 1.5\%Si + 0.5\%Nb$$

Equation 1.6

$$Ni_{eq} = \%Ni + 30\%C + 0.5\%Mn + 30\%N$$

Usually, if the calculated ratio is higher than 1.5, as in the case of the 17-4 PH stainless steel, the solidification starts from the liquid with the presence of primary δ-ferrite (F). Conversely, if this value is lower than 1.5 the solidification from the liquid starts with primary austenite (A). Nevertheless, with the higher cooling rates reached during the AM processes it is also important to consider the kinetics of the process. If the cooling rate is high, during the solidification of a regular 17-4 PH stainless steel, the first phase to form is the δ-ferrite which partially transforms into austenite by a peritectic reaction; later, the austenite transforms into martensite by the displacive reaction during the cooling across the range Ms-Mf. Due to the low content of C, the cooling rate governs the quantity of retained austenite and the quantity of martensite.

At room temperature, the 17-4 PH stainless steel is conformed of δ-ferrite and retained austenite in a martensitic matrix. The δ-ferrite phase is responsible for the magnetic properties of these steels [57]–[62]. Figure 1.16 shows the typical microstructure of these types of steels.

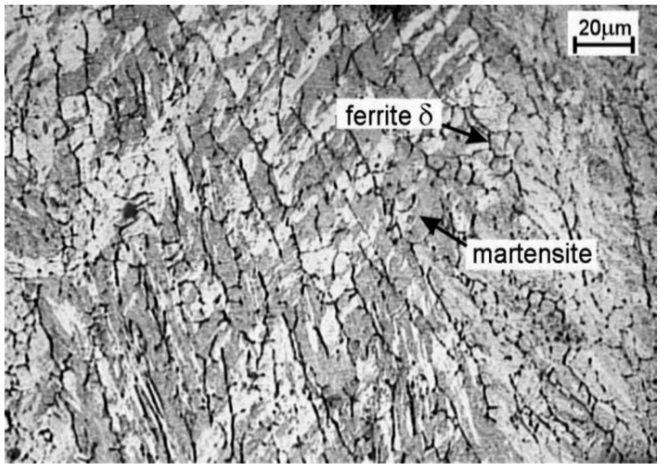

Figure 1.16 Typical microstructure of as-built 17-4 PH specimens. Micrograph of a welded samples obtained from [61].

During the L-DED process, the non-equilibrium cooling rates promote a very fast solidification which consequently produces a certain amount of δ-ferrite in a martensitic matrix. In the literature, authors such as Auguste [63] studied the microstructural evolution of the 17-4 PH stainless steel processed via Selected Laser Melting (SLM), starting with powders of different compositions. The authors stated that it is difficult to assess the microstructural components across the samples with the use of common characterization techniques. With the use of EBSD analysis, and independently of the powder composition, they could determine the typical martensitic structure as well as the presence of δ-ferrite and residual austenite, as observed in Figure 1.17.

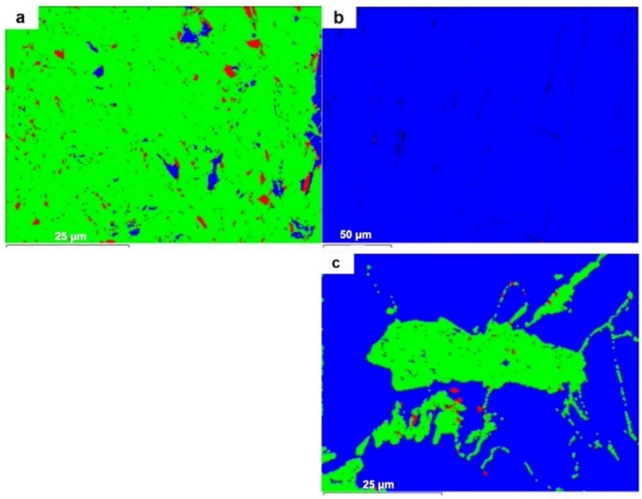

Figure 1.17 EBSD analysis of the SLM different powder compositions samples. The different colors identify the diverse microstructure, green: martensite, blue: ferrite, and red: residual austenite [63].

In the conclusion of the study, the authors affirmed that the first phase formed from the liquid is the δ-ferrite when the Cr/Ni ratio is higher than 2, but it is also mentioned that the presence of the ferritic microstructure across the martensitic matrix is highly conditioned by the cooling rate suffered during the process, avoiding the total transformation of δ-ferrite to austenite during the solid-state transformation.

1.2.1.2 Effect of the process parameters on 17-4 PH L-DED depositions

As mentioned in paragraph 1.1.2 adequate control of the process parameters across the L-DED depositions is the key to manage the heat input during the process and consequently control the microstructural and mechanical properties of a piece. Besides, it reduces defect presence such as cracking, residual stresses, and porosity.

The scanning speed, the power of the laser, and the powder feed rate are the most important parameters that additionally influence the laser energy density factor across the samples. In literature, it has been observed that studies related to the 17-4 PH stainless steel processed by L-DED are scarce, however, the most interesting results are discussed as follows.

Mathoho et al [30] performed a study of the effect of the process parameters on 17-4 PH depositions to analyze the presence of defects, the microstructure, and the mechanical properties with and without post-fabricating heat treatments. One of the most important results of the authors was that 17-4 PH stainless steel is suitable to be processed by L-DED employing specific parameters and obtaining excellent densities (upper than 99.9 %). Additionally, it was stated that the laser power is the parameter that has more effect on the grain morphology and consequently on the hardness behavior, finding that this property decreases when the laser power increases while the scanning speed has a limited relevance (see Figure 1.18).

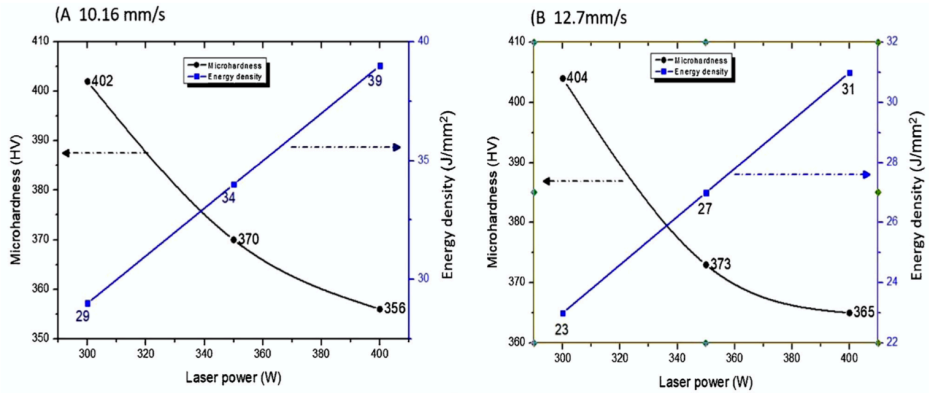

Figure 1.18 Effect of laser power on the microhardness values for two different scanning speed[30].

Adeyemi et al [57] performed a study about the effect of the laser power variation in the range of 1000-2600 W on the microhardness and wear resistance of the deposited parts. As can be noticed in Figure 1.19, the authors found a martensitic microstructure, but with high contents of δ-ferrite. They also observed a change from fine to coarse grains of δ-ferrite according to the increase of the laser power.

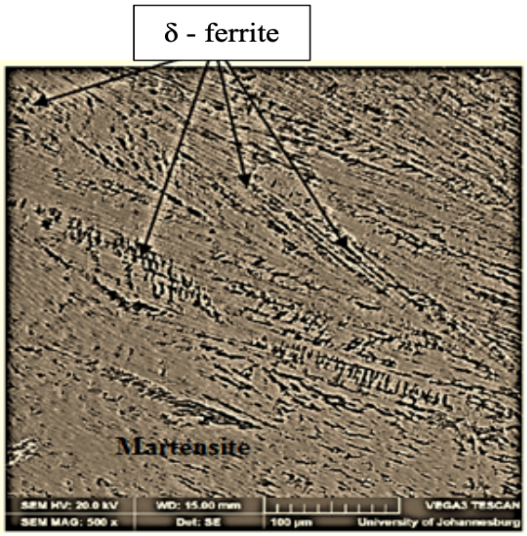

Figure 1.19 Microstructure found on the tested samples [57].

As concerns the hardness behavior, they did not find a linear correlation between hardness and laser power. Hardness is more correlated to the δ-ferrite content and to the reinforcing precipitates than to the laser power. The hardness values decrease at certain laser power values, but they later increase with the laser power (see Figure 1.20); this is due to the size and distribution of the δ-ferrite across the martensitic matrix and to the dynamic of precipitation of the reinforcing particles during the process.

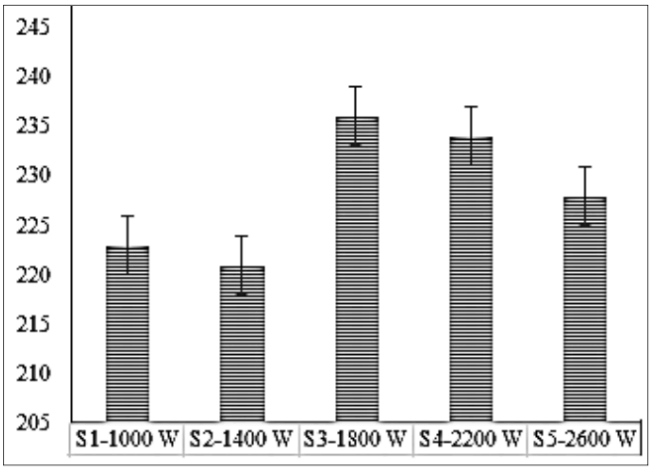

Figure 1.20 Effect of the laser power on the hardness behavior of the samples tested in the study [57]

Gökçe Aydin et al [64] performed an analysis of the effect of the Laser Melting Deposition (LMD) process parameters on both the geometrical features and the dilution of 13-8Mo PH stainless steel depositions. Given that the dilution is crucial for the efficiency of the deposition, the authors used a full factorial of two levels design of experiments to accurately select the process parameters to be employed.

After the first geometrical analysis performed on the depositions, the authors found that, according to the statistical regression coefficients for each parameter, the laser power has the strongest influence on the geometrical features of the bead, such as the height, the width, and the depth of the initial depositions. Figure 1.21 shows the experimental results, while Figure 1.22 collects the statistical ones.

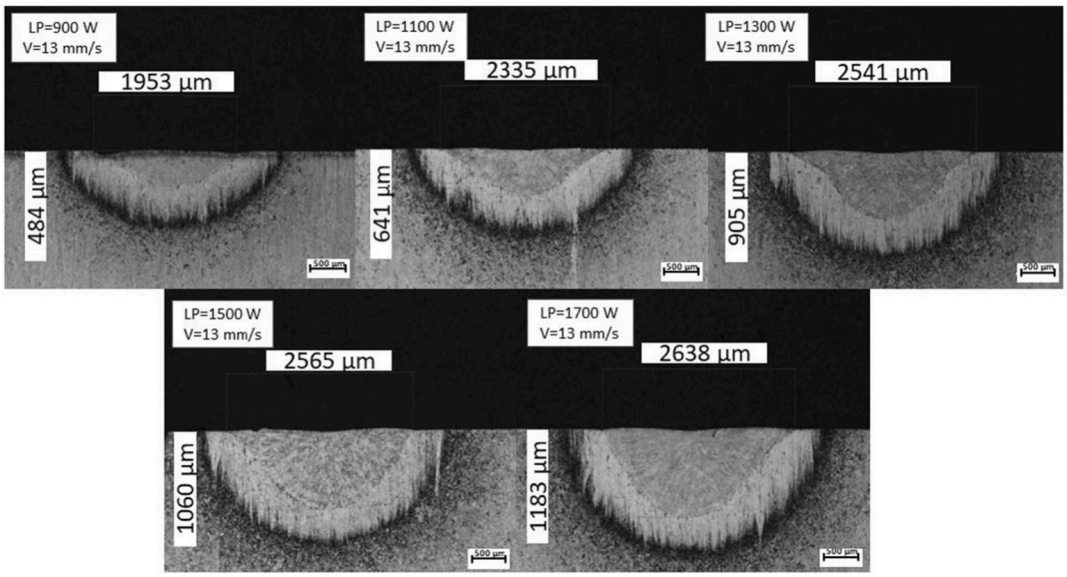

Figure 1.21 Geometrical results of the samples in accordance with the process parameters [64].

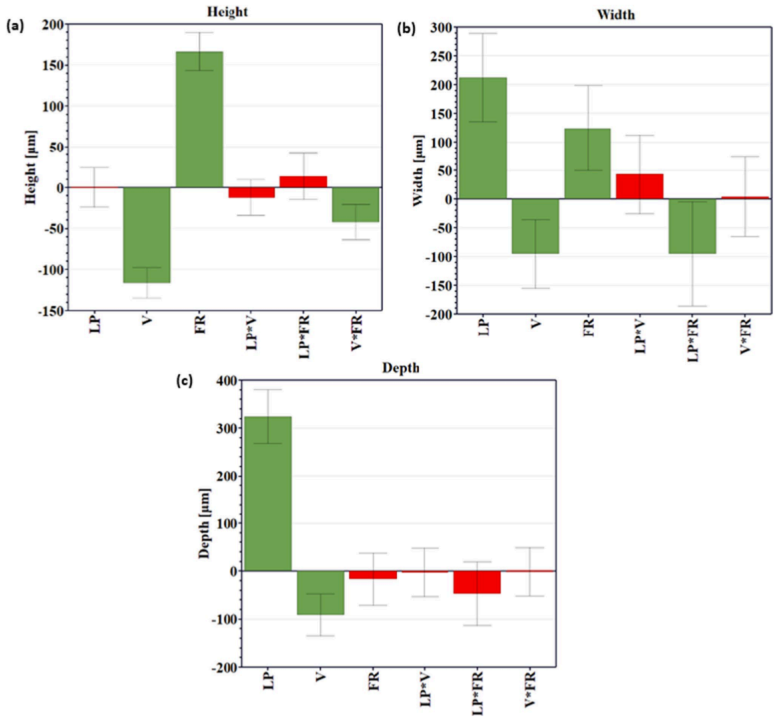

Figure 1.22 Statistical validation of the effect of the process parameters on the geometrical features of the depositions. Green bars represent the significant factor of each feature [64].

In terms of the microstructure, the authors confirmed that the specimens are composed of a martensitic matrix with primary δ-ferrite, observing that the presence of this phase increases with the increasing of the energy input. Figure 1.23 shows the different microstructures they observed in the samples; in particular, micrograph n. 3 is representative of the δ-ferrite content at the lowest energy input, while micrograph n. 5 is representative of the δ-ferrite content at the highest energy input.

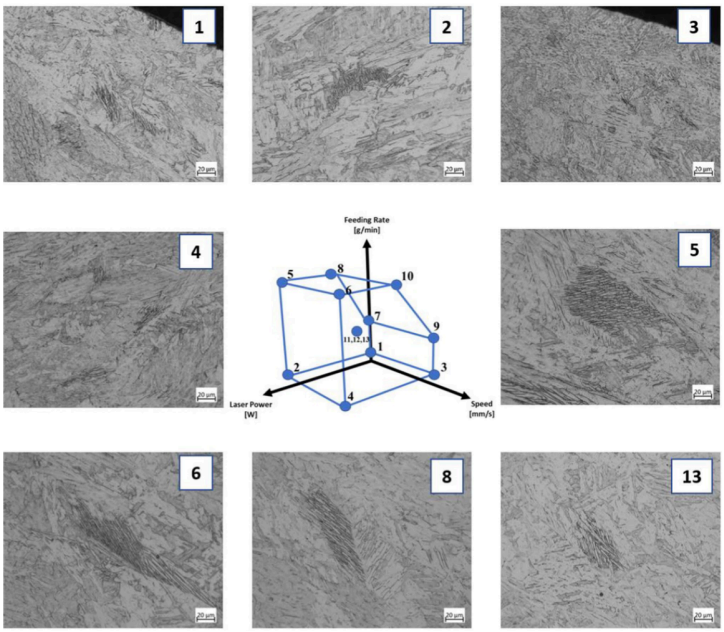

Figure 1.23 Micrographs of the different specimens showing different δ-ferrite contents [64].

In conclusion, the authors found that laser power has a strong impact on the geometrical features, while the energy input has the strongest effect on the distribution of martensite and δ-ferrite in the microstructure.

As stated in the studies found in the literature, in the 3D printing by L-DED of 17-4 PH stainless steel the selection of proper process parameters has a significant role in obtaining good quality parts. Both the laser power and the laser energy input seem to have a role that needs to be extremely controlled because not only affects the geometry, and so the dilution, of single tracks but also governs the microstructure of the deposited layers. Nevertheless, the role of these parameters needs to be deeply understood, so further experimental work is needed to improve the knowledge and optimize the process.

1.2.1.3 Effect of the heat treatment on 17-4 PH L-DED depositions

As mentioned before, during the L-DED a laser melts and solidify metallic powders but the control of process parameters is highly important to avoid geometrical discontinuities and inner defect formation. Although this topic has been already studied, the selection of process parameters has not been yet optimized, so the mechanical properties of 17-4 PH depositions may be improved. Nevertheless, an increase in mechanical properties can be currently obtained by the management of a proper post-fabrication heat treatment as mentioned in paragraph 1.1.5.

Among the different post-processing procedures, the most common are the thermal conventional treatments, hydrostatic stress thermal treatments, machining, surface finishing, and remelting procedures, which are usually employed to decrease the defect presence and increase their mechanical performance. Specifically, thermal post-processing treatments are one of the most feasible options to increase at low cost the properties of a DED part; among the different options, stress relieving, annealing, quenching, homogenization, solution heat treating, aging, and direct aging can be considered.

As stated before, PH stainless steels are usually heat treated to increase their mechanical behavior, performing a solution treatment followed by a rapid cooling (quenching) and a subsequent aging treatment. In the 17-4 PH stainless steel the aging, also mentioned as hardening (H) treatment, is the stage that promotes the reinforcement of the metal with nano-scale fine Cu-rich precipitate formation [65]. In accordance with the ASM handbook, in addition to a solution treatment carried out at 1038 °C for 30 min and a rapid cooling by quenching in water, an aging treatment within the range of 480 to 595 °C (900 1100 °F) is usually applied to the 17-4 PH alloy. The heat treatment route which considers aging performed a 480 °C for 1 hour is commonly known as H900 [66].

In the literature, studies regarding the heat treatment of 17-4 PH stainless steel are focused on the effect of the H900 applied on the mechanical properties of samples fabricated by both L-PBF and DED processes. Auguste et al [63] manufactured SLM specimens employing different 17-4 PH powder compositions. In accordance with the powder composition variation, the specimen's mechanical and microstructural properties varied as well. One of the powder specimens solidify mostly from the ferritic way while the other from the martensitic, the authors have found that when different heat treatments routes were applied, the aging at 480 °C for 1 hour produce an increase in hardness of those martensitic samples (samples named T480 in Figure 1.24). While the ferritic composition samples (T480 SLM, in Figure 1.24) require a prior homogenization treatment since during the solubilization the microstructure doesn't transform mostly in martensite. The authors confirm that with the homogenization treatment in both composition cases the hardness increase (H-SHT- T480 in Figure 1.24) considerably.

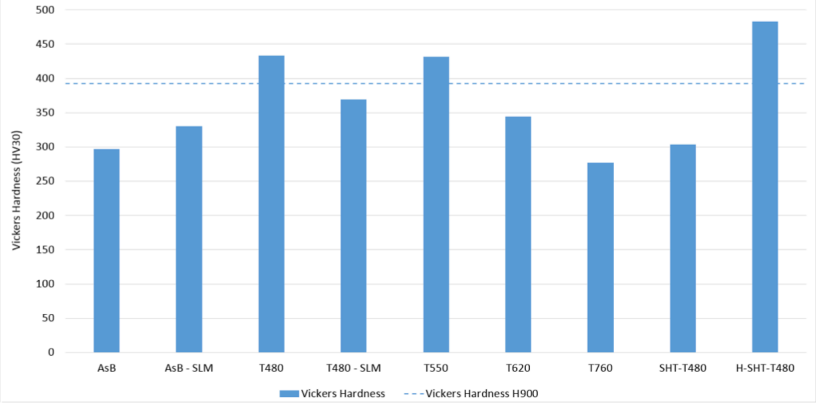

Figure 1.24 Hardness results of the different tested at different heat treatments [67].

Other studies, such as the one performed by Cheruvathur [68] regard the employment of a post-processing heat treatment on PBF-manufactured 17-4 PH samples studying the effect of the heat treatment in the homogenization of the martensite. The authors found that in this type of material the usual heat treatment suggested to relieve stresses has a weak effect to reach specific requirements of microstructure. So, the authors employed a homogenization treatment to promote a better ratio of microstructure, and with this fulfilled the hardness enhancement. Hsiao [68], performed an age-hardening treatment at a temperature higher than 620 °C on a 17-4 PH material, finding the presence of Cu-rich precipitates but also the re-formation of austenite at high temperatures, obtaining with this an increase in the hardness values but still having high-quantity of dislocations.

Mathoho et al. [30] in another hand performed a study in which the effect of the process parameters on the microstructural behavior of L-DED 17-4 PH specimens is analyzed. Besides to study the effect of post-processing (heat treatment) on the microstructure and microhardness across the as-built specimens, including the application of a homogenization stage of 1100°C for 2 hours followed by aging of 480 °C for 1 hour instead of applying the classical solution heat treatment. The results observed by the authors have demonstrated that after applying the heat treatment on the sample with less porosity the different stages showed a clearly change in microstructure. As observed in Figure 1.25 the as-built specimen demonstrates the presence of martensite and austenite, but when the homogenization was applied the austenite as well as the melt pool boundaries disappear, showing only martensite presence that continues present in the post-aging condition.

In conclusion, the authors have found that the as-built microstructure showed both martensite and retained austenite while homogenization and aging led to the suppression of the retained austenite and a further microhardness increase as observed in Figure 1.26.

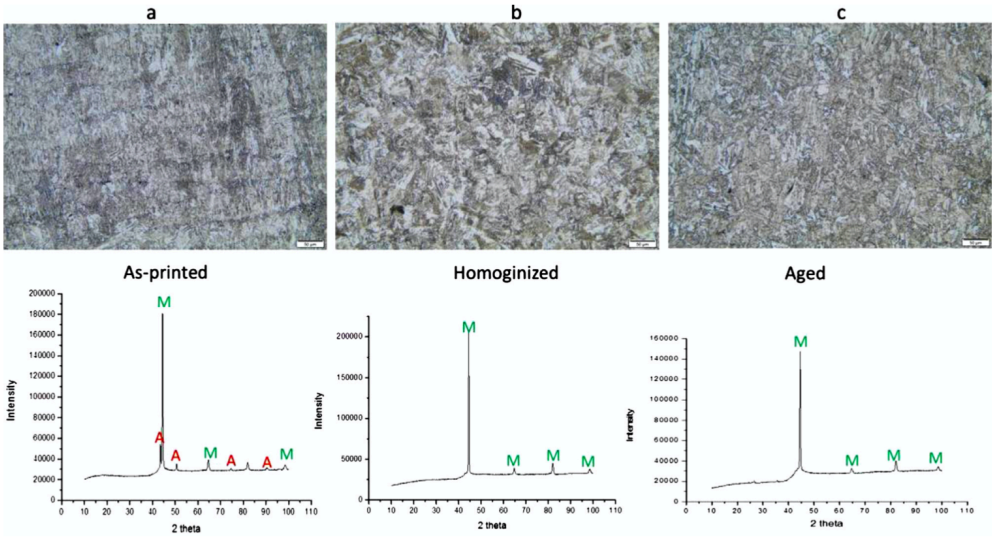

Figure 1.25 Microstructural comparison among the diverse stages of the modified H900 heat treatment with their respective XRD analysis [30].

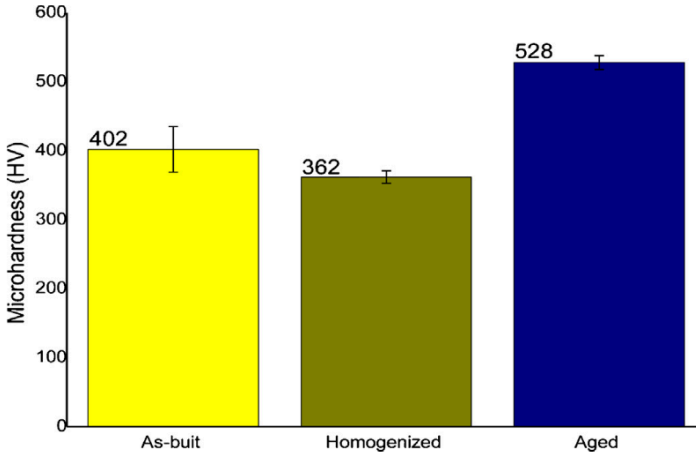

Figure 1.26 Microhardness across the different heat treatment stages [30].

Wee-Do Yoo et al. [69] performed a homogenization treatment followed by a solution and a long-term 400 °C aging treatment in order to investigate the microstructural behavior of the 17-4 PH stainless steel samples at different time conditions. The author found that when the homogenization time performed at 1149 °C increases the size of the δ-ferrite across the specimen decreases as well as its volume fraction. While the sample that was treated with only the solution heat treatment at 1038 °C presents lath martensite with a small fraction of elongated δ-ferrite and no precipitates were observed. However, when the temperature of the aging increases and the aging time moves up to 3060 hours, Cu-rich particles precipitates in the δ-ferrite: This phenomena decrease the mechanical performance of the alloy and can only be restored with a recovery H900 treatment in which the presence of the precipitates remain but the δ-ferrite is quite dissolved (Figure 1.27).

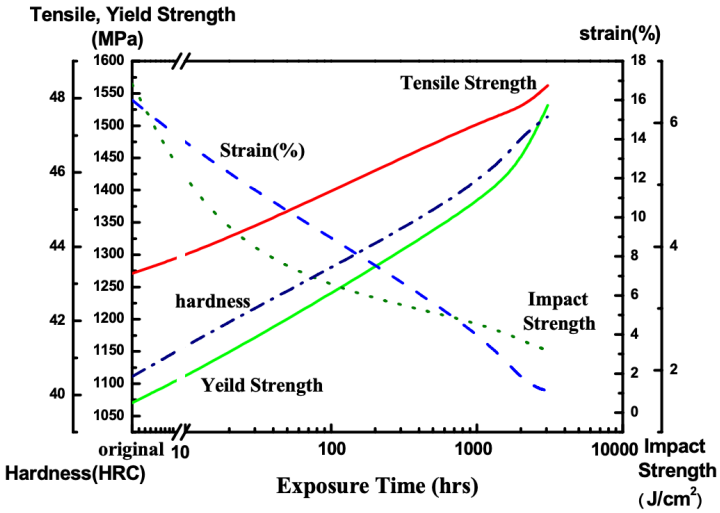

Figure 1.27 Mechanical property variation of the 17-4 PH SS in accordance with the 400 °C aging exposure [69].

Lashgari et al, [70] study the laser energy density effect across the microstructural and mechanical behavior of 17-4 PH L-PBF samples applying as well different post-heat treatment routes. The different heat thermal treatments containing a solubilization at 1040 °C, quenching in water, and aging at 472 °C for 1 hour. The authors have found that a strong relationship between the heat treatment route and the laser power energy density is depicted in the control the quantity of reverted austenite and Cu-rich precipitation formation. Since the solubilization treatment led to the retained austenite formation and precipitation of M_7C_3 carbides, increasing their presence when the time of the solubilization time increased from 1 to 4 hours but decreasing the volume fraction of the retained austenite. Clearly, Cu precipitation was observed when the aging treatment was applied and continuously increased as well as the volume fraction of the retained austenite when the time of the aging was prolonged. In terms of mechanical testing, it was observed that the initial energy density of the additively manufactured samples has a significant influence on the wear resistance of post-thermally treated samples and results in different wear behavior. Nevertheless, the samples have shown that the use of a conventional solution + aging treatment did not increase the hardness of the specimens due to the slow Cu diffusion, however, a change in the solubilization time regardless of the initial energy density employed, is assumed to be highly important for the microstructural evolution.

In 17-4 PH stainless steels fabricated by L-PBF and L-DED, the effects of post-fabrication heat treatments are not still completed understood. The evolution of microstructure during the heat treatment is complex due to both the adopted process parameters and the heat treatment parameters themselves. Some authors proposed the use of a typical H900 treatment; nevertheless, considering the obtained results it seems that a proper variation of time and temperature of both solubilization and aging treatments may induce an optimization of the microstructure, thus improving the mechanical properties. The aging treatment is the key to improve the mechanical properties because of the precipitation of the hardening nanoprecipitates; nevertheless, the peculiar microstructure of L-DED 17-4 PH stainless steel in the as-built condition could lead to optimization of the solution treatment too. Finally, it is worth noting that also the oversaturated condition of the as-built microstructure could be sufficient for improving the mechanical properties by a direct aging.

1.2.2 Cemented carbide (cermet) composites

Cemented carbides, also known as cermets, are very successful composite materials consisting of a ceramic part embedded into a metallic binder, in which the last one acts as a

ductile matrix for the material. Figure 1.28 shows the different classifications of these materials, mainly based on the nature of the ceramic phase [71].

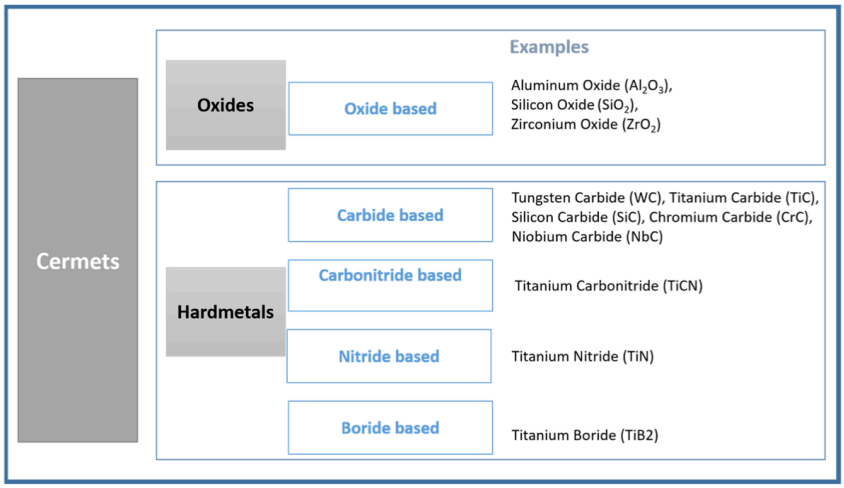

Figure 1.28 Cemented carbides classification [71].

Extraordinary hardness, toughness, high wear, and corrosion resistance are some of the features characterizing this kind of materials. Commonly produced via casting and powder metallurgy, the production of complex geometries often requires a post-processing method, e.g., machining, in order to obtain the final part. With the arrival of AM techniques, new manufacturing possibilities opened, however, the processing of this composites materials is still very challenging due to their high melting temperatures.

In literature, even if information related to the fabrication of these composites via AM processes is very lacking. It is worth noting that SLS, E-PBF, DED, and BJ processes are cited as possible additive manufacturing techniques suitable for fabricated cermet parts. A very important study carried out by Aramian [72] discusses the production of cermets through different additive manufacturing processes since this group of technologies is considered highly promising to reduce most of the constraints of the more traditional manufacturing methods employed for these kind of materials (see Figure 1.29).

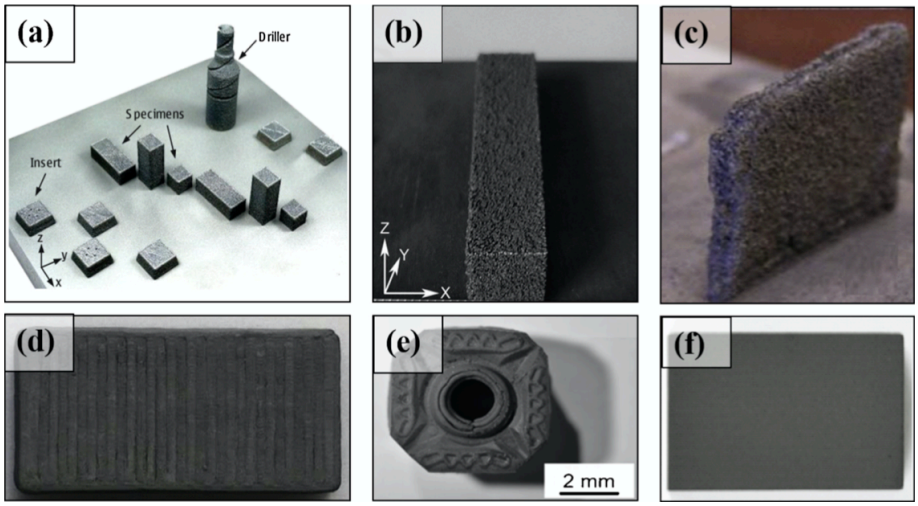

Figure 1.29 Cermets specimens produced by different AM processes a) SLM, b) DED, c) LENS, d) BJ, e) Extrusion-Based 3D printing, and f) gel printing [72].

Common applications of these materials cover cutting and forming of other materials, but they are also used as hard-facing materials in coating applications [72]–[76].

1.2.2.1 WC-Co composite

WC-Co was one of the first produced cermets and still one of the most widely used for cutting tools, mining, and molding due to their excellent mechanical performances including good strength, wear resistance, high hardness, and high melting point (200-400 °C). This cermet usually contains from 4 % to 30 % of Co which increases the fracture toughness and very hard WC monocarbide particles embedded into the binder with an average particle size of 0.1 – 20 μm. The size of the WC particles, the Co content as well as the carbide particles distribution are key factors controlling the mechanical properties of these materials [74].

WC-Co cermets are characterized by their unique core-shell type microstructure, consisting of mainly three phases: a hard phase, a metal binder, and a surrounding phase. In the following, a brief description of these phases is reported.

1.2.2.1.1 WC phase

The principal structure of a WC-Co material comprises a WC phase that forms a strong and hard continuous skeleton as well as compounds of W-C-Co, CoW, and CoC, formed within the binder phase. Tungsten mainly combines with carbon in order to form the following carbides: WC, also known as δ-WC, $WC_{0.5}$ (β-W_2C, named lower tungsten carbide with other two polymorphs; α-W_2C and γ-W_2C), and γ-WC_{1-x} which are stable at a specific temperature. $WC_{0.5}$ forms from a eutectoid reaction between 2516 °C and 1250 °C while γ-WC_{1-x} forms at a temperature above 2516 °C, resulting from the eutectoid reaction between β-W_2C and δ-WC. These phase transformations can be found in the W-C phase diagram depicted in Figure 1.30.

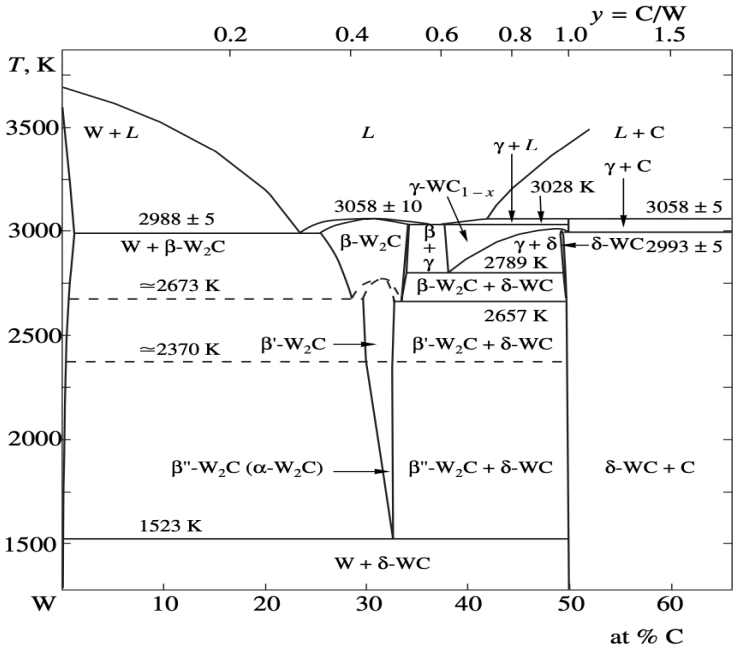

Figure 1.30 W-C phase diagram [77].

1.2.2.1.2 Binder phase

Co is the most used metal binder for WC cermets with a mass fraction within the range of 3-30 wt.%. Co is usually employed as a binder because of its excellent carbide wetting and suitable mechanical properties. In general, Co is a ferromagnetic metal that could be present in two crystal structures, FCC, and HCP, and can undergo a martensitic-type phase transition. The transformation of Co is also highly affected by the amount of WC dissolved within the binder, the distance between two carbide grains (binder mean free path), and the solubility of WC grains in Co which usually depends on the temperature.

1.2.2.1.3 Carbides

Precipitates are generally observed in the binder phase of cemented carbides in the shape of non-metallic impurities, graphite, carbides, and intermetallic compounds during the cooling of these materials.

C content has a strong effect on the mechanical properties; Figure 1.31 shows the phase diagram of a WC-Co system with 10 % of Co. When the C content is low, the material generates the eta phase (η), i.e., complex carbides (also nominated ternary compound) composed of W, Co or Fe, and C that can exist in two main forms, either M_6C carbide ranging from M_3W_3C, $Co_{32}W_{28}C$ to Co_2W_4C or $M_{12}C$ carbide with Co_6W_6C as the most probable due to the carbon deficiency during the processing. This phase is generally brittle and detrimental for the mechanical properties. On the contrary, if the C content is high free graphite phase is present in the microstructure [75]–[79].

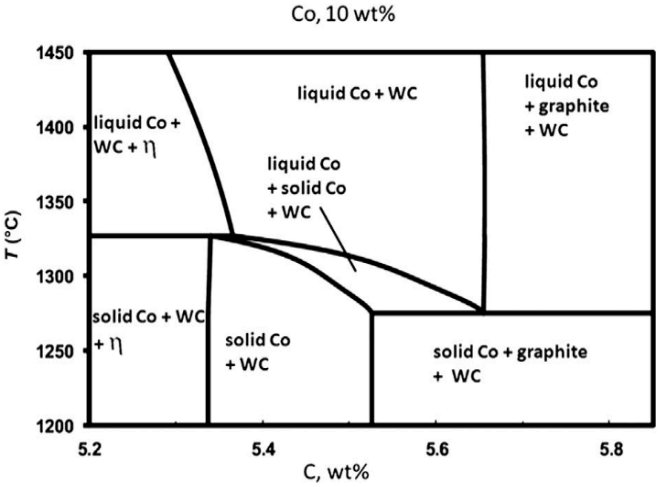

Figure 1.31 Phase diagram of a WC-10%Co system with carbon variation [79].

The morphologies of the η phase range from finely dispersed particles at low carbon deficiency to large areas at high carbon deficiency.

The microstructure of these materials is usually composed of polygonal WC grains of different sizes embedded across some rounded zones which are known to be partially dissolved WC grains with a high presence of the η phase. The quantity and presence of these zones at room temperature are commonly determined as an effect of both the cooling rate and the C content [80]. In Figure 1.32 a typical WC-Co microstructure of a laser cladding, obtained at specific process parameters, is shown [80]. The authors detailed across their study an explanation of the microstructural, wear, and hardness evolution that occurred across the performed coatings in relation to the different parameters employed. The authors have found that when high scanning speed and higher energy density are employed the dissolution of the WC particles is more prominent besides that the lamellar WC and herringbone carbide formation is more consisting, besides demonstrating better densification, good bonding, and the highest hardness increase.

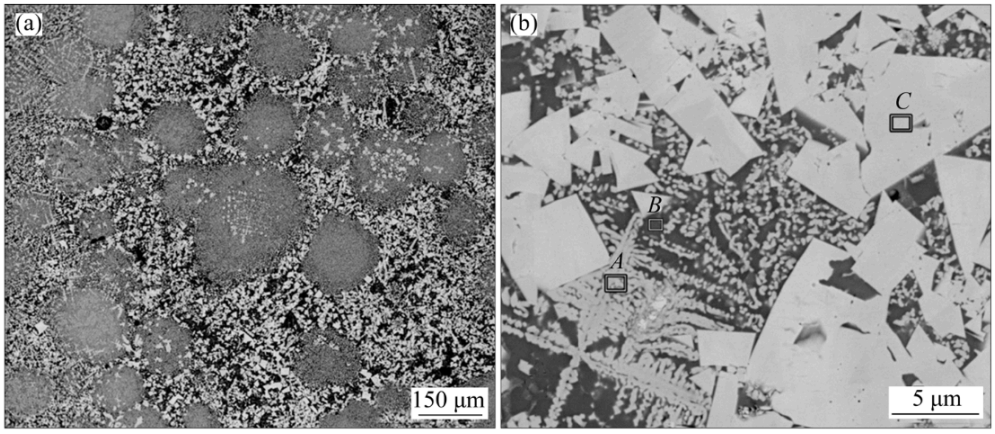

Figure 1.32 a) Morphology of carbides on surface of coatings; (b) Morphology of carbides at the edge of residual WC−12Co particles [80].

1.2.2.2 Effect of the process parameters on WC-Co L-DED depositions

The L-DED technique is one of the AM processes employed to deposit this kind of hard metal materials since during the process the high temperatures reached for the laser beam promote the melting of the WC-Co powder. As observed in the previous 17-4 PH cases of study is useful to study the geometrical and macrostructure behavior of the samples optimize the future multilayer depositions and avoid non-desirable defects [79].

Although the literature related to this kind of processed samples is very scarce, some studies dealt with the use of the SLM technique to process these hard-facing metals. Fortunato et al [74] performed the deposition of the WC-Co samples varying the powder features and their compositions to establish the optimal process parameters. The authors have found that a multi-pass strategy (also known as remelting technique) is feasible to guarantee higher energy densities and avoid cracks across the specimens, maintaining constant both the laser power and the scanning strategy. They concluded that the higher the Co content, the less brittle the component is, demonstrating less crack formation.

In comparison, Fries et al [81] found that if WC-Co samples were performed via L-PBF the influence of the process parameters, in particular with the laser power in the range of 140-360 W, is highly important for the crack and porosity formation across the depositions. As can be observed in Figure 1.33, even if the number of pores decreases in size with the increase of the laser power, the presence of small micropores still remains.

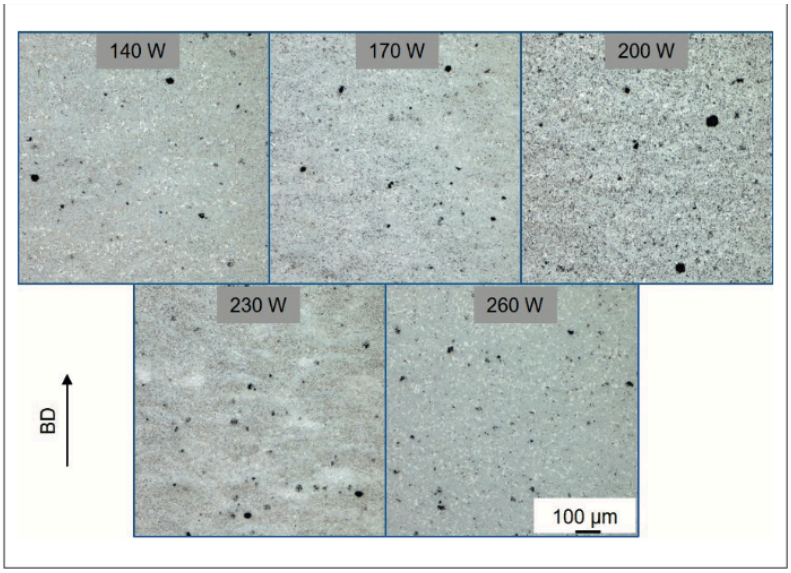

Figure 1.33 Optical micrographs of the as-built WC-17Co specimens produced at different laser power parameters [81].

The same authors observed that not only the laser power has a strong effect on the microstructure or on the number of defects formed during the depositions. In fact, they showed that at higher laser power values both the number of carbides and their size increase, thus promoting a strong effect on the hardness of the specimens; the volume fraction of the porosity increases as well. To reduce the impact of these problems, the authors mentioned that the use of a HIP post-treatment is of great importance for closing the pores and so for improving the density of the samples (see Figure 1.34).

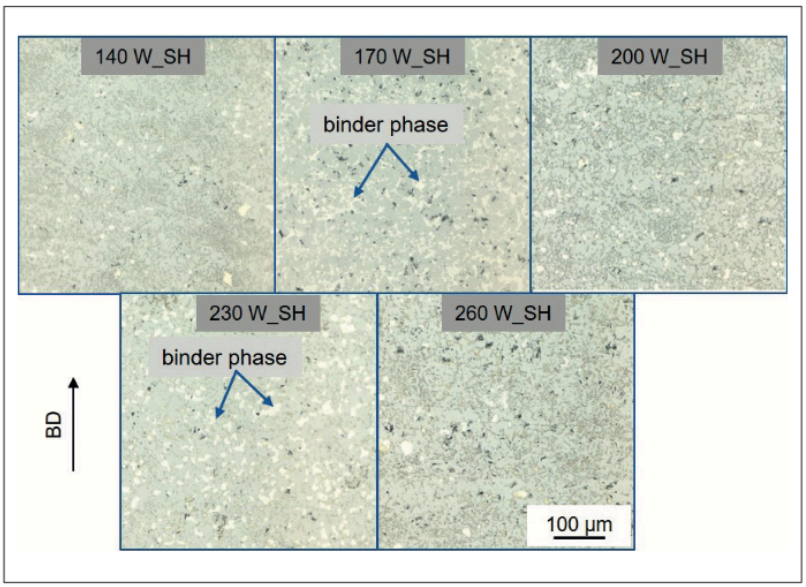

Figure 1.34 Optical micrographs of the microstructure after the HIP treatment [81].

In the literature, a limited number of papers dealing with WC-Co materials processed via DED can be found and it is even more difficult to find specific works with emphasis on the effect of the process parameters. Among some of the studies near this kind of material the one performed by Woo-Jin Lee [69] focused on the effect of the particle shape of WC-Ni powder during DED depositions, maintaining constants of the other process parameters. Both irregular and spherical powers were tested as two different shapes of the particles. As a result, the authors found that the use of particles with different shapes influences the integrity of the deposited part; in fact, as can be observed in Figure 1.35, the irregular shape of the powder particles significantly affected the geometry of the deposited part itself.

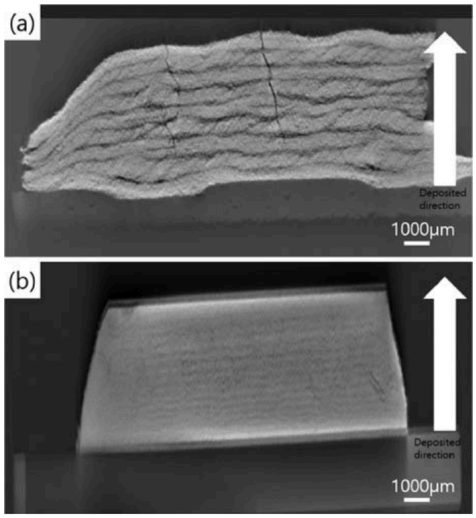

Figure 1.35 DED WC-Ni samples performed with different powders a) irregular, b) spherical [69].

In addition, Kyoung-Wook et al [82] performed a study regarding the effect of different process parameters, in particular the scanning speed and the hatch spacing, when WC-12Co samples are deposited via the L-DED process. Three different process conditions named A, B, and C in accordance with the laser power energy density (higher, low, and medium respectively) were fabricated and analyzed. It was found that the laser energy density is strictly correlated to the formation of porosity: the higher is the laser energy density, the better is the densification of the parts.

As observed in Figure 1.36, the sample under condition A is the one with the less presence of porosity, even if lack of fusions and possible cracks can be observed.

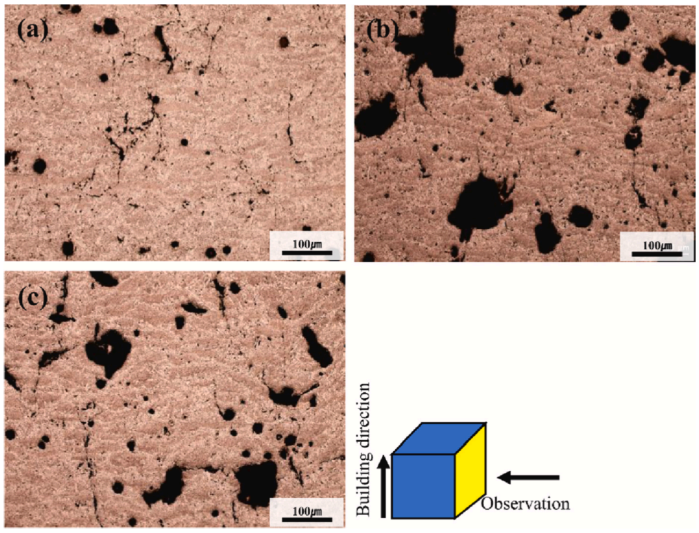

Figure 1.36 Microstructures across WC-12Co DED samples at different parameters (A, B, C) [82].

The authors also performed XRD analysis, finding out the WC, Co, and eta phase peaks are in accordance with the composition of the fabricated samples (see Figure 1.37). Nevertheless, the amount of coarse WC phases and secondary phases was highest in the A condition; this condition is the one characterized by the highest volume energy density (VED) among the three materials.

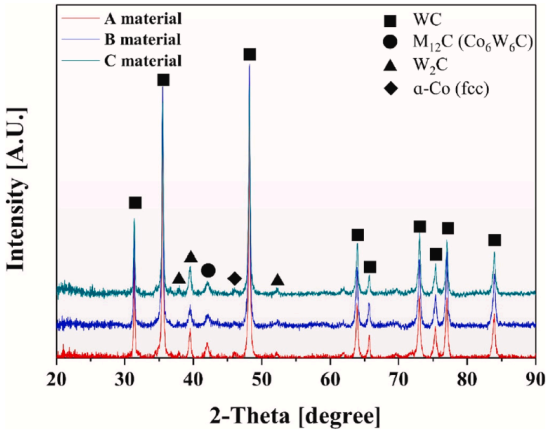

Figure 1.37 XRD analysis performed on the deposited samples [82].

Another important process parameter in the deposition of WC-Co cermets is the scanning pattern strategy that the laser follows during the depositions. A few studies approached the analysis of the scanning pattern strategies used across the laser-based additive manufacturing techniques. The scanning strategy as cited by [83] is the spatial moving pattern of the energy beam, for a single-layer scan. This parameter varies concerning

the different directions of the scanning, sequence, vector scanning rotational angle, scanning vector length, time, and hatch spacing. It was found that the selection of different scanning strategies may have a pivotal role in the presence or in the absence of voids or pores inside of the deposited samples; the heat input accumulation changes from pattern to pattern promoting specific overlapping between adjacent melting pools and/or different melting behaviors of powders, as observed in Figure 1.38 [84].

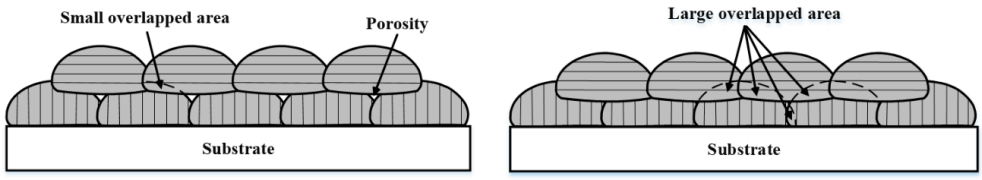

Figure 1.38 Schematic image of different overlapping areas resulted from different scanning strategies employed during the fabrication of samples via L-DED [84].

As reported in the study performed by Jia et al. [83], the most adopted scanning strategies are the unidirectional and the bidirectional (zig-zag). Another interesting and high-performance scanning pattern is the chessboard, also named island strategy, in which the main area interested by the scan path is divided into small cells, each of them scanned by the laser according to different directions. Most of the possible strategies are described in Figure 1.39.

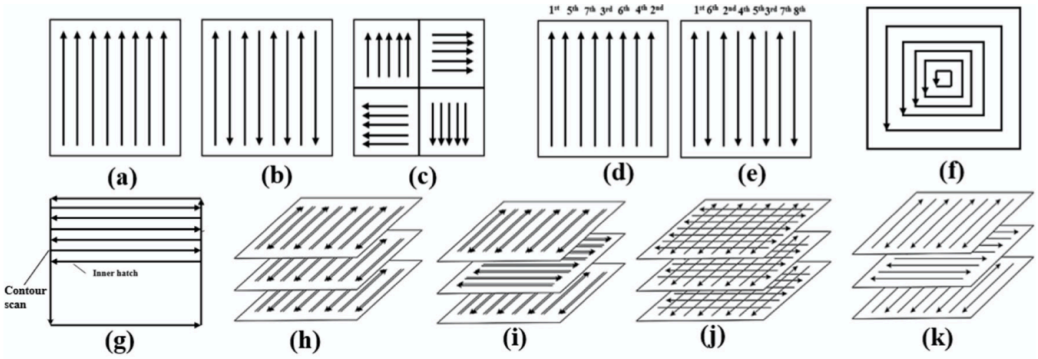

Figure 1.39 Scheme of different scanning strategies employed during the AM process. A) unidirectional, b) bidirectional/ zig-zag, c) island, d) unidirectional scan with a variety of sequences, e) bidirectional scan with a variation of the sequence, f) helix, g) contour scan, h) bidirectional with a double pass, i) bidirectional with double pass and 90 ° rotation, j) cross scan and k) bidirectional single pass and 90 ° rotation [83].

The authors of the study mentioned that a reasonable selection of the scanning strategy is necessary since it has a strong effect on the microstructure, mechanical properties, and residual stresses. They also mentioned that sometimes remelting is beneficial to improve the microstructure and to increase the mechanical properties.

Other authors, such as Liu [85] studied the effect of the scan pattern of the laser on the mechanical properties caused by the thermal mismatch during the process, besides the reduction of material deformation and residual stresses. Nevertheless, in the conclusion of their works, they assessed that a proper scanning strategy selection is fundamental for the soundness of the deposited material even if the scanning can be optimized, synergically with the other process parameters. In addition, Kandice S.B. Ribiero et al [86] evaluated the influence of several deposition paths and beads stepover on the dimensions and forms of AISI 316L parts, but also checking the evolution of microhardness and density according to the selected deposition paths and beads stepover. The authors performed different specimens at diverse process parameters, including four deposition strategies as observed in Figure 1.40.

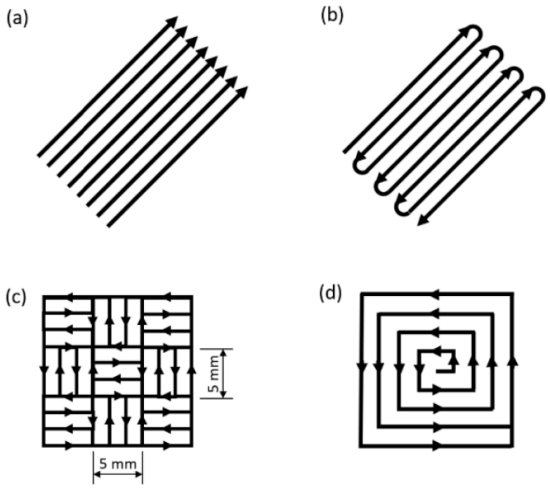

Figure 1.40 Scanning strategy deposition used across the performed study. a) linear, b) zig-zag, c) chessboard, and d) contour [86].

As a summary of this brief theoretical background regarding the 3D printing of WC-Co cermets, it is worth noting that the control of the DED process parameters needs to be improved. The laser power and scanning strategy as well as the energy density input have been found to be the parameters with a major effect on the microstructure and, in particular, on the defect formation across the depositions. It has been observed that the research in this thematic area (WC-Co processed with DED is still open. Topics related to the optimization of process parameter optimization and of post-processing treatments, without resorting to the HIP treatment which is highly beneficial but expensive for the cost production of a DED part, are of great interest for the scientific community working for the improvement of knowledge in L-DED processes.

1.3 REFERENCES

[1] ASTM, "Standard Terminology for Additive Manufacturing Technologies F2792." doi: 10.1520/F2792-09.

[2] D. Herzog, V. Seyda, E. Wycisk, and C. Emmelmann, "Additive manufacturing of metals," *Acta Mater*, vol. 117, pp. 371–392, 2016, doi: 10.1016/j.actamat.2016.07.019.

[3] M. Aliakbari, "Additive Manufacturing: State-of-the-Art, Capabilities, and Sample Applications with Cost Analysis," 2012.

[4] ASTM, "International Standard - ISO/ASTM 52900. Additive manufacturing - General principles," *ASTM*. pp. 1–28, 2015.

[5] S. Ganesh Sarvankar and S. N. Yewale, "Additive Manufacturing in Automobile Industry," *International Journal of Research in Aeronautical and Mechanical Engineering*, vol. 7, no. 4, pp. 1–10, 2019.

[6] R. Leal *et al.*, "Additive manufacturing tooling for the automotive industry," *International Journal of Advanced Manufacturing Technology*, vol. 92, no. 5–8, pp. 1671–1676, Sep. 2017, doi: 10.1007/s00170-017-0239-8.

[7] A. Charles, A. Hofer, A. Elkaseer, and S. G. Scholz, "Additive Manufacturing in the Automotive Industry and the Potential for Driving the Green and Electric Transition," in *Smart Innovation, Systems and Technologies*, Springer Science and Business Media Deutschland GmbH, 2022, pp. 339–346. doi: 10.1007/978-981-16-6128-0_32.

[8] D. Chantzis *et al.*, "Review on additive manufacturing of tooling for hot stamping", doi: 10.1007/s00170-020-05622-1/Published.

[9] C. Pinna, L. Ramundo, F. G. Sisca, C. M. Angioletti, M. Taisch, and S. Terzi, "Additive Manufacturing applications within Food industry: an actual overview and

future opportunities," in *XXI Summer School "Francesco Turco" - Industrial Systems Engineering18*,
[10] Mohd. Javaid and A. Haleem, "Additive manufacturing applications in medical cases: A literature based review," *Alexandria Journal of Medicine*, vol. 54, no. 4, pp. 411–422, Dec. 2018, doi: 10.1016/j.ajme.2017.09.003.
[11] B. Sun, Q. Ma, X. Wang, J. Liu, and M. R. M. Rejab, "Additive manufacturing in medical applications: A brief review," *IOP Conf Ser Mater Sci Eng*, vol. 1078, no. 1, p. 012007, Feb. 2021, doi: 10.1088/1757-899x/1078/1/012007.
[12] C. Culmone, G. Smit, and P. Breedveld, "Additive manufacturing of medical instruments: A state-of-the-art review," *Additive Manufacturing*, vol. 27. Elsevier B.V., pp. 461–473, May 01, 2019. doi: 10.1016/j.addma.2019.03.015.
[13] D. Svetlizky *et al.*, "Laser-based directed energy deposition (DED-LB) of advanced materials," *Materials Science and Engineering A*, vol. 840. Elsevier Ltd, Apr. 18, 2022. doi: 10.1016/j.msea.2022.142967.
[14] R. Singh *et al.*, "Powder bed fusion process in additive manufacturing: An overview," in *Materials Today: Proceedings*, Elsevier Ltd, 2019, pp. 3058–3070. doi: 10.1016/j.matpr.2020.02.635.
[15] P. C. Priarone, V. Lunetto, E. Atzeni, and A. Salmi, "Laser powder bed fusion (L-PBF) additive manufacturing: On the correlation between design choices and process sustainability," in *Procedia CIRP*, Elsevier B.V., 2018, pp. 85–90. doi: 10.1016/j.procir.2018.09.058.
[16] D. Herzog, V. Seyda, E. Wycisk, and C. Emmelmann, "Additive manufacturing of metals," *Acta Mater*, vol. 117, pp. 371–392, Sep. 2016, doi: 10.1016/j.actamat.2016.07.019.
[17] E. J. Schindelholz, M. A. Melia, and J. M. Rodelas, "Corrosion of Additively Manufactured Stainless Steels—Process, Structure, Performance: A Review," *Corrosion*, vol. 77, no. 5. NACE International, pp. 484–503, May 01, 2021. doi: 10.5006/3741.
[18] A. Saboori, A. Aversa, G. Marchese, S. Biamino, M. Lombardi, and P. Fino, "Application of directed energy deposition-based additive manufacturing in repair," *Applied Sciences (Switzerland)*, vol. 9, no. 16. MDPI AG, Aug. 01, 2019. doi: 10.3390/app9163316.
[19] B. Freire, M. Babcinschi, L. Ferreira, B. Señaris, F. Vidal, and P. Neto, "Direct energy deposition: A complete workflow for the additive manufacturing of complex shape parts," in *Procedia Manufacturing*, Elsevier B.V., 2020, pp. 671–677. doi: 10.1016/j.promfg.2020.10.094.
[20] C. Bourlet, S. Zimmer-Chevret, R. Pesci, R. Bigot, A. Robineau, and F. Scandella, "Microstructure and mechanical properties of high strength steel deposits obtained by Wire-Arc Additive Manufacturing," *J Mater Process Technol*, vol. 285, Nov. 2020, doi: 10.1016/j.jmatprotec.2020.116759.
[21] S. C. A. Costello, C. R. Cunningham, F. Xu, A. Shokrani, V. Dhokia, and S. T. Newman, "The state-of-the-art of wire arc directed energy deposition (WA-DED) as an additive manufacturing process for large metallic component manufacture," *Int J Comput Integr Manuf*, pp. 1–44, Jan. 2023, doi: 10.1080/0951192X.2022.2162597.
[22] A. Saboori, A. Aversa, G. Marchese, S. Biamino, M. Lombardi, and P. Fino, "Microstructure and mechanical properties of AISI 316L produced by directed energy deposition-based additive manufacturing: A review," *Applied Sciences (Switzerland)*, vol. 10, no. 9. MDPI AG, May 01, 2020. doi: 10.3390/app10093310.
[23] G. Piscopo, E. Atzeni, A. Saboori, and A. Salmi, "An Overview of the Process Mechanisms in the Laser Powder Directed Energy Deposition," *Applied Sciences (Switzerland)*, vol. 13, no. 1. MDPI, Jan. 01, 2023. doi: 10.3390/app13010117.

[24] J. L. Dávila, P. I. Neto, P. Y. Noritomi, R. T. Coelho, and J. V. L. da Silva, "Hybrid manufacturing: a review of the synergy between directed energy deposition and subtractive processes," *International Journal of Advanced Manufacturing Technology*, vol. 110, no. 11–12. Springer Science and Business Media Deutschland GmbH, pp. 3377–3390, Oct. 01, 2020. doi: 10.1007/s00170-020-06062-7.

[25] A. Dass and A. Moridi, "State of the art in directed energy deposition: From additive manufacturing to materials design," *Coatings*, vol. 9, no. 7, 2019, doi: 10.3390/COATINGS9070418.

[26] D.-G. Ahn, "Directed Energy Deposition (DED) Process: State of the Art," *International Journal of Precision Engineering and Manufacturing - Green Technology*, vol. 8, no. 2, pp. 703–742, Mar. 2021, doi: 10.1007/s40684-020-00302-7.

[27] D. Svetlizky *et al.*, "Directed energy deposition (DED) additive manufacturing: Physical characteristics, defects, challenges, and applications," *Materials Today*, vol. 49, pp. 271–295, Oct. 2021, doi: 10.1016/j.mattod.2021.03.020.

[28] ASM International. Handbook Committee., *ASM handbook*, vol. 24. 2020.

[29] H. Gu, H. Gong, D. Pal, K. Rafi, T. Starr, and B. Stucker, "Influences of Energy Density on Porosity and Microstructure of Selective Laser Melted 17-4PH Stainless Steel."

[30] I. Mathoho, E. T. Akinlabi, N. Arthur, and M. Tlotleng, "Impact of DED process parameters on the metallurgical characteristics of 17-4 PH SS deposited using DED," *CIRP J Manuf Sci Technol*, vol. 31, no. 2019, pp. 450–458, 2020, doi: 10.1016/j.cirpj.2020.07.007.

[31] S. Cheruvathur, E. A. Lass, and C. E. Campbell, "Additive Manufacturing of 17-4 PH Stainless Steel: Post-processing Heat Treatment to Achieve Uniform Reproducible Microstructure," *Jom*, vol. 68, no. 3, pp. 930–942, 2016, doi: 10.1007/s11837-015-1754-4.

[32] A. Eliasu, A. Czekanski, and S. Boakye-Yiadom, "Effect of laser powder bed fusion parameters on the microstructural evolution and hardness of 316L stainless steel," *The International Journal of Advanced Manufacturing Technology,* vol. 113, pp. 2651–2669, 2021, doi: 10.1007/s00170-021-06818-9/Published.

[33] M. C. Sow *et al.*, "Influence of beam diameter on Laser Powder Bed Fusion (L-PBF) process," vol. 36, pp. 1–11, 2020, doi: 10.1016/j.addma.2020.101532ï.

[34] Z. Wang, B. He, Z. Song, L. Lan, G. Lu, and S. Gao, "Optimization of the Process Parameters of Laser Beam Powder Bed Fusion GTD222 Nickel-Based Superalloy Based on Two Laser Energy Densities," *Metals (Basel)*, vol. 12, no. 7, Jul. 2022, doi: 10.3390/met12071154.

[35] P. Ferro, R. Meneghello, G. Savio, and F. Berto, "A modified volumetric energy density-based approach for porosity assessment in additive manufacturing process design," *The International Journal of Advanced Manufacturing Technology,* vol. 110, pp. 1911–1921, 2020, doi: 10.1007/s00170-020-05949-9/Published.

[36] L. Costa *et al.*, "A simplified semi-empirical method to select the processing parameters for laser clad coatings," in *Materials Science Forum*, Trans Tech Publications Ltd, 2003, pp. 385–394. doi: 10.4028/www.scientific.net/msf.414-415.385.

[37] B. Bax, R. Rajput, R. Kellet, and M. Reisacher, "Systematic evaluation of process parameter maps for laser cladding and directed energy deposition," *Addit Manuf*, vol. 21, pp. 487–494, May 2018, doi: 10.1016/j.addma.2018.04.002.

[38] U. de Oliveira, V. Ocelík, and J. T. M. de Hosson, "Analysis of coaxial laser cladding processing conditions," *Surf Coat Technol*, vol. 197, no. 2–3, pp. 127–136, Jul. 2005, doi: 10.1016/j.surfcoat.2004.06.029.

[39] A. Bayode, E. T. Akinlabi, and S. Pityana, “Microstructure and Microhardness of 17-4 PH Stainless Steel Made by Laser Metal Deposition,” in *World Congress on Engineering and Computer Science*, 2016, p. 1040.

[40] A. Dass and A. Moridi, “State of the art in directed energy deposition: From additive manufacturing to materials design,” *Coatings*, vol. 9, no. 7. MDPI AG, 2019. doi: 10.3390/COATINGS9070418.

[41] E. M. Lee, G. Y. Shin, H. S. Yoon, and D. S. Shim, “Study of the effects of process parameters on deposited single track of M4 powder based direct energy deposition,” *Journal of Mechanical Science and Technology*, vol. 31, no. 7, pp. 3411–3418, Jul. 2017, doi: 10.1007/s12206-017-0239-5.

[42] M. O. Gushchina *et al.*, “Effect of Scanning Strategy on Mechanical Properties of Ti-6Al-4V Alloy Manufactured by Laser Direct Energy Deposition,” *J Mater Eng Perform*, vol. 31, no. 4, pp. 2783–2791, Apr. 2022, doi: 10.1007/s11665-021-06407-7.

[43] M. Liu, A. Kumar, S. Bukkapatnam, and M. Kuttolamadom, “A Review of the anomalies in Directed Energy Deposition (DED) processes and potential solutions.”

[44] P. Y. Lin, F. C. Shen, K. T. Wu, S. J. Hwang, and H. H. Lee, “Process optimization for directed energy deposition of SS316L components,” *International Journal of Advanced Manufacturing Technology*, vol. 111, no. 5–6, pp. 1387–1400, Nov. 2020, doi: 10.1007/s00170-020-06113-z.

[45] Arianna Gennari, “Influence of Directed Energy Deposition (DED) parameters on microstructural features of AISI 316L steel,” 2017.

[46] K. Sindo, *Welding Metallurgy*, Second. New Jersey: Wiley.

[47] I. Hemmati, V. Ocelík, and J. T. M. de Hosson, “Microstructural characterization of AISI 431 martensitic stainless steel laser-deposited coatings,” *J Mater Sci*, vol. 46, no. 10, pp. 3405–3414, May 2011, doi: 10.1007/s10853-010-5229-2.

[48] M. H. Farshidianfar, A. Khajepour, and A. P. Gerlich, “Effect of real-time cooling rate on microstructure in Laser Additive Manufacturing,” *J Mater Process Technol*, vol. 231, pp. 468–478, May 2016, doi: 10.1016/j.jmatprotec.2016.01.017.

[49] C. Zeng, W. Tian, W. H. Liao, and L. Hua, “Microstructure and porosity evaluation in laser-cladding deposited Ni-based coatings,” *Surf Coat Technol*, vol. 294, pp. 122–130, May 2016, doi: 10.1016/j.surfcoat.2016.03.083.

[50] M. Erfanmanesh, H. Abdollah-Pour, H. Mohammadian-Semnani, and R. Shoja-Razavi, “An empirical-statistical model for laser cladding of WC-12Co powder on AISI 321 stainless steel,” *Opt Laser Technol*, vol. 97, pp. 180–186, Dec. 2017, doi: 10.1016/j.optlastec.2017.06.026.

[51] C. Zhong, A. Gasser, T. Schopphoven, and R. Poprawe, “Experimental study of porosity reduction in high deposition-rate Laser Material Deposition,” *Opt Laser Technol*, vol. 75, pp. 87–92, Jul. 2015, doi: 10.1016/j.optlastec.2015.06.016.

[52] P. Bajaj, A. Hariharan, A. Kini, P. Kürnsteiner, D. Raabe, and E. A. Jägle, “Steels in additive manufacturing: A review of their microstructure and properties,” *Materials Science and Engineering A*, vol. 772, Jan. 2020, doi: 10.1016/j.msea.2019.138633.

[53] C. Rowolt, B. Milkereit, A. Springer, C. Kreyenschulte, and O. Kessler, “Dissolution and precipitation of copper-rich phases during heating and cooling of precipitation-hardening steel X5CrNiCuNb16-4 (17-4 PH),” *J Mater Sci*, vol. 55, no. 27, pp. 13244–13257, Sep. 2020, doi: 10.1007/s10853-020-04880-4.

[54] L. Zai *et al.*, “Laser powder bed fusion of precipitation-hardened martensitic stainless steels: A review,” *Metals*, vol. 10, no. 2. MDPI AG, Feb. 01, 2020. doi: 10.3390/met10020255.

[55] I. Gibson, D. Rosen, and B. Stucker, *Additive manufacturing technologies: 3D printing, rapid prototyping, and direct digital manufacturing, second edition*. Springer New York, 2015. doi: 10.1007/978-1-4939-2113-3.

[56] R. Narayan, *Rapid Prototyping of Biomaterials*, Second Edition. in Woodhead Publishing Series in Biomaterials. Woodhead Publishing, 2020. doi: https://doi.org/10.1016/B978-0-08-102663-2.09991-3.
[57] A. A. Adeyemi, E. Akinlabi, R. M. Mahamood, K. O. Sanusi, S. Pityana, and M. Tlotleng, "Influence of laser power on microstructure of laser metal deposited 17-4 ph stainless steel," *IOP Conf Ser Mater Sci Eng*, vol. 225, p. 012028, Aug. 2017, doi: 10.1088/1757-899x/225/1/012028.
[58] R. : M. Dabalà, "17-4 PH Ottenuto mediante pressatura isostatica a caldo."
[59] N. W. Makoana, H. Moller, H. Burger, M. Tlotleng, and I. Yadroitsev, "Evaluation of single tracks of 17-4PH steel manufactured at different power densities and scanning speeds by selective laser melting," *South African Journal of Industrial Engineering*, vol. 27, no. 3SpecialIssue, pp. 210–218, 2016, doi: 10.7166/27-3-1668.
[60] Z. Yu *et al.*, "Effect of laser remelting processing on microstructure and mechanical properties of 17-4 PH stainless steel during laser direct metal deposition," *J Mater Process Technol*, vol. 284, Oct. 2020, doi: 10.1016/j.jmatprotec.2020.116738.
[61] A. Ziewiec, A. Zielińska-Lipiec, and E. Tasak, "Microstructure of welded joints of X5CrNiCuNb 16-4 (17-4 PH) martensitic stainlees steel after heat treatment," *Archives of Metallurgy and Materials*, vol. 59, no. 3, pp. 965–970, 2014, doi: 10.2478/amm-2014-0162.
[62] A. S. Murthy, "Role of alloy additions on strengthening in 17-4 PH stainless steel," 2012. [Online]. Available: https://scholarsmine.mst.edu/doctoral_dissertations/2253
[63] P. Auguste, A. Mauduit, L. Fouquet, and S. Pillot, "Study on 17-4 PH stainless steel produced by selective laser melting," *UPB Scientific Bulletin, Series B: Chemistry and Materials Science*, vol. 80, no. 4, pp. 197–210, 2018.
[64] G. Aydin, M. A. Valiente Bermejo, M. Högström, A. Şelte, C. Oikonomou, and J. Andersson, "Influence of laser metal deposition process parameters on a precipitation hardening stainless steel," *Welding in the World*, Jan. 2023, doi: 10.1007/s40194-023-01478-7.
[65] O. F. Murathan and M. R. Abul, "□Heat Treatment and Surface."
[66] ASM International, "Heat Treating," in *ASM Handbook*, p. 2173.
[67] A. Mauduit, P. Auguste, L. Fouquet, and S. Pillot, "Study on 17-4 PH stainless steel produced by selective laser melting," *Bull., Series B*, vol. 80, 2018, [Online]. Available: https://www.researchgate.net/publication/329586854
[68] C. N. Hsiao, C. S. Chiou, and J. R. Yang, "Aging reactions in a 17-4 PH stainless steel," *Mater Chem Phys*, vol. 74, no. 2, pp. 134–142, 2002, doi: https://doi.org/10.1016/S0254-0584(01)00460-6.
[69] W. do Yoo, J. H. Lee, K. T. Youn, and Y. M. Rhyim, "Study on the microstructure and mechanical properties of 17-4 PH stainless steel depending on heat treatment and aging time," *Solid State Phenomena*, vol. 118, pp. 15–20, 2006, doi: 10.4028/www.scientific.net/SSP.118.15.
[70] H. R. Lashgari, C. Kong, E. Adabifiroozjaei, and S. Li, "Microstructure, post thermal treatment response, and tribological properties of 3D printed 17-4 PH stainless steel," *Wear*, vol. 456–457, Sep. 2020, doi: 10.1016/j.wear.2020.203367.
[71] S. A. Jose, M. John, and P. L. Menezes, "Cermet Systems: Synthesis, Properties, and Applications," *Ceramics*, vol. 5, no. 2. MDPI, Jun. 01, 2022. doi: 10.3390/ceramics5020018.
[72] A. Aramian, S. M. J. Razavi, Z. Sadeghian, and F. Berto, "A review of additive manufacturing of cermets," *Addit Manuf*, vol. 33, May 2020, doi: 10.1016/j.addma.2020.101130.
[73] Y. Yang, C. Zhang, D. Wang, L. Nie, D. Wellmann, and Y. Tian, "Additive manufacturing of WC-Co hardmetals: a review," *International Journal of Advanced*

Manufacturing Technology, vol. 108, no. 5–6, pp. 1653–1673, May 2020, doi: 10.1007/s00170-020-05389-5.
[74] A. Fortunato, G. Valli, E. Liverani, and A. Ascari, "Additive Manufacturing of WC-Co Cutting Tools for Gear Production," *Lasers in Manufacturing and Materials Processing*, vol. 6, no. 3, pp. 247–262, Sep. 2019, doi: 10.1007/s40516-019-00092-0.
[75] A. Joseph, "Additive Manufacturing of novel cemented carbides with self lubrificating properties," 2019.
[76] C. Liu, "Alternative binder phases for WC cemented carbides."
[77] A. S. Kurlov and A. I. Gusev, "Tungsten carbides and W-C phase diagram," *Inorganic Materials*, vol. 42, no. 2, pp. 121–127, Jan. 2006, doi: 10.1134/S0020168506020051.
[78] A. Yousfi, "Microstructure Development of WC-Co Based Cemented Carbides During Creep Testing," 2016.
[79] V. Sarin, D. Mari, and L. Llanes, Eds., *Comprehensive hard materials*, First., vol. 1–3. Waltham: Elsevier, 2014.
[80] M. Hu, J. cheng Tang, X. gui Chen, N. Ye, X. yue Zhao, and M. miao Xu, "Microstructure and properties of WC-12Co composite coatings prepared by laser cladding," *Transactions of Nonferrous Metals Society of China (English Edition)*, vol. 30, no. 4, pp. 1017–1030, Apr. 2020, doi: 10.1016/S1003-6326(20)65273-6.
[81] S. Fries *et al.*, "Laser-Based Additive Manufacturing of WC–Co with High-Temperature Powder Bed Preheating," *Steel Res Int*, vol. 91, no. 3, Mar. 2020, doi: 10.1002/srin.201900511.
[82] K. W. Kim, G. S. Ham, S. H. Park, J. W. Cho, and K. A. Lee, "Direct energy deposition of ultrastrong WC-12Co cemented carbide: Fabrication, microstructure and compressive properties," *Int J Refract Metals Hard Mater*, vol. 99, Sep. 2021, doi: 10.1016/j.ijrmhm.2021.105591.
[83] H. Jia, H. Sun, H. Wang, Y. Wu, and H. Wang, "Scanning strategy in selective laser melting (SLM): a review," *International Journal of Advanced Manufacturing Technology*, vol. 113, no. 9–10. Springer Science and Business Media Deutschland GmbH, pp. 2413–2435, Apr. 01, 2021. doi: 10.1007/s00170-021-06810-3.
[84] T. J. Jeon, T. W. Hwang, H. J. Yun, C. J. VanTyne, and Y. H. Moon, "Control of porosity in parts produced by a direct laser melting process," *Applied Sciences (Switzerland)*, vol. 8, no. 12, Dec. 2018, doi: 10.3390/app8122573.
[85] W.-W. Liu *et al.*, "Review on scanning pattern evaluation in laser-based additive manufacturing," *Optical Engineering*, vol. 60, no. 7, p. 18, 2021, doi: 10.1117/1.
[86] K. S. B. Ribeiro, F. E. Mariani, and R. T. Coelho, "A Study of Different Deposition Strategies in Direct Energy Deposition (DED) Processes," *Procedia Manuf*, vol. 48, pp. 663–670, 2020, doi: 10.1016/j.promfg.2020.05.158.

CHAPTER 2 L-DED SINGLE-TRACK AND MULTILAYER DEPOSITIONS IN 17-4 PH: INFLUENCE OF PROCESS PARAMETERS AND POST-FABRICATION HEAT TREATMENTS

The present chapter aims at presenting the study performed on 17-4 PH single-track depositions considering the effects of different L-DED process parameters. The geometry of the transversal section of the tracks, the dilution, the fraction of porosity, and the defects were evaluated and their relationship with the process parameters was discussed. The samples identified as fabricated with the most suitable combinations of process conditions were subjected to deep microstructural and mechanical investigations. Different post-fabrication heat treatments were performed and the evolution in the microstructure as well as the improvement in mechanical properties was assessed. Finally, the microstructural and mechanical analysis carried out on multitrack depositions fabricated with the optimal process parameters is shown.

2.1 EXPERIMENTAL PROCEDURE FOR THE SINGLE-TRACK DEPOSITIONS

In this present investigation, gas atomized 17-4 PH steel powders (supplied by Il Sentiero International Campus, Magreta, Italy) were used for manufacturing three single tracks deposited on 120 x 40 x 10 mm AISI 316L stainless steel plates used as a substrate, as depicted in Figure 2.1. The powder particle granulometric analysis performed by the supplier showed a near-spherical shape with some rough agglomerates and satellites together with a few elongated particles that range in diameter from 45 - 90 μm, as shown in Figure 2.2. Their chemical composition, determined via a semiquantitative analysis employing a Zeiss EVO MA 10 (Carl Zeiss, Jena, Germany) scanning electron microscope equipped with a Bruker Quantax probe (Bruker, Massachusetts, US) is shown in Table 2.1. In Table 2.2 is collected the nominal chemical composition (wt.%) of the specific AISI 316L stainless steel used as a substrate, highlighting that its selection was due to the similarity of the chemical composition among both materials.

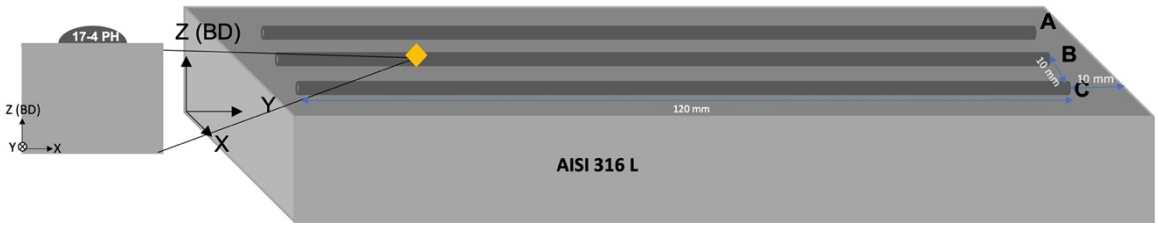

Figure 2.1 Scheme of the three-replicas 17-4 PH single-track L-DED depositions.

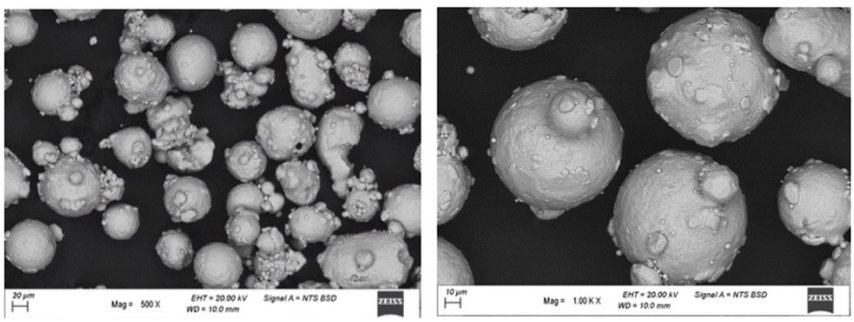

Figure 2.2 SEM micrographs of the 17-4 PH gas atomized powder analyzed by Il Sentiero International Campus.

Table 2.1 Chemical composition (wt. %) of the 17-4 PH powder employed for the L-DED depositions.

Element	C	Si	Cr	Ni	Cu	Nb	Mn	P	Fe
Chemical composition [wt. %]	0.039	0.43	15.24	4.49	3.39	0.27	0.50	0.019	Balance

Table2.2 Nominal chemical composition (wt. %) of the AISI 316L stainless steel.

Element	C	Si	Cr	Ni	Mo	Mn	P	Fe
Chemical composition [wt. %]	≤ 0.030	≤ 1	16-18	10-14	2-3	≤ 2.0	≤ 0.045	Bal.

A six-axis ABB IRB 4600 (ABB, Zurich, Switzerland) robot (see Figure 2.3), available at the Birex Competence Center (Bologna – Italy) and equipped with a coaxial nozzle with 6 heads, a laser line source of 4.5 kW and argon as a carrier and shield gas in flow rates of 3 L/min and 6 L/min, respectively, was used to manufacture the tracks. The robot was also equipped with a v2.0 CLAMIR camera (CLAMIR, Madrid, Spain), which was used to control the laser power and monitor the melt pool size during the process.

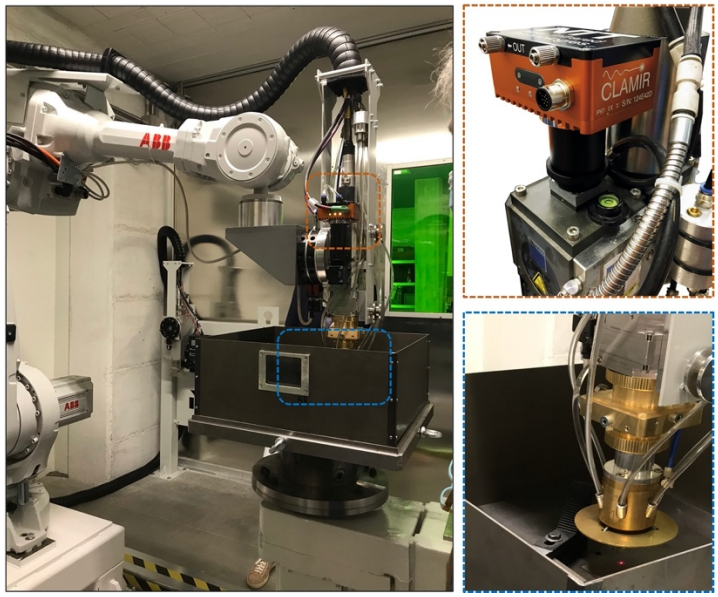

Figure 2.3 Robot used to fabricate the L-DED depositions with the CLAMIR camera illustration.

To establish the process parameters to be employed in the present investigation, a preliminary geometrical evaluation was performed. Twenty-seven different conditions were obtained (Table 2.3) from a full factorial design of experiments of three factors and three levels (3^3) including laser power (*P*) in a range of 1500 – 2500 W, scanning speed (*V*) in the range of 10 – 20 mm/s, and power feed rate (*PFR*) in a range of 6.7 – 20.1 g/min. The laser spot size (*dspot*) was maintained constant and equal to 2.2 mm.

Table 2.3 Initial process parameters employed to deposit the 17-4 PH specimens.

Power (*P*) [W]	Replicas	Scanning speed (*V*) [mm/s]	Power feed rate (*PFR*) [g/min]
1300	A B C	10	6,7
1300	A B C	10	13,4
1300	A B C	10	20,0
1300	A B C	15	6,7
1300	A B C	15	13,4
1300	A B C	15	20,0
1300	A B C	20	6,7
1300	A B C	20	13,4
1300	A B C	20	20,0
1730	A B C	10	6,7
1730	A B C	10	13,4
1730	A B C	10	20,0
1730	A B C	15	6,7
1730	A B C	15	13,4
1730	A B C	15	20,0
1730	A B C	20	6,7
1730	A B C	20	13,4
1730	A B C	20	20,0
2160	A B C	10	6,7
2160	A B C	10	13,4
2160	A B C	10	20,0
2160	A B C	15	6,7
2160	A B C	15	13,4
2160	A B C	15	20,0
2160	A B C	20	6,7
2160	A B C	20	13,4
2160	A B C	20	20,0

All eighty-one specimens (considering the three replicas named A, B, C) were geometrical and visually studied after their metallographic preparation following the steps specified in Table 2.4. It is worth mentioning that seventeen different combinations of etchants and etching times (see Table 2.5) were investigated in order to optimize the microstructure of the 17-4 PH alloy; in fact, the different chemical etchants suggested in the literature [1]–[5] were not found satisfactory in revealing the microstructure. The 17-4 PH deposited material and the substrate were etched individually.

Table 2.4 Metallographic preparation followed for the 17-4 PH depositions.

	Metallographic Preparation
Grinding	80, 120, 220, 400, 600, 800, 1000, 1200 and 2500 SiC papers, lubricated with water
Polishing	I. 6, 3 and 1 μm diamond paste using lubricant for diamond II. Al_2O_3 0.03 μm using water and delicate soap as lubricant
Etching	Kalling's (2g $CuCl_2$, 40 mℓ HCl in 40-80 mℓ ethanol) for 10 sec for 17-4 PH Oxalic acid for 240 sec and 6 V for the AISI 316 L SS

Table 2.5 Investigated combinations of etching strategies.

Etchant	Time and Voltage
Vilella's	15 s
Vilella's	30 s
Fry's	3 s
Fry's	5 s
Kalling's	2 s
Kalling's	5 s
Beraha's	25 s
Oxalic Acid	240 s, 6 V
Oxalic Acid + Beraha's	300 s, 6 V + 60 s
Kalling's	10 s
Fry's	5 s
Vilella's	90 s
Fry's + Marble's	5 s + 15 s
Ralph's	45 s
Ralph's + Oxalic Acid	20 s + 120 s, 6 V
Marble's	10 s
Ralph's + Oxalic Acid+ Kalling's	20 s + 120 s, 6 V + 5 s

After the metallographic preparation of these preliminary samples, geometrical dilution (D%) was determined in each sample, following the scheme highlighted in Figure 1.6 and using Equation 1.3 [6]. Moreover, features such as the height of the clad, the percentage of porosity, and defects were measured in each specimen. In accordance with some authors [7]–[11], dilution is strongly dependent on the process parameters According to several authors, to guarantee adequate bonding and adhesion between the deposited material and the substrate the dilution should be between 10 % and 30 % [8], [12], [13].

The eighty-one samples were evaluated according to specific acceptance criteria: a good dilution in the range 10% - 30 %, a specific size of porosity (high, medium, and low), no defects such as detachments and cracks, and the height of the clad within 400 μm. Then, a ranking from 1 to 7 was established for each of the mentioned criteria, assigning a score equal to 1 if the sample respected all the criteria, up to 7 if the sample respected no one.

Considering the scores obtained in this preliminary analysis, four sets of process conditions were selected in order to perform a deep investigation. For each selected combination, three 100 mm long single-track replicas (named A, B, and C) were deposited on the same substrate. As can be observed in Figure 2.4, a 10 mm distance was maintained among them and from the substrate corners to avoid edge effects.

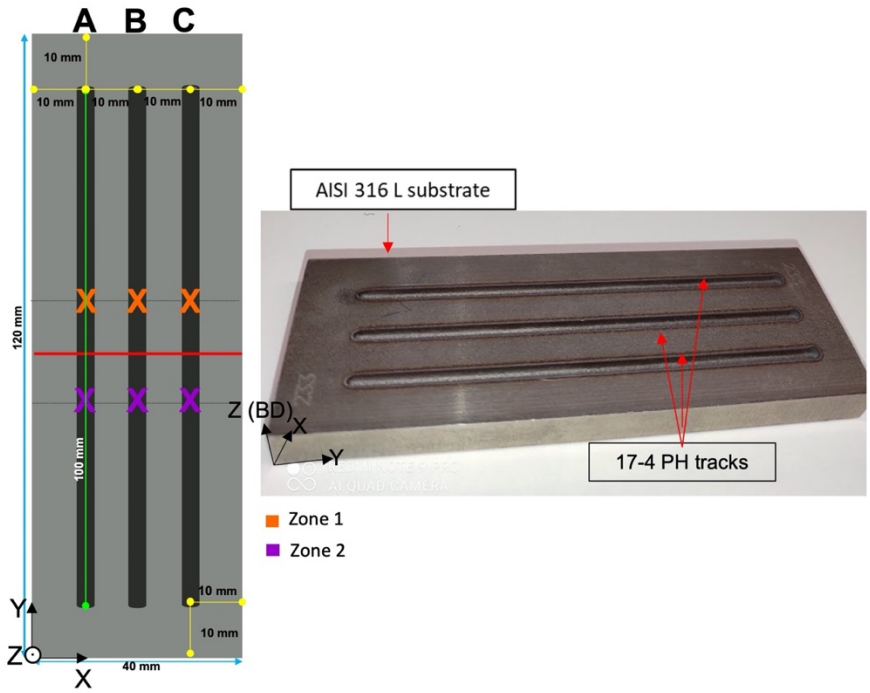

Figure 2.4 Example of single-track L-DED depositions: sampling positions along the tracks are highlighted.

From every single track, two specimens were drawn symmetrically concerning the half-length of the tracks (Zone 1 and Zone 2, respectively Figure 2.4). So, a total of 24 specimens were obtained (6 for each set of process parameters). This method of sampling was chosen to consider possible inhomogeneity in the microstructural features along the length of the depositions. All these specimens were prepared in accordance with the standard ASTM E3, starting with grinding by SiC papers from 120 to 2500 grit and then polishing with diamond and colloidal silica suspensions from 6 to 0.3 µm (Table 2.5). Before etching, all the specimens were preliminarily observed by a Leica MZ6 (Leica, Wetzlar, Germany) stereomicroscope to measure through the Leica Application Suite (LAS v4.13) image analysis software, the most important geometrical features of the cross-sections. The measurements were performed according to [14] as described in Figure 1.6. Dilution (D%), which is representative of the quality of the L-DED depositions was calculated again according to the Equation 1.3 [15].

Additionally, the porosity content was also investigated by using the image analysis technique and data was used to estimate the density (ρ) of the depositions. In each track's cross-section, the fraction of porosity was calculated according to the Equation 1.4 [15], and used to estimate the density of the deposition because the area of the deposited tracks was too small to apply other physical methods such as apparent Archimedes to measure its density.

Microstructural observations of the specimens were performed by the Leica DMi8A (Leica, Wetzlar, Germany) optical microscope, with the aim of deeply investigating the main microstructural features of the material according to the four selected process parameters. In addition, a detailed analysis of the chemical dilution across the interface between the substrate and the deposited track, as well as of the microstructural features, was carried out by a Zeiss EVO MA 15 (Carl Zeiss, Jena, Germany) scanning electron microscope equipped with an Oxford Xmax 50 (Oxford Instruments, Abingdon-on-Thames, UK) microprobe for energy-dispersive spectroscopy (SEM/EDS).

The phase compositions of both the AISI 316L substrate and the 17-4 PH L-DED tracks were studied by X-ray diffractometry (XRD) using a D8 Bruker X-ray diffractometer (Bruker, Massachusetts, US) with Cu K-α radiation and a pattern acquired from 20° to 110°

(2θ mode, 0.02° step size, and 1 s/step) in order to confirm the presence of the before explained microstructural components.

Vickers microhardness behavior of the selected specimens was measured by performing linear profiles across the substrate and the tracks under 50 gf load (HV0.05) and 15 s loading time by a Future-Tech FM1e Vickers micro indenter (Future-Tech Corp., Kawasaki, Japan) in accordance with the UNI EN ISO 6507-1:2018 standard.

Once the selected samples were analyzed in their as-built conditions, some heat treatment routes were performed on specimens drawn from the tracks, considering specifically designed time and temperature conditions to analyze the changes in terms of microstructural evolution and hardness Table 2.6 shows in detail the different selected heat treatment routes, distinguished in *stage I, stage II and stage III*.

These three heat treatment stages were practiced in order to analyze the effect of the different time and temperature variations across the microstructural and hardness behavior. *Stage I,* which includes the H900 commonly used treatment for the 17- PH stainless steel was employed to analyze its effect across the additively manufactured as built samples and to have a starting point of the treated samples as manner of comparison in the future treatment applications. *Stage II,* HT1 was performed in order to corroborate the previous treatment employed at 60 min, however two more aging times were employed in order to analyze the effect of the full H900 treatment across the precipitation across the 17-4 PH specimens. HT2 was developed with a short solubilization and the same three aging times conditions. In this case, the shorten time applied in the step of the treatment was applied in order to analyze how the time of the solution of the elements affects the microstructural formation. HT3 instead, was performed in a direct aging treatment with no solubilization of the elements to comprehend how the microstructure behaves after in terms of the precipitation of the hardened particles. It is known that during the laser process provoked by the L-DED the material already suffers a similar treatment condition so when the heat treatment is applied with no solubilization consideration it is possible to obtain the same microstructure as the as-built samples but with hardened precipitation, which consequently increases the mechanical properties of the specimen. *Stage III* was planned in order to analyze the same treatment surgencies but with longer aging times, since as mentioned before, the effect of a long time of the aging promote the feasible formation of Cu-rich precipitates that increase a bit more the hardness behavior of the sample and reduce the ferrite formation across the martensitic matrix.

The solubilization heat treatment was performed in a tubular Lenton LTF oven while a Remet mod E-79N was used for the aging step. During the treatments a K-type thermocouple was positioned inside the equipment, and the temperature evolution was monitored and acquired by an OMEGA TC-08 data logger with Picolog 6 software. Figure 2.5 shows the system used for the heat treatment of each sample. Figure 2.6 as an example, shows the general heat treatment route followed by the sample HT1 and HT2 for *stage II* and *stage III*.

One deposition for each process parameter condition was tested with the different treatment conditions and after that, the microstructural analysis via optical and scanning electron microscope with a further microhardness profile was performed.

Table 2.6 Heat treatment routes performed during the present 17-4 PH experimentation.

	#	Solution treatment	Quenching	Aging at 480 °C (min)
Stage I	HT1	1040 °C x 30'	In water	60
Stage II	HT1	1040 °C x 30'	In water	60 180 300
	HT2	1040 °C (short)	In water	60 180 300
	HT3	NO	NO	60 180 300
Stage III	HT1	1040 °C x 30'	In water	6000
	HT2	1040 °C (short)	In water	6000
	HT3	NO	NO	6000

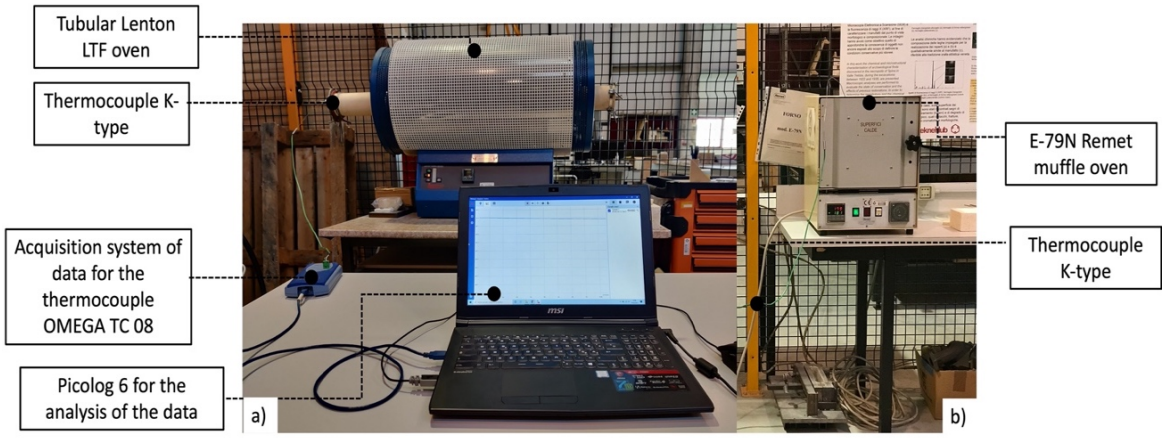

Figure 2.5 Equipment system employed during the heat treatment.

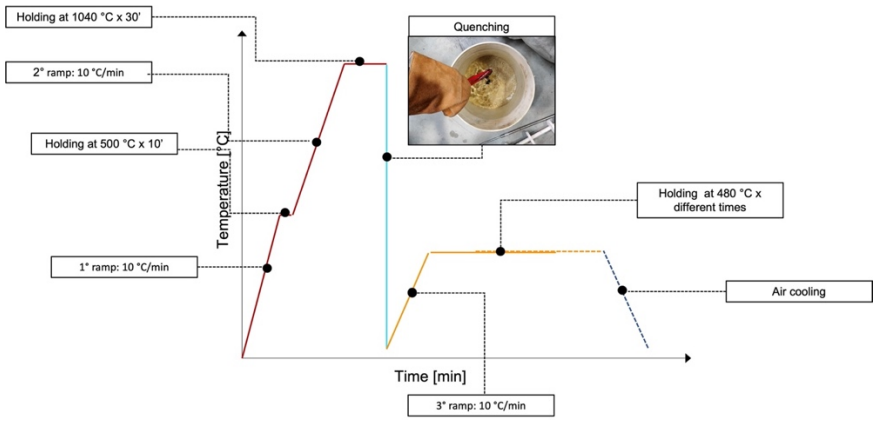

Figure 2.6 Heat treatment routes followed during the experimentation.

2.2 DISCUSSION OF THE SINGLE-TRACK DEPOSITIONS RESULTS

2.2.1 Geometrical analysis

The performed analysis across the preliminary eighty-one specimens has demonstrated that considering the reliability of this factor was useful to discriminate and

select the best conditions. However, additional analysis across the samples including the presence of defects such as detachment, the quantity of porosity, and the height of the bead was considered as well. These results analysis is depicted in Table 2.7. As observed the dilution is highly influenced by the thermal input of the laser and the quantity of the deposited material by the PFR. Although some specific samples show a higher dilution it is highlighted that they present another kind of unacceptable defect such as high porosity, detachment, or in some cases overpass the accepted range of dilution. In addition, some other conditions present a dilution value within the abovementioned D% range.

Table 2.7 Average dilution response found across each specimen at the different process parameter conditions.

Power (*p*) [W]	Replicas	Scanning speed (*V*) [mm/s]	Power feed rate (*PFR*) [g/min]	Dilution (D%) [%]	Height of the clad H [mm]	Defects presence (Sum of points in accordance with low porosity 0.5, medium porosity 1, high porosity 2 and detachment 4)
1300	A B C	10	6,7	29,2	406,0	1,5
1300	A B C	10	13,4	6,6	672,3	4,0
1300	A B C	10	20,0	2,9	883,0	7,0
1300	A B C	15	6,7	44,2	259,3	1.0
1300	A B C	15	13,4	14,2	447,7	1.0
1130	A B C	15	20,0	1,3	612,3	7,5
1300	A B C	20	6,7	51,7	194,7	0
1300	A B C	20	13,4	19,5	344,7	2,0
1300	A B C	20	20,0	31,8	302,3	3,0
1730	A B C	10	6,7	39,4	403,0	2,5
1730	A B C	10	13,4	8,0	749,0	5,0
1730	A B C	10	20,0	1,8	1063,3	7,5
1730	A B C	15	6,7	48,4	290,3	2,5
1730	A B C	15	13,4	16,2	518,7	2,0
1730	A B C	15	20,0	4,2	705,3	7,5
1730	A B C	20	6,7	52,6	236,3	1,5
1730	A B C	20	13,4	26,9	377,3	2,5
1730	A B C	20	20,0	13,0	473,7	3,0
2160	A B C	10	6,7	31,2	371,0	1,0
2160	A B C	10	13,4	29,5	666,3	5,0
2160	A B C	10	20,0	5,4	925,0	7,0
2160	A B C	15	6,7	63,2	274,7	0
2160	A B C	15	13,4	40,3	424,7	1,0
2160	A B C	15	20,0	20,3	575,7	3,0
2160	A B C	20	6,7	57,9	256,7	0
2160	A B C	20	13,4	33,4	409,0	2,0
2160	A B C	20	20,0	11,1	556,0	3,5

Therefore, only four sets of parameters were selected, since apart from their dilution value, were selected due to their low quantitative level of porosity and no detachment of the deposited track. Table 2.8 shows the chosen conditions able to guarantee a good bonding in accordance with the dilution range, the higher height of the clad together to the best evaluation in accordance with all the other evaluations observed in the last column of Table 2.7.

Table 2.8 Process conditions selected from the dilution (D%) analysis.

Set	Power (*p*) [W]	Scanning speed (*V*) [mm/s]	Power feed rate (*PFR*) [g/min]	Laser energy input (*E*) [J/mm^2]	Dilution (*D%*) [%]
S1	1300	15	13,4	39.4	14.1
S2	1730	15	13,4	52.4	16.2
S3	1730	20	20,0	39.3	13.0
S4	2160	20	20,0	49.1	11.1

As observed in Table 2.7 the laser energy density (*E*) factor, described by Equation 1.1 was also calculated. In accordance with many authors [8], [16]–[19] the relevance of this factor is of high relevance to control the porosity and defect presence since expresses the effect of the combination of the primary process parameters on the microstructural and mechanical behavior of the specimens.

Results of Table 2.8 reflect that the energy density value is highly influenced by the laser power since this parameter increases as higher is the power. This is surely true in the case of S1 and S2 in which the scanning speed was fixed as constant.

In S2 and S3 it is observed that is necessary to maintain a lower scanning speed to obtain a high dilution. This effect is contradicted when samples S3 and S4 were analyzed because when both the scanning strategy and laser power were employed, the higher dilution of the powder across the substrate.

2.2.2 Macrostructural analysis and porosity measurements

The four selected samples were cross-sectioned in two zones (zone 1, zone 2) of each track (A, B, C), as demonstrated in Figure 2.5, so a total of 6 specimens of each parameter combination were considered to test the homogeneity of the microstructure along the depositions. After a metallographic preparation as mentioned in Table 2.4, the measured features of each clad are summarized in Table 2.9.

In addition, Table 2.9 collects as well some more results related to the measurements performed on the cross sections of the samples by image analysis. In particular, the porosity percent [Ap %] which is another important feature to consider since estimates the probability of the porosity content across the clad [33], [34]. Calculated Equation 1.4 [15] it was used to estimate the density (ρ) of the deposited 17-4 PH material according to the different sets of parameters.

Data obtained from the image analysis of each specimen is compared with the full-density value for the 17-4 PH stainless steel assumed to be equal to 7.68 g/cm^3 [28], [29]. Set S4 as an example shows an average calculated value of Ap % equal to 0.881 % and thereby an estimated density ρ equal to 7.612 g/cm^3. Figure 2.7 displays the representative unetched micrographs of track A, acquired from both Zone 1 and Zone 2 of the analyzed cross-sections. It is depicted that first; the size of the pore increases as the length area of the track advance. Zone 2 presents a higher pore size than zone 1, which represent that the formation of discontinuity varies across the single deposition and consequently that this size effect is not due to the process parameter but is of the shielding protection during the process or features of the powder, just as mentioned in [12], [16], [17], [20].

Table 2.9 Geometrical features measured of each section obtained from the 17-4 PH depositions.

Sample	H [mm]	h [mm]	w [mm]	b [mm]	Ac [mm²]	Am [mm²]	Ac+ Am [mm²]	Ap [mm²]	Ap% = Ap/(Am+Ac) *100 [%]
S1_A_1	0.704	0.594	2.927	0.110	1.200	0.202	1.402	0.007	0.472
S1_B_1	0.654	0.573	2.912	0.081	1.139	0.204	1.343	0.004	0.302
S1_C_1	0.699	0.590	2.867	0.109	1.179	0.201	1.380	0.008	0.596
S1_A_2	0.639	0.578	2.819	0.061	1.153	0.157	1.310	0.005	0.356
S1_B_2	0.669	0.582	2.937	0.087	1.185	0.164	1.349	0.007	0.537
S1_C_2	0.761	0.652	2.839	0.109	1.314	0.238	1.552	0.008	0.501
mean value	0.688 ± 0.044	0.595 ± 0.029	2.884 ± 0.049	0.093 ± 0.020	1.195 ± 0.062	0.194 ± 0.030	1.389 ± 0.086	0.006 ± 0.002	0.461 ± 0.111
S2_A_1	0.778	0.683	3.231	0.095	1.563	0.266	1.829	0.010	0.524
S2_B_1	0.787	0.686	3.282	0.101	1.590	0.300	1.890	0.017	0.905
S2_C_1	0.822	0.699	3.201	0.123	1.630	0.315	1.945	0.018	0.949
S2_A_2	1.026	0.937	3.029	0.089	2.168	0.089	2.257	0.013	0.592
S2_B_2	0.979	0.923	3.116	0.056	2.108	0.060	2.168	0.019	0.879
S2_C_2	1.018	0.954	3.204	0.064	2.250	0.078	2.328	0.026	1.110
mean value	0.902 ± 0.062	0.814 ± 0.018	3.177 ± 0.090	0.088 ± 0.025	1.885 ± 0.322	0.185 ± 0.121	2.070 ± 0.208	0.017 ± 0.006	0.827 ± 0.224
S3_A_1	0.713	0.641	2.959	0.072	1.350	0.170	1.520	0.005	0.340
S3_B_1	0.765	0.662	3.003	0.103	1.428	0.137	1.565	0.005	0.342
S3_C_1	0.754	0.655	3.041	0.099	1.410	0.173	1.583	0.010	0.659
S3_A_2	0.722	0.629	3.022	0.093	1.362	0.188	1.550	0.012	0.774
S3_B_2	0.744	0.645	3.010	0.099	1.362	0.188	1.550	0.001	0.041
S3_C_2	0.802	0.658	3.005	0.144	1.385	0.207	1.592	0.009	0.594
mean value	0.750 ± 0.032	0.648 ± 0.012	3.007 ± 0.027	0.102 ± 0.024	1.383 ± 0.031	0.177 ± 0.024	1.560 ± 0.026	0.007 ± 0.004	0.458 ± 0.268
S4_A_1	0.843	0.713	3.253	0.130	1.659	0.287	1.946	0.017	0.890
S4_B_1	0.858	0.717	3.309	0.141	1.660	0.269	1.929	0.026	1.353
S4_C_1	0.870	0.728	3.309	0.142	1.745	0.279	2.024	0.017	0.815
S4_A_2	0.867	0.730	3.309	0.137	1.647	0.299	1.946	0.014	0.707
S4_B_2	0.875	0.734	3.298	0.141	1.732	0.233	1.965	0.012	0.606
S4_C_2	0.907	0.742	3.277	0.165	1.768	0.268	2.036	0.019	0.917
mean value	0.870 ± 0.021	0.727 ± 0.011	3.293 ± 0.023	0.143 ± 0.012	1.702 ± 0.052	0.273 ± 0.023	1.974 ± 0.045	0.017 ± 0.005	0.881 ± 0.259

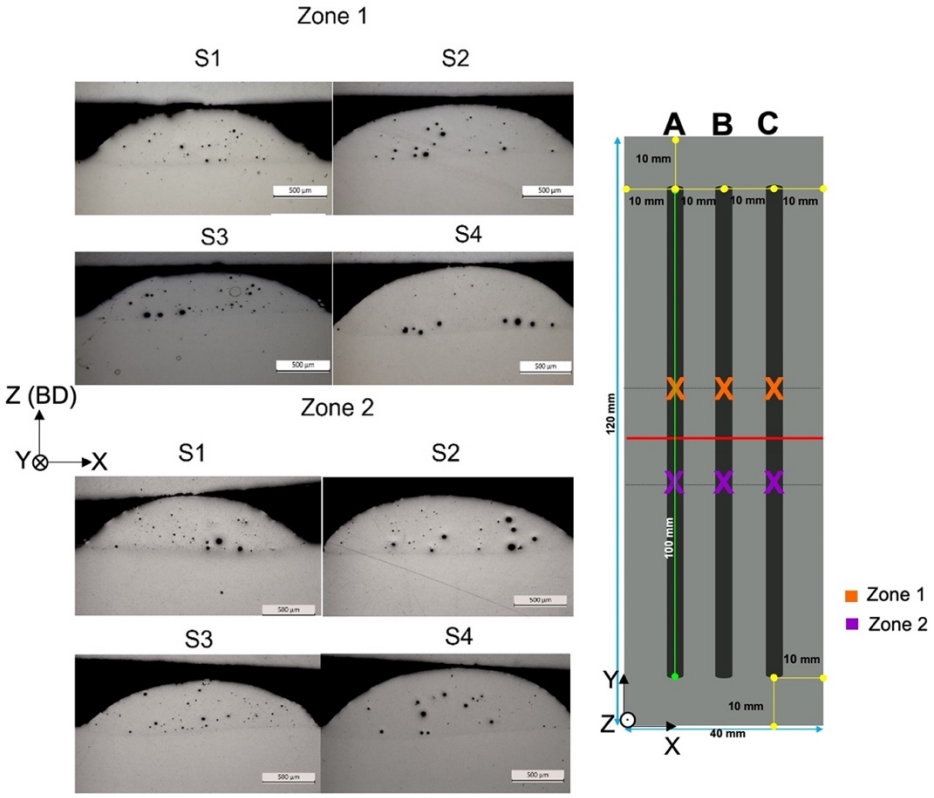

Figure 2.7 Porosity variation across the single 17-4 PH deposited tracks.

In addition, Table 2.9 reports the measured geometrical features of every single-track of the four selected samples, while Figure 2.8 depicts the average data of the same geometrical features as well as H/w and h/H ratios. Most of the highest values of the geometrical features belong to the samples drawn from the tracks performed with set S2, even though with the highest standard deviations. Even though H/w and h/H ratios, which are related to the shape of the track deposition, are higher on S2, their values seem to be strongly and directly correlated to the laser energy input (*E*) (see Figure 2.8), in particular, increasing values of specific energy generated during the process determine an increase of these geometrical features.

The tracks carried out with set S4 show the highest values of parameter b, which is important for the quality and integrity of the deposition. Comparing data from Figure 2.8a, and Figure 2.8b, the higher is b the higher the mixing zone between the substrate and the cladding material so directly correlated to dilution.

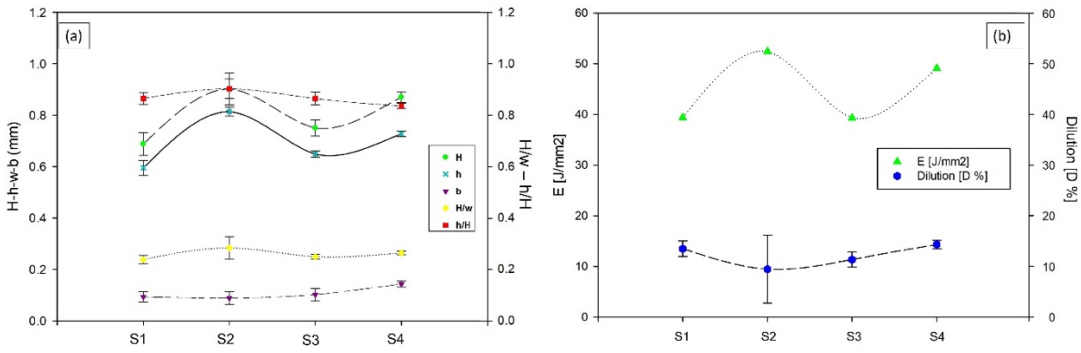

Figure 2.8 a) Geometrical features of the cross-sections and b) laser energy input (E) values against dilution [D%] for each set.

Comparing the effects of the process parameters on porosity, the study and analysis of *E* and laser power demonstrated that they have a strong impact on porosity formation. As higher the power and scanning speed employed is, as in S4, the higher the size of the pores but visually the appearance is lower. Identifying that the pores are more related to the gas porosity type, but decreasing in samples S3 and S1, samples that were performed with the lower energy density. A study performed by Gu et al [21] focused on the effect of *E* across the porosity resulting in a 17-4 PH SLM when the process conditions were varied. The porosity percent of the specimens was verified with the Archimedes method and image analysis. After their analysis it was found that even the laser energy is important to control the porosity formation, is not the best indicator for the porosity level. In accordance with this study and some others [19], [22] it is confirmed that in the present investigation, the porosity of the depositions does not always depend on the process parameters since other factors such as the powder features, gas protection, or convections interactions [23] can influence their formation and propagations.

Figure 2.9 demonstrate a more specific microstructural analysis of some of the samples where other type of defects are identified across the deposited tracks. As observed in previous section almost all the samples present gas porosity in different quantities in accordance with the process parameters used as well as some detachment at the beginning of the deposition. In accordance with the literature [20], this kind of defect could be related to the process parameters reflected in the laser energy density. Specifically, gas porosity could be formed due to the high energy density and in the case of the lack of fusion due to the excessive powder flow rate that produces insufficient melting of the powder.

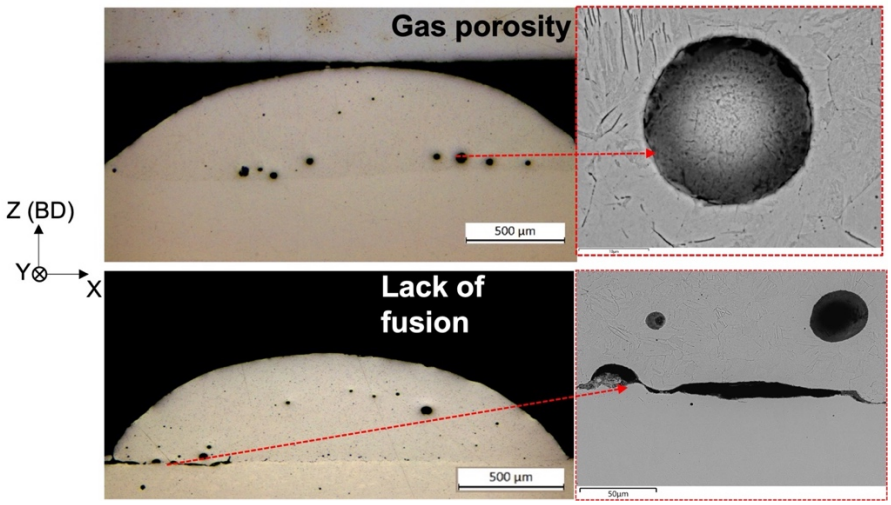

Figure 2.9 Examples of defects across the additively deposited samples.

From the geometrical and macro analysis, it was drawn up that the samples named S1 and S4 were considered as the most feasible as summarized in Figure 2.10. Both showed the presence of pores in their tracks but are smaller than the rest of the deposited samples, as observed in Figure 2.7. As can be observed, D% of S1 is higher than S4; however, the porosity presence across sample S1 is higher in quantity and consequently more dangerous for the performance of a future part while sample S4 is dispersed and less present in matter of size and distribution so this set of samples is considered as the most feasible from the porosity and geometrical point of view.

Sample	Dilution [%]	Molten area [mm^2]	%Porosity
S1	14.1	0.194	0.461
S4	11.1	0.273	0.881

Note: Data considered from the average values

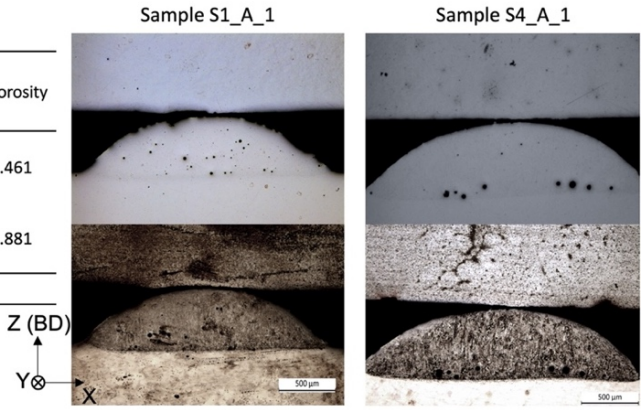

Figure 2.10 Summarizing the two most feasible deposited tracks in accordance with %D and %porosity.

2.2.3 Microstructural analysis

Prior to microstructural investigations, seventeen different combinations of etching strategies were tested to determine the best etching conditions for revealing the microstructure of the depositions; in Figure 2.11 only the twelve of them that promoted remarkable results are shown. The best was obtained with the chemical etching performed by Kalling's solution for 14 s (see Figure 2.11l). Conversely, the typical austenitic microstructure of the AISI 316L substrate was properly revealed by electrolytic etching performed in a 10 % oxalic acid solution at 6 V for 24 s, as observed in Figure 2.12.

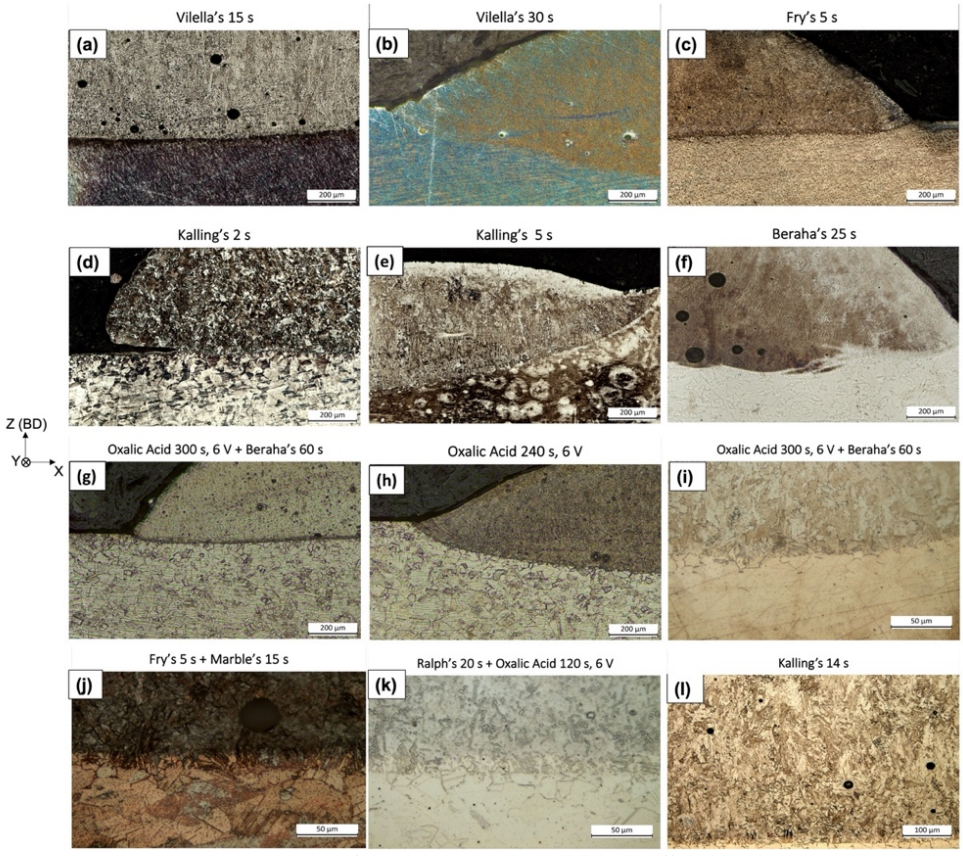

Figure 2.11 Microstructures of the deposition revealed with different etching strategies.

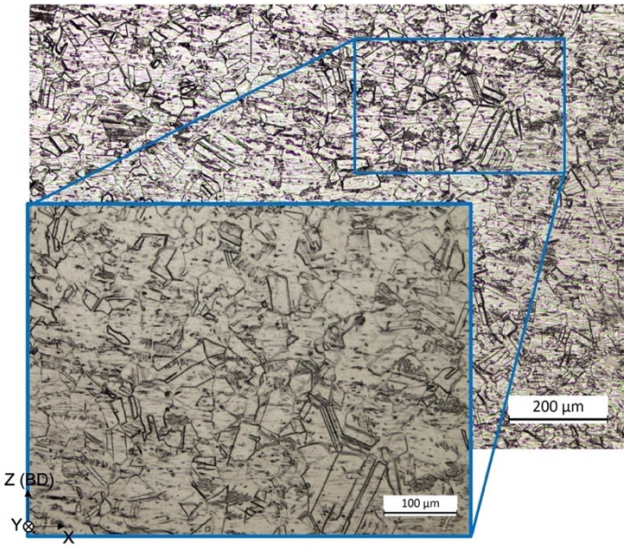

Figure 2.12 Microstructure of the AISI 316L substrate electrolytically etched in 10 % oxalic acid solution for 240 s and 6 V.

In L-DED the cooling rate is usually much higher than in traditional processes [24] usually above the melting temperature of the metal powders due to the high energy density input effect of the laser during the part production producing a rapid solidification of the molten material [25]. The microstructure generated during solidification and the control of the possible phase transformations occurring during cooling is strongly dependent on the employed process parameters and it is correlated to the thermal gradient G [K/mm] and the solidification speed R [mm/s]. In the DED deposition of tracks on a substrate, the highest cooling and solidification rates are found across the substrate/track interface, gradually decreasing as the distance from the substrate increases. Hence, in 17-4 PH single-track depositions, the high GxR values at the interface are expected to generate a fine martensitic matrix but also a high amount of retained δ-ferrite, just as stated by [26], [27].

The solidified microstructure of the present L-DED 17-4 PH samples is mainly conformed by the FCC austenite and BCC phases, which could be either ferrite or martensite. Nevertheless, the extremely rapid cooling rate experienced by the material during the process is one of the most influential factors affecting the microstructural evolution. Following the theorem mentioned in 1.2.1.1, Equation 1.5 and Equation 1.6 were respectively used to calculate Cr_{eq} and Ni_{eq} as well as their location across the Schaeffler diagram (see Figure 2.13). Moreover, the Cr_{eq}/Ni_{eq} ratio was calculated to identify the expected solidification mode of these samples.

$$Cr_{eq} = \%Cr + \%Mo + 1.5\%Si + 0.5\%Nb$$
$$Cr_{eq} = 15.24 + 0.13 + 1.5(0.43) + 0.5(0.27)$$
$$Cr_{eq} = 16.15\%$$

$$Ni_{eq} = \%Ni + 30\%C + 0.5\%Mn + 30\%N$$
$$Ni_{eq} = 4.49 + 30(0.039) + 0.5(0.50) + 30(0)$$
$$Ni_{eq} = 5.91\%$$

$$Cr_{eq}/Ni_{eq} = 2.73$$

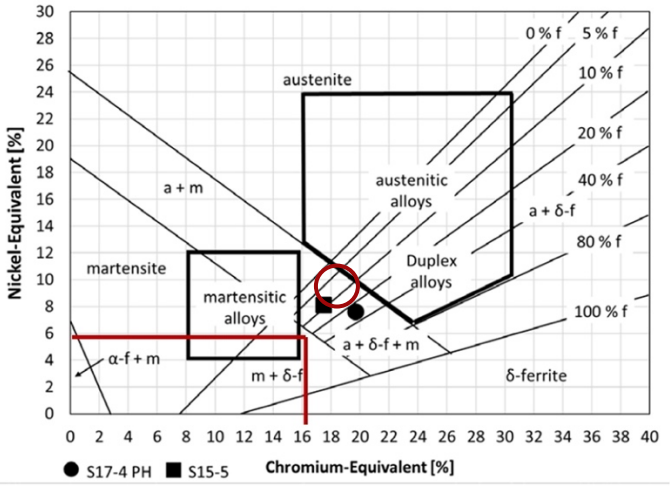

Solidification Kinetic mode	Ratio Creq/Nieq
A- full austenitic	Creq/Nieq < 1.25
AF- Austenitic- Ferritic	1.25<Creq/Nieq<1.48
FA - Ferritic- Austenitic	1.48<Creq/Nieq<1.95
F-Ferritic	Creq/Nieq>1.95

Figure 2.13 Solidification prediction of the phases presented in 17-4 PH steel performed from the Cr/Nieq calculation [28], [29].

Conventionally, solid-state transformation for 17-4 PH begins with δ-ferrite, followed by austenite, and finally, martensite formation. Considered the Schaeffler diagram reported in Figure 2.13 and the calculated Cr_{eq}/Ni_{eq} ratio, the value has demonstrated that the solidification mode of the present samples starts from the δ-ferrite with speculate austenite, δ-ferrite, and martensite microstructure presence. However, as the cooling rate is so high, the ferrite phase converts directly to martensite without transforming to austenite, remaining dominant the δ-ferrite as mentioned by [30].

Each of the specimens selected in Table 2.8 was analyzed via the Leica Dmi8A optical microscope, after its respective chemical etching with Kalling's reagent for 14 s. The representative micrographs of three different zones from the interface between the clad and the substrate up to the top of the clad itself are depicted in Figure 2.14.

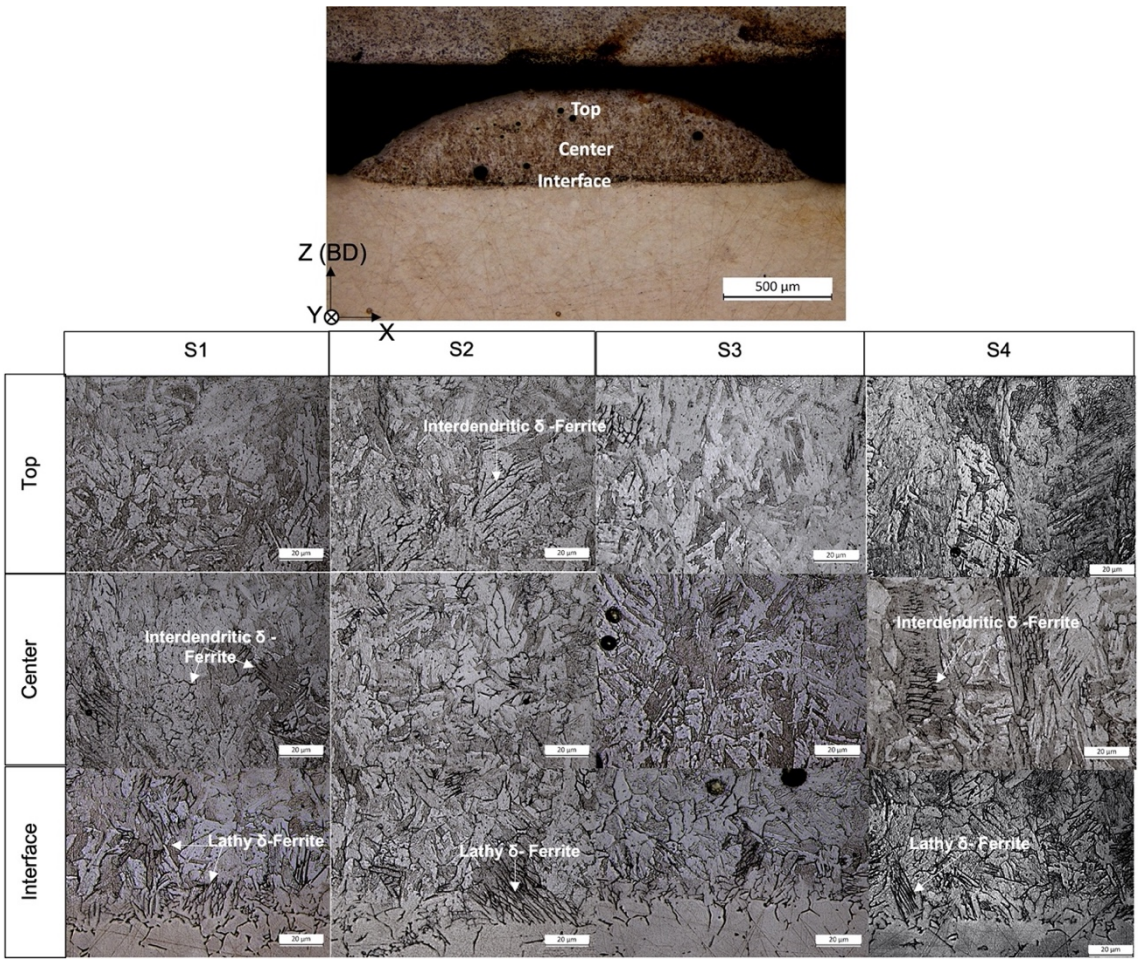

Figure 2.14 Microstructural evolution of the 17-4 PH deposited parts.

Considering Figure 2.14 the most important microstructural differences among the deposited tracks according to the investigated process parameters are mainly ascribed to the size and distribution of laths in the martensitic matrix, as well as the δ-ferrite phase, whose amount decreases from the interface to the top of the clad according, being present as well as some islands of intergranular ferrite across the martensite matrix across the length of the deposition. These experimental findings are directly related to the heat gradient evolution, i.e., the cooling rate experienced by the cladding material during the solidification. The cooling rates are directly related to the laser energy input generated according to the imposed set of parameters. Set S1 and set S2 are characterized, respectively, by the highest and the lowest laser energy inputs, so it is reasonable that the lowest the cooling rate experienced by the metal near the interface, the lower is thereby the amount of δ-ferrite.

These results are consistent with the ones of other authors, who confirmed that an increase in the size and distribution of the dendritic martensite occurs when the cooling rate is faster. Moreover, the higher cooling rate at the interface inhibits the complete transformation of the δ-ferrite prior to austenite and then to martensite [27], [31].

When a correlation of the process parameters effect across the microstructural evolution is performed it is observed that the quantity of δ-ferrite across the interface seems to be roughly similar. With the increase of laser power and scanning speed from set S1 to set S4 an increasingly less defined dendritic morphology of the martensitic matrix can be observed. Across samples S1, S2, and S3 it is depicted that the martensite laths have grown in a dendritic grain structure with a combination of small and big grains. While across the interface it is observed δ-ferrite with bigger islands in sample S2 and some interdendritic presence across the diverse zones in S3 and S1.

Sample S4 shows instead longer martensite laths of columnar dendritic structure that grew parallel in the direction of the heat flow, from bottom to top with some δ-ferrite across the interface zone. The effect of the process parameters has caused more homogeneity and evidence when the laser power and energy density are higher.

Through SEM analysis, the different zones of the specimens were deeply analyzed and by EDS microprobe the chemical dilution analysis across the interface was measured to observe the change in composition across the interface of both materials.

As observed in Figure 2.15, the lathy δ-ferrite across the different zones changes in size and distribution, being most concentrated in the shape of islands across the interface between the substrate and the deposition and being higher in sample S4. It is also observed how the columnar martensitic grains follow the cooling effect that comes from the interface to the surface of the sample; besides that, the intergranular δ-ferrite grows in the same direction. Moreover, the δ-ferrite across the interface is coarser and in higher quantity. Figure 2.16 depicts a high increase in comparison between the optical and scanning electron microscopy of sample S4. Conglomerate lathy δ-ferrite is mainly situated in the interface of both materials, decreasing its presence as in increasing the distance from the interlayer to the top part of the clad.

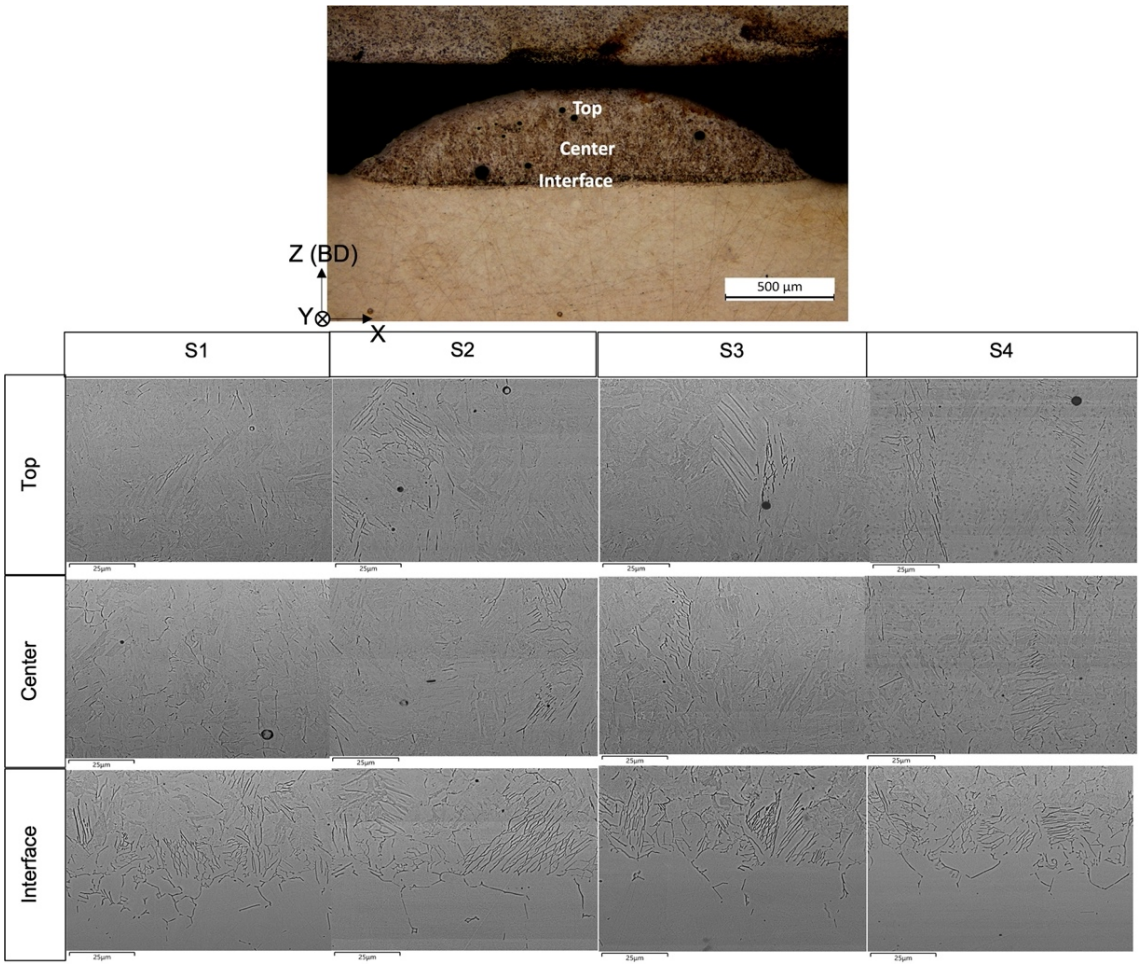

Figure 2.15 SEM micrographs showing the microstructure evolution across each DED deposition.

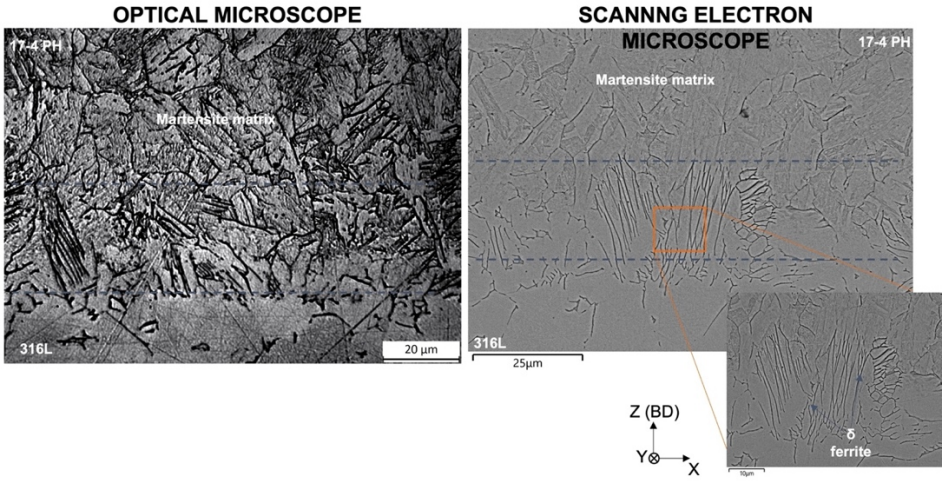

Figure 2.16 Interface micrographs comparison of one of the S4 samples that depicts the δ-ferrite.

Even though the δ-ferrite has the same crystallographic structure as BCC martensite can be recognized visually as the lathy needles presented across the martensitic matrix mentioned before. A semiquantitative image analysis across different SEM micrographs acquired at the clad/substrate interfaces were measured to know the amount of ferrite at the interface according to the different sets of parameters. From the results depicted in the binary SEM images of Figure 2.17 together with a quantitative assessment of *δ*-ferrite amount as a result of the analysis of 2.5 mm^2 of area, performed by acquiring at least n. 5 micrographs in the interface zone, it drawn up that a high-quantity of δ-ferrite is present across S2 and S3 samples while in S1 and S4 the percentage is lower. Figure 2.17 b. demonstrates the comparative plot and the analyzed images where it is observed visually the change in ferrite quantity.

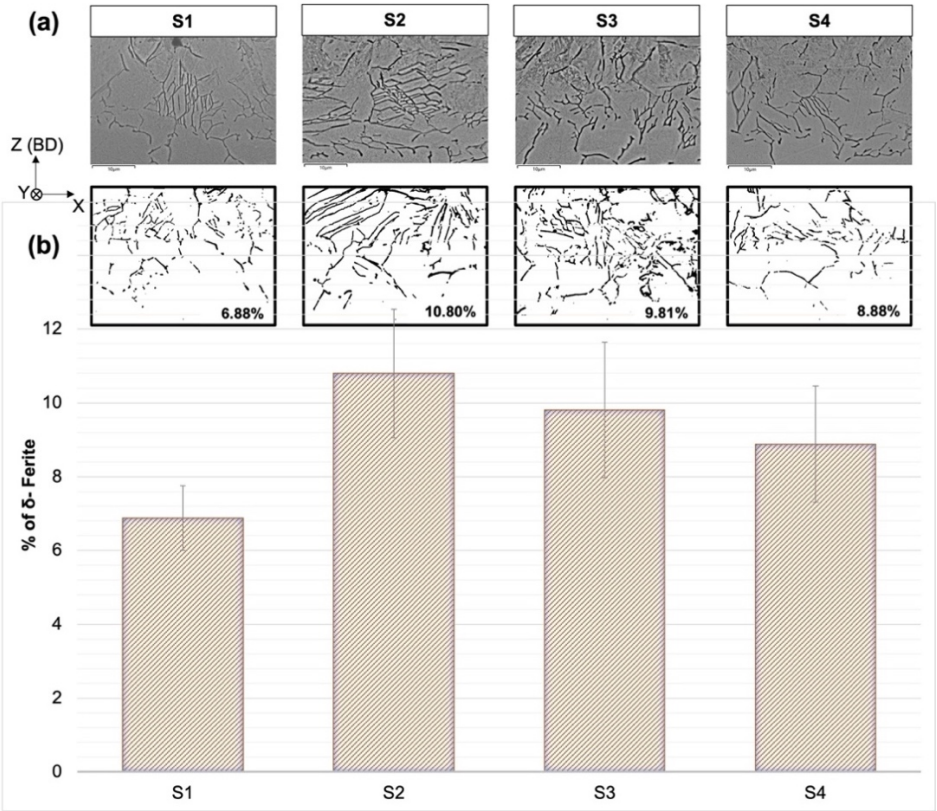

Figure 2.17 δ-ferrite percentage's plot of the samples at the different process conditions.

The δ-ferrite percentage measured across the interface was correlated with the cooling rate experienced during the process at the different process parameters. First, it is observed that being a semi-quantitative analysis the reliability is not so high, but it was decided to be performed to have an idea of the quantity of this phase and its relationship with the principal process parameters.

As the employed laser power value increases, the enhancing of the laser energy promotes a decrease in δ-ferrite content, as observed in S4, since as mentioned before sample S2 presents a lower quantity of this phase but of a bigger size. This can be related to the fact that major heat input promotes high-quantity of the initial δ-ferrite that transforms to austenite and then to martensite, remaining a lower quantity of non-transformed δ-ferrite. Across sample S1 it is observed a minor apparent quantity of δ-ferrite with lower size, due to the time that the specimens must cool and solidify during the process is higher, but the quantity of suffered heat promotes a good conversion leaving less presence of this phase.

This behavior is not coherent when the S3 sample is analyzed, even though the energy density employed during the process is lower the analysis reports higher ferrite presence, nevertheless, as in sample S3 the size is higher than in the other samples. So, for the present analyses it could be noted that is not dependent on the energy density but more on the combination of the laser power and scanning strategy effect, since depends as well on the analyzed zone and the solidification of this phase.

From these analyses sample, S4 was chosen as the one to perform the next investigations since posses' best dilution, less porosity, and media presence of δ ferrite.

The chemical dilution of elements across the interface between the substrate and the deposition clad was studied by carrying out linear maps by the energy-dispersive spectroscopy microprobe. Figure 2.18 shows the analysis performed on sample of the set S4, with evidence of a remarkable but smoothy variation in the Cr, Mn, and Ni contents across the interface in about 25-30 μm. As expected, their contents are higher in the AISI 316L stainless steel substrate than in the clad. Conversely, as concerns the Cu content, it is higher in the 17-4 PH deposition layer than in the AISI 316L substrate. It is worth noting that the smooth variation of these elements across the interface is guaranteed by the appropriate dilution that occurred during the DED building process.

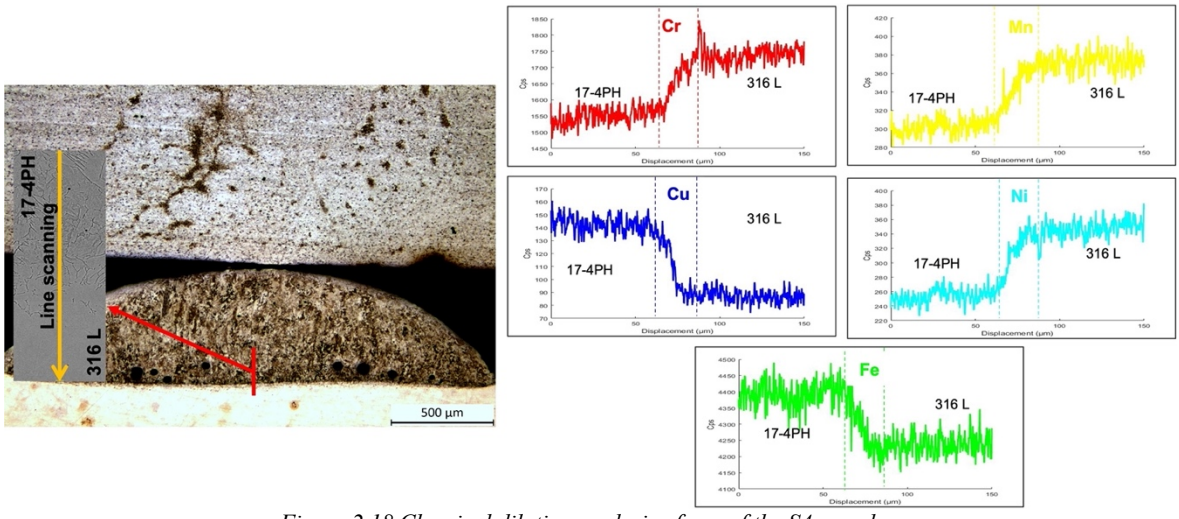

Figure 2.18 Chemical dilution analysis of one of the S4 samples.

It is worth noting that the substrate selection is of high importance to guarantee a good bonding among both materials, in the present case the AISI 316 L stainless steel owns a composition as reported in Table 2.2 which is greatly compatible with the 17-4 PH stainless steel. The microstructural analysis performed by SEM demonstrates that the AISI 316L

substrate has the typical microstructure composed of polygonal austenite grains with some twining within the grains revealed with oxalic acid, at 6 V per 240 s, as observed in Figure 2.19.

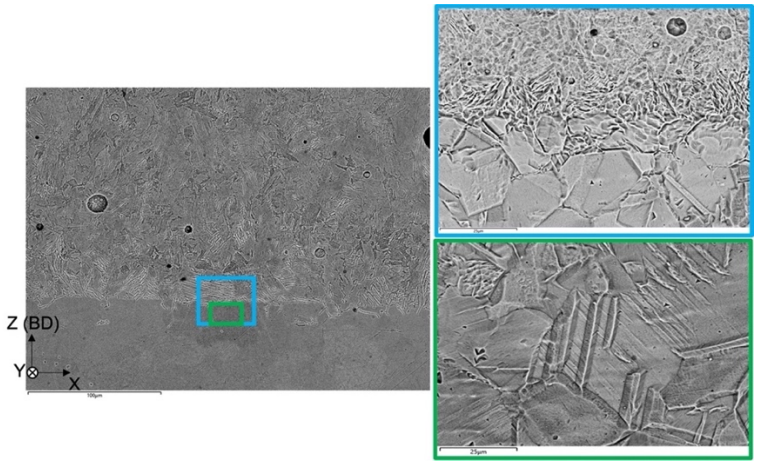

Figure 2.19 Microstructure found across the AISI 316 L stainless steel.

The X-ray diffraction patterns recorded on the surface of both the substrate and the clad are shown in Figure 2.20. In the clad, peaks related to the presence of α'-martensite (BCC) as well as peaks of γ-austenite (FCC) were identified. The presence of the latter ones can be ascribed to the small size of the clad and so to the presence of traces of austenite belonging to the AISI 316L substrate. Unfortunately, the XRD analyses have not been so useful in clearly detecting the peaks of *δ*-ferrite: due to the fast-cooling rate, the crystallographic indices of its unit cell may be confused with the ones of the α'-martensite, surely predominant in the microstructure of the clad, as mentioned in [32], [33].

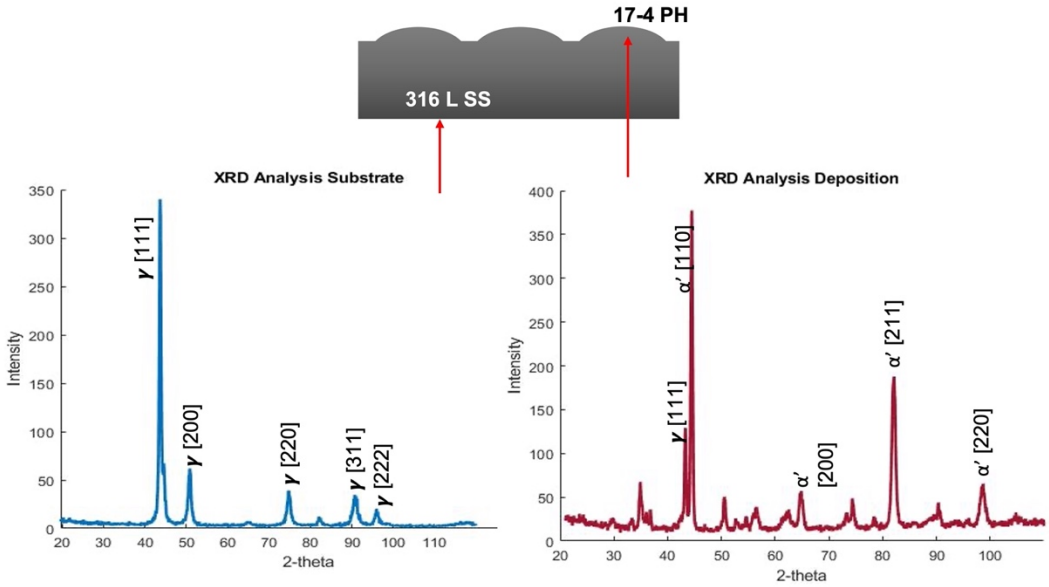

Figure 2.20 XRD patterns taken from the deposition and substrate parts of sample S4.

2.2.4 Hardness analysis

Vickers microhardness tests were performed by the linear profile analysis, from the substrate to the top of the clad across the interface, of one of the selected samples under 50 g_f load ($HV_{0.05}$) at 15 s. Table 2.10 collects the mean values of each zig-zag profile performed on each sample, and illustrated in the plot of Figure 2.21. The measured average hardness of the AISI 316L substrate is 317 ±16. HV0.05, while the average hardness values for each clad

deposited by L-DED are in the range 364 – 392 HV0.05. In the same figure, the indentation path performed across the sample is also depicted.

In accordance with the literature, it is observed that the hardness values found across the as-built L-DED depositions are like the ones performed by [34], who found out values up to 402 HV0.3, and with [30] that obtained hardness values of 334 HV0.5. The higher hardness of the deposited part is due to the martensite microstructure as well as the possible presence of Cu-based nano precipitates in the samples.

Table 2.10 Collection of hardness values measured in the different zones of the samples.

	Clad 17-4 PH		Substrate AISI 316 L	
Condition	**Mean value (HV0.05)**	**SD (HV0.05)**	**Mean value (HV0.05)**	**SD (HV0.05)**
S1	382	46,0	323	15.2
S2	389	33.8	332	17.8
S3	364	32.4	295	17.1
S4	393	46,0	323	15.2

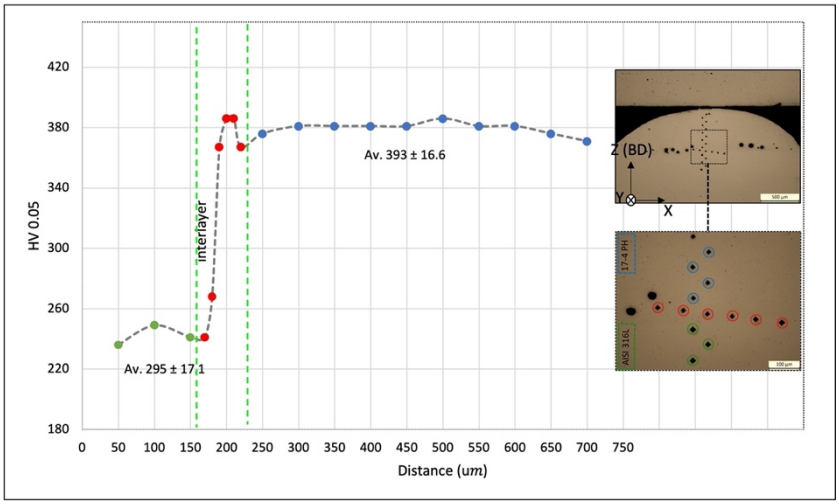

Figure 2.21 Microhardness HV0.05 profile of the one S4 sample.

2.2.5 Post-fabrication heat treatment analysis

17-4 PH steel is usually treated under the H900 condition [35] which consists of an austenitizing in a range of 1040 °C ± 10 for 30 min, quenching in water and an aging treatment at 482 °C for 1 hour in order to promote the precipitation of the coherent Cu-rich precipitates as mentioned in section 1.2.1.1 [27].

In the literature, it has been observed that the modification of the heat treatment in 17-4 PH samples obtained from different AM processes, which includes a decrease in the austenitizing time up to avoiding it [30], results in the improvement on the quantity of martensite formed, being positive for their hardness behavior.

As observed in the previous section, the attempt to find the most feasible parameters is highly important since some defects such as porosity and microcracks are still presented in the selected samples (Table 2.8). Thus, the present section highlights the results obtained after the application of different heat treatment routes, considering variations in time and temperature of both austenitizing and aging, to monitor the changes in terms of microstructure and hardness values in the 17-PH single-tracks.

Samples drawn from one single track fabricated with each of the selected process parameters were subjected to the different designed heat treatment conditions. The microstructural evolution was studied by optical and scanning electron microscopy as well as XRD analysis, while the mechanical enhances were monitored by microhardness profiles.

The samples found before as the most feasible were used to perform the tests of *stage I*. Across Figure 2.22 is depicted a comparison among the microstructures obtained from the as-built condition, after austenitizing and after the full HT1 treatment with aging of 60 min.

A change in the distribution, size, and refinement of the lath martensite can be observed across the different analyzed zones (top, center, and interlayer) of tracks. In particular, after austenitizing and quenching the microstructure is more homogeneous in comparison with the as-built one, composed of a coarse martensite and with no presence of lathy δ-ferrite, as also observed by [30]. After subsequent aging, no significative changes in the microstructure can be observed by optical microscopy because of the precipitation of nanometric precipitates. After the treatment the presence lathy δ-ferrite is no more evident with respect to the as-built condition, neither at the interface nor along the deposition up to the top, demonstrating that during the austenitizing most of the ferrite dissolve in the austenitic matrix.

This behavior is also mentioned by several author, such as [36] who performed different heat treatment routes varying the aging time and temperature and confirmed that after the conventional H900 treatment, matrix is composed by martensite with no evidence of δ-ferrite (see Figure 2.23).

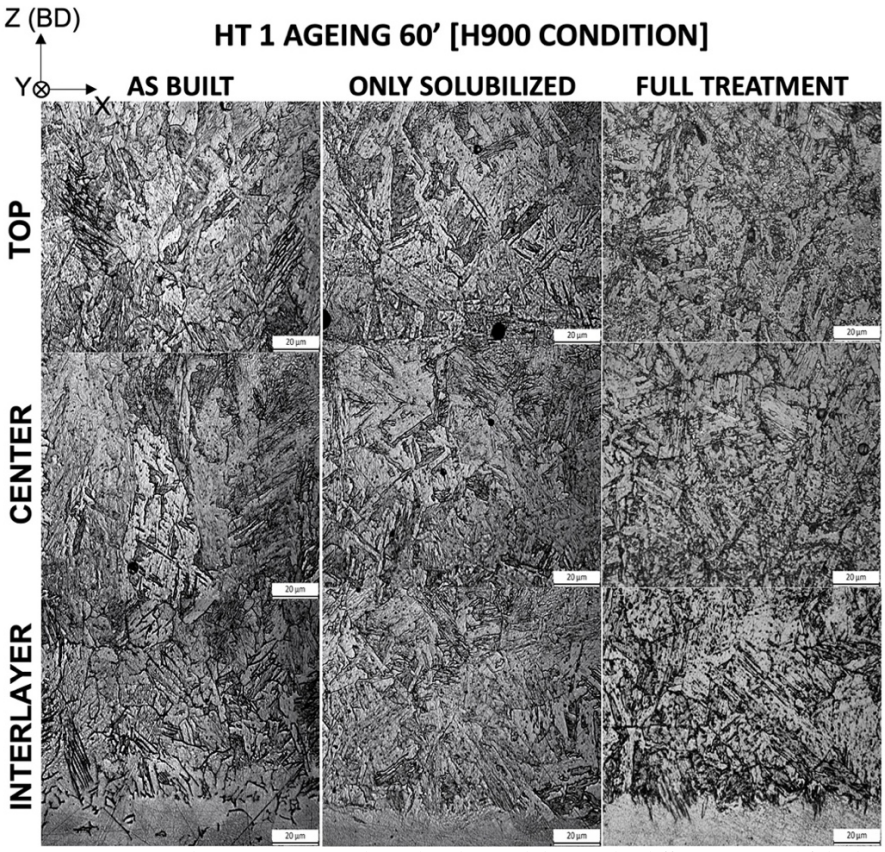

Figure 2.22 Comparison among the microstructural results obtained during the different stages of the heat treatments.

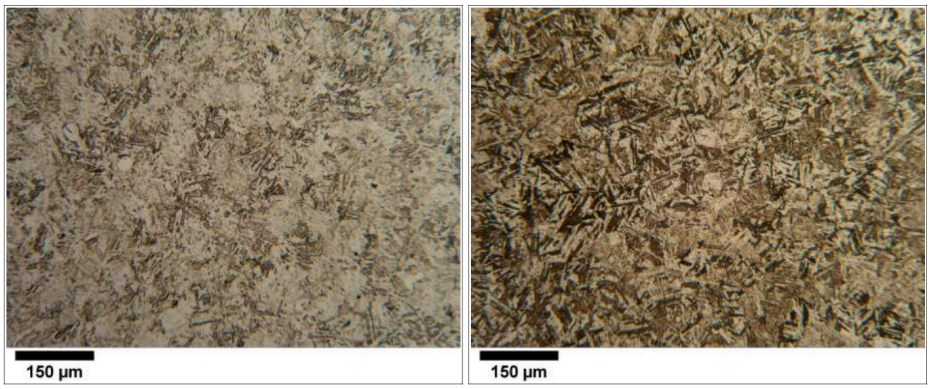

Figure 2.23 Optical micrographs obtained from [36] *right after solution treatment, left after aging at 495 °C for 4 hours.*

As shown in Figure 2.24, in all the different stages of the heat treatment HT1, XRD pattern analyses were also performed in each of the treated samples to check the nature of the phases across the depositions,

The XRD pattern of the as-built sample show four α' peaks, which correspond to the martensitic BCC phase as well as a γ[111] corresponding to the austenitic FCC phase and belonging to the substrate. The presence of the γ[111] peak is justified by to really small size of the deposited part, so in the XRD pattern also shows a high-intensity peak belonging to the substrate. Nevertheless, it was difficult to confirm the presence of δ-ferrite in the as-built condition because, as mentioned before, their peaks are usually confused with the ones of martensite. This is also confirmed by the studies performed by Moghazi [37] and Y. Sun [38].

X-ray pattern after austenitizing and quenching is very similar to the one of the as-built condition, increasing slightly in intensity due to the different saturation of the alloy after their different cooling stages in which the as-built is faster than in the solubilized condition, so the quantity of martensite is slighter lower. After the full heat treatment show differences can be observed since the intensity of the peaks are significantly lower and some other peaks were detected. We need to remember that after aging a fine precipitation of Cu-rich phases happens. Similar results were found in several other studies, such as in [38]–[41].

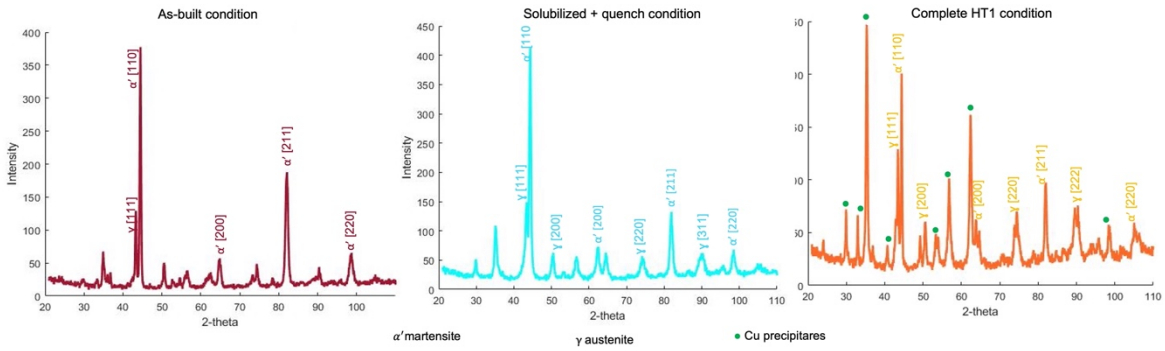

Figure 2.24 XRD patterns obtained after the different heat treatments of stage I in comparison with the as-built one.

Vickers microhardness profiles were measured across the transversal section of the selected specimen after the two different stages of the heat treatment to compare them with the as-built conditions. The results are reported in Figure 2.25. After austenitizing and quenching the hardness profile shows a significant variation in the hardness values along the deposition layer. After aging that hardness profile shows a more stable trend of results; the values of hardness along the 17 -4 PH depositions are more stable, and the hardness is higher. The increase in hardness is significantly higher than in the a-built condition 393 ± 46 HV0.05. The precipitation of Cu-rich nanoparticles surely contributes to increasing the

hardness of the layer. This behavior was also detected in other studies [38]–[40], confirming the increase in the hardness after the whole treatment. As a comparison, in Table 2.11 are collected the mean hardness values and the standard deviations.

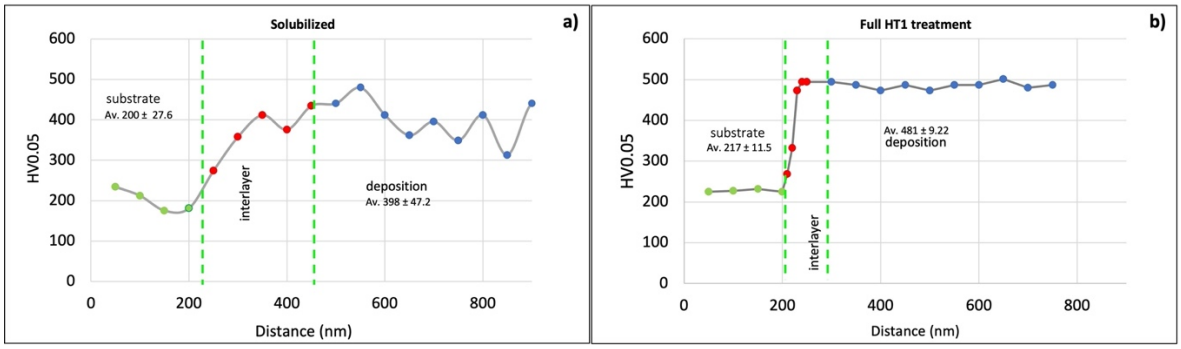

Figure 2.25 Micro Vickers hardness profiles performed after austenitizing and after the full heat treatment.

Table 2.11 Summary of the hardness values found across the different zones of the non- and heat-treated samples.

Condition	17-4 PH		Substrate AISI 316 L	
	Mean value (HV0.05)	SD (HV0.05)	Mean value (HV0.05)	SD (HV0.05)
S4 as-built	393	46	323	15.2
S4 solubilized	398	47.2	200	27.6
S4 full HT1 *stage I*	481	9.22	217	11.5

To analyze the effect of other heat treatment routes with respect to the conventional H900 treatment, *stage II* was performed on new samples of the deposited S4 specimen with the aim to analyze if an increase in the hardness in the deposition layer can be obtained. Samples were drawn from S4 (S4_A2, S4_A3, S4_A4, S4_B2, S4_B3, S4_B4) in order to apply the HT1, HT2, and HT3 routes considering the different aging times.

Table 2.12 clarifies the planned heat treatments.

Table 2.12 Aging treatment routes performed during stage II.

Heat Treatment *Stage II*	**Aging time [min]**		
HT1	HT1_60 (sample S4_A2)	HT1_180 (sample S4_A3)	HT1_300 (sample S4_A4)
HT2	HT2_60 (sample S4_B2)	HT2_180 (sample S4_B3)	HT2_300 (sample S4_B4)
HT3	HT3_60 (sample S4_C2)	HT3_180 (sample S4_C3)	HT3_300 (sample S4_C4)

The conditions of the heat treatment HT1, with aging performed for 60 min, were not changed but two additional aging times were applied, 180 and 300 min. Instead, HT2 was characterized by a different austenitizing treatment because a short time austenitizing time was selected. In this case, the samples were put into the oven once the equipment reached the settled austenitizing temperature of 1040 °C. Conversely, in HT3 the austenitizing was completely avoided and direct aging for different times was applied. In the literature, the direct aging strategy was already tested by other researchers with good results in terms of mechanical properties for specimens fabricated by PBF [30]. No similar studies have been found when the DED process is used.

After the heat treatments, the specimens were firstly investigated by optical microscopy and Figure 2.26 shows the microstructure of the S4_A specimens in the HT1 conditions. As expected, after all the aging conditions the δ-ferrite phase is no more recognizable.

In Figure 2.27 the microstructure of the samples after HT2 routes are depicted. Despite the short austenitizing time, a martensitic matrix is detectable with no evidence of δ-ferrite.

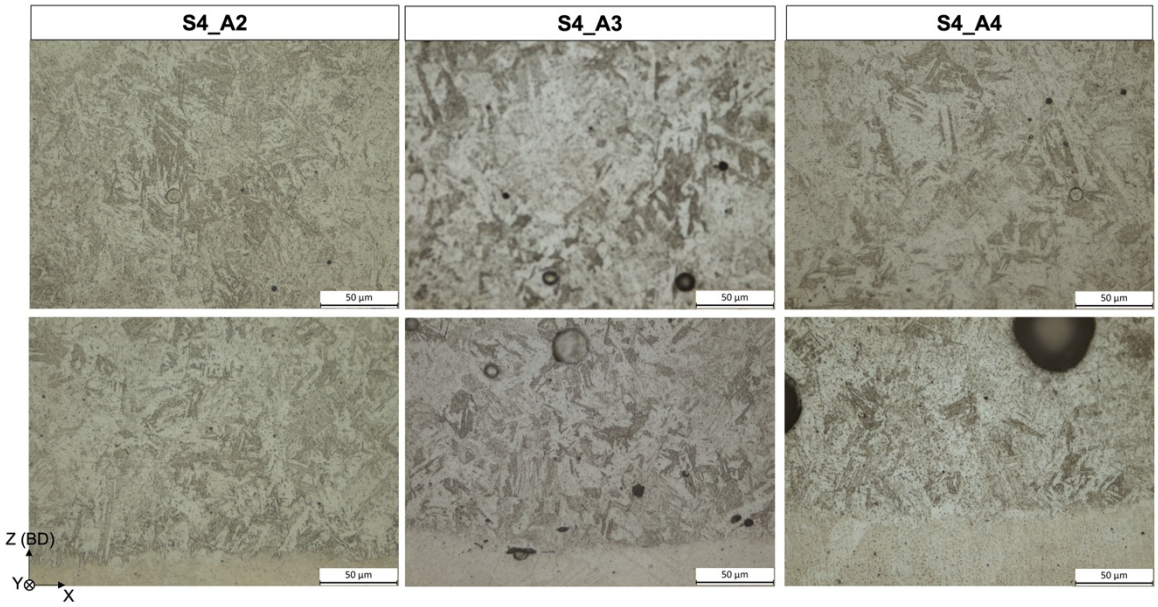

Figure 2.26 Microstructure of the specimens treated under HT1 at different aging times (A2: 60 min, A3: 180 min, and A4: 300 min).

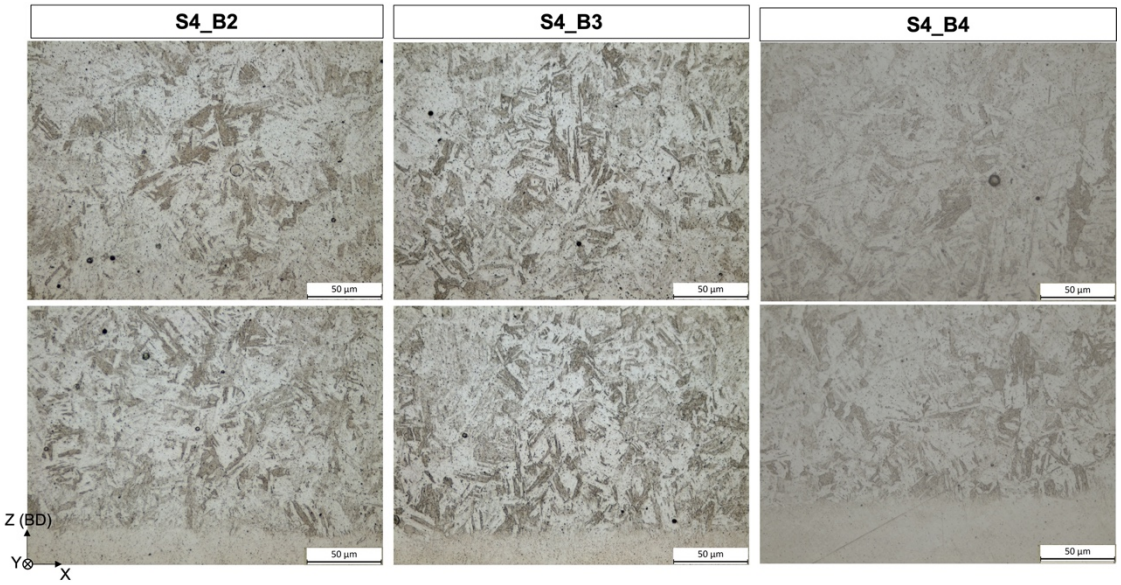

Figure 2.27 Microstructure revealed from the specimens treated under HT2 at different aging times (B2: 60 min, B3: 180 min, and B4: 300 min).

Conversely, the micrographs depicted in Figure 2.28 show that the absence of austenitizing has an important effect on the microstructure. The presence of the martensitic matrix with a needle-like structure and a high quantity of lathy δ-ferrite can be observed. In this case, δ-ferrite is maintained due to the lack of the heating at high temperatures.

In terms of timing between 60 and 180 min it could be depicted that the fineness of the lath martensite enhanced. On the contrary, when the time is increased to 300 min the martensite seemed overaged.

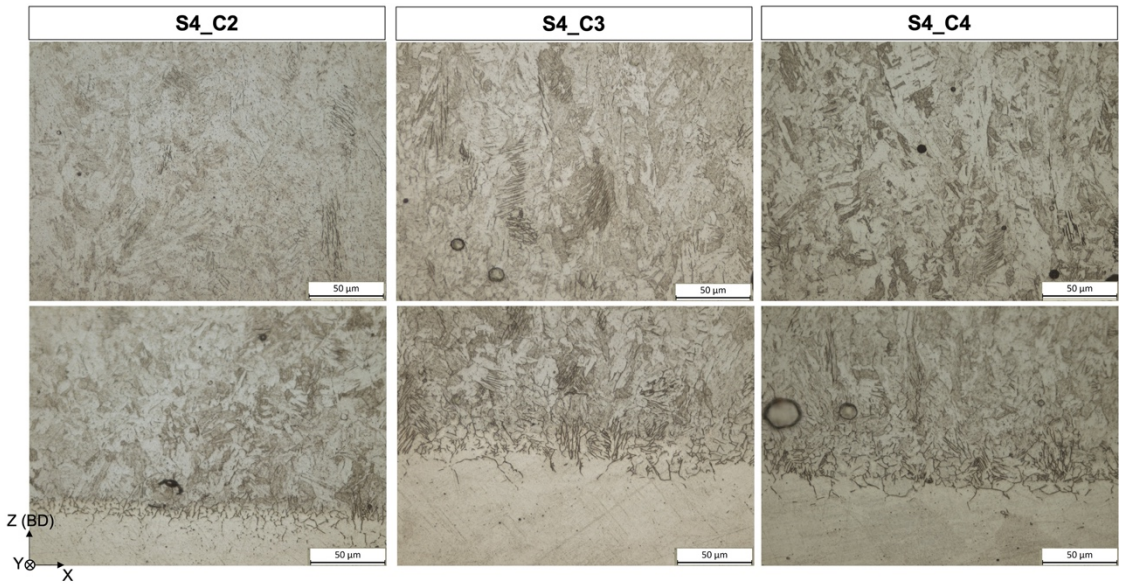

Figure 2.28 Microstructure revealed from the specimens treated under HT2 at different aging times (C2: 60 min, C3: 180 min, and C4: 300 min).

In all the treated samples, HV0.05 microhardness profiles were performed from the substrate to the top of the deposited layer, across the interface. In Figure 2.29, the plots of all the representative hardness profiles (HT1, HT2, HT3) for the different aging times are depicted. In HT2 samples, the hardness in the deposited layer is in the range 490 - 500 HV0.05, behaving very constantly among the different aging times, with a slight increase when 180 min are applied.

In the case of the HT3 conditions, with direct aging, the hardness was found to be the highest, reaching values of more than 520 HV0.05 when the aging time is maintained between 60 and 180 min.

As explained in the previous section, the microstructure is less defined when the aging time pass the 180 min seemed to be overage and decreases its hardness values. In terms of the variation of the solubilization treatment, it has been observed that when this treatment stage is avoided better results are found on the mechanical properties of the DED depositions. In accordance with some studies such as the ones performed by [30] during the DED depositions the materials already suffered so high temperatures induced by the laser which promotes that the microstructure behaves as a "pre solubilization" treatment, so when after the fabrication of a direct port aging treatment application is enough to increase its mechanical properties.

Figure 2.30 additionally shows a graphical comparison of the effect of the aging time versus the hardness values obtained during the test of *stage II.*

XRD analysis of all the samples aged for 180 min was performed in the same condition as for the as-built one. Figure 2.31 shows the three different XRD patterns, which are similar to the as-built one. As concerns the as-built and as already mentioned, the peaks of martensite are clearly present, being the martensite characteristic of the as-built state due to the high cooling rate suffered by the material during the DED process. All the samples subjected to heat treatments show similar XRD patterns, with the peaks of austenite which are more related to the substrate than to an effective increase of austenite in the layer. We need to remember that the single track is very so the austenitic γ peaks are surely related to the substrate. The presence of δ-ferrite in HT3 was not detected because of its pattern similar to the one of martensite. No peaks related to the Cu-rich nanoprecipitates were detected. In [42]–[44] authors explained how the change in the aging time has an effect on the revealing of Cu-rich precipitates only over 1000 hours of aging.

Because of these considerations the aim of *stage III* was to understand what would happen if samples were aged for longer times.

Hence, 100 hours of aging were applied to the deposited tracks of the sample S4, analyzing their hardness behavior. Their XRD analysis as well as longer aging treatments (338 hours) at the different solubilization conditions are currently an ongoing investigation in order to study of the long-term aging across the hardened precipitation across the samples and their effect on hardness behavior.

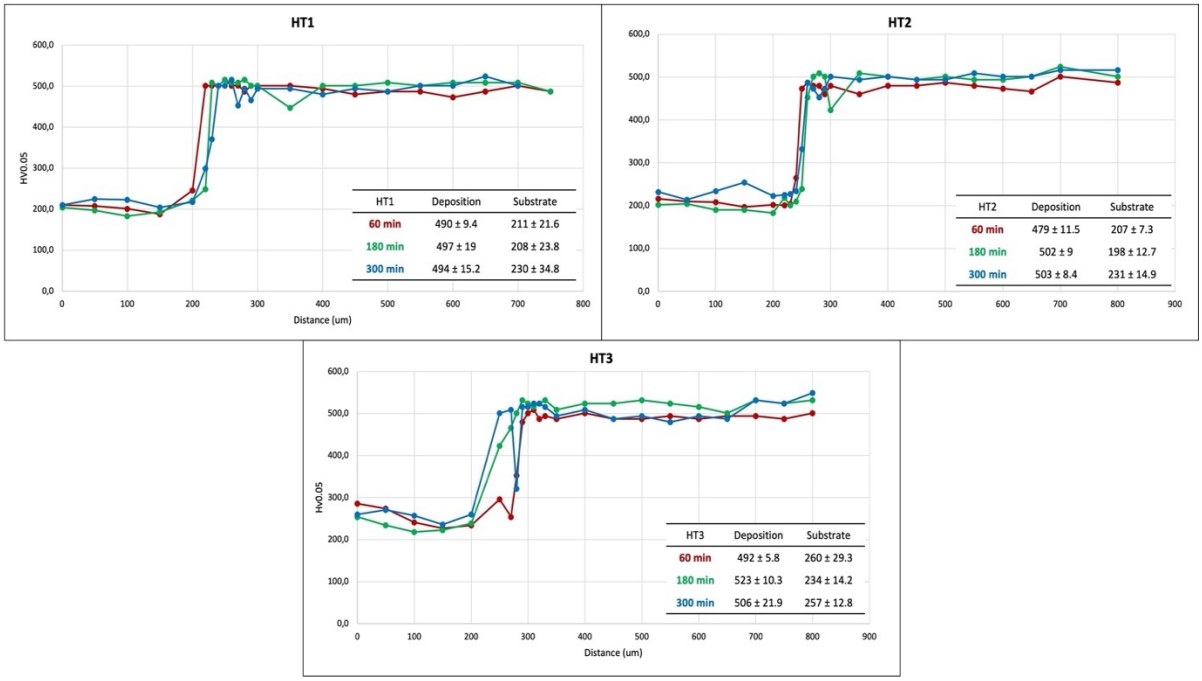

Figure 2.29 Vickers hardness profiles of the different heat treatment routes followed in stage II.

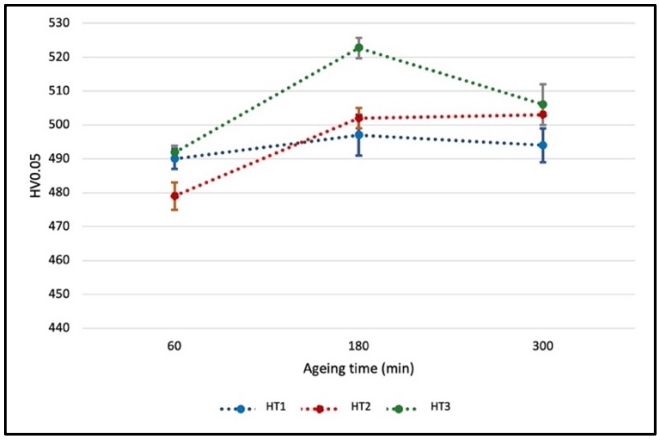

Figure 2.30 Vickers profile comparison among the three treatments in stage II in accordance with the aging time applied.

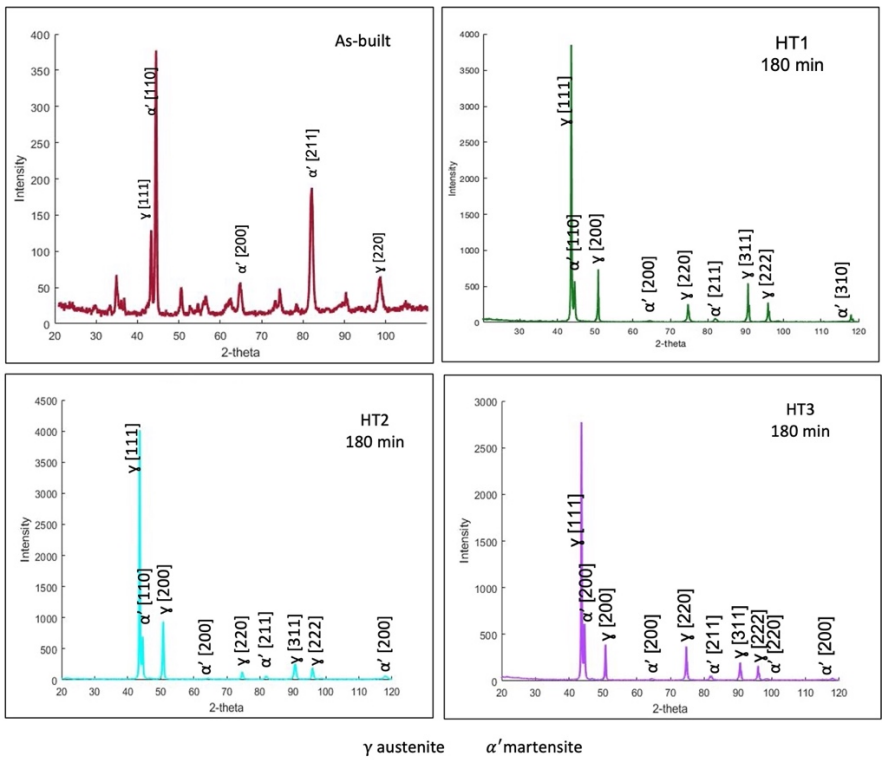

Figure 2.31 XRD patterns of as-built and each treated condition.

The hardness profiles of the samples aged for 100 hours are depicted in Figure 2.32.The increase in the number of hours causes a significant decrease in hardness for the different HT1, HT2, and HT3 heat treatment routes, with the highest values of hardness, after 100 hours, reached for the HT3 route (direct aging). Hence, this route is considered as the most feasible.

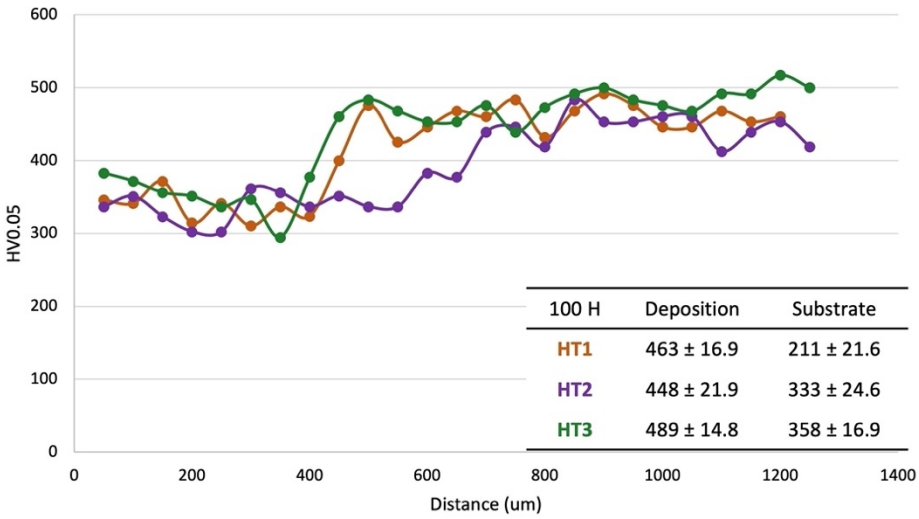

Figure 2.32 Hardness profiles for Ht1, HT2, and HT3 heat treatment routes after 100 hours of aging.

2.3 EXPERIMENTAL PROCEDURE FOR THE MULTITRACK DEPOSITIONS

Once the process parameters were deeply analyzed in terms of geometrical features, microstructure, and hardness properties, with and without heat treatment, multitrack depositions with the best process parameters were performed.

By means of the same gas-atomized 17-4 PH stainless steel powder, multilayer gas depositions were fabricated over AISI 316L stainless steel plates with the same equipment shown in Figure 2.3. Argon was used as shield gas with a flux of 6 L/min, employing a multidirectional scanning strategy with 90° of rotation for each layer, with a hatch distance of 1 mm and a layer thickness of 0.8 mm as depicted in Figure 2.33b. As concerns the adopted process parameter, a combination like S4, (see previous Table 2.13) was selected.

Some images of the fabricated samples, in the as-built condition, are depicted in Figure 2.33a. In particular, two multilayer samples with dimensions 60 mm x 30 mm and 20 layers were deposited.

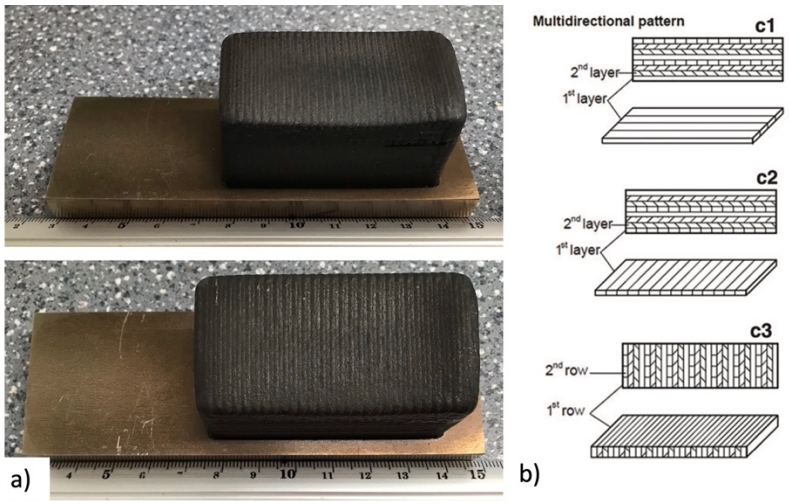

Figure 2.33 a) 17-4 PH multilayer deposited samples, and b) employed scanning strategy [45]

Table 2.13 Selected process parameters employed for fabricating the 17-4 PH multilayer samples.

	Power (*p*) [W]	**Scanning speed (*s*) [mm/s]**	**Power feed rate (*PFR*) [g/min]**	**Laser energy input (*E*) [J/mm²]**	**Volumetric energy density (VED) [J/mm²]**	**Dilution (D%) [%]**
S4	2160	20,0	20,0	49.1	86,4	11.1

The macro and microstructural analysis of the samples was performed by selecting specimens from two different areas: the top part of the multilayer sample and the interface part, respectively. In Figure 2.34., together with an image of on samples, is depicted a scheme of the two different specimens named “multilayer-deposition” and “multilayer-interface”, respectively. For their metallurgical inspection, performed by optical microscopy and scanning electron microscopy, both longitudinal and transversal directions were considered, and the same metallographic preparation procedure used for the single tracks was adopted.

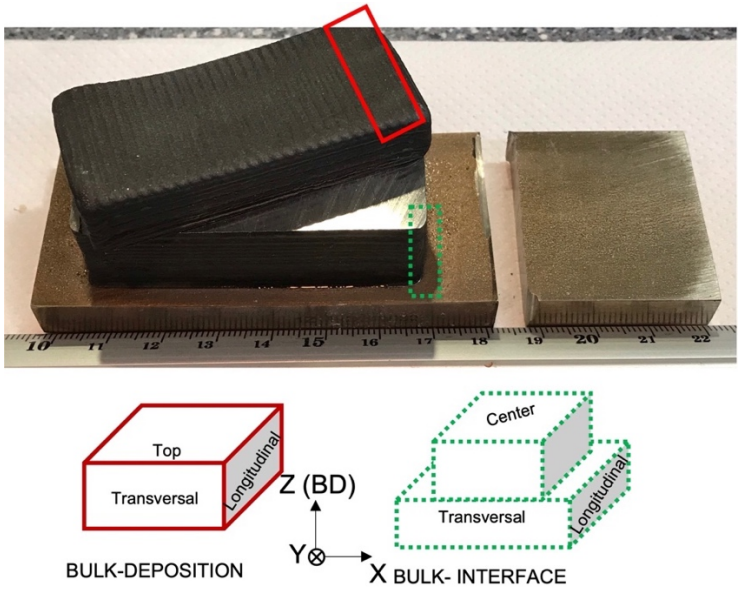

Figure 2.34 Selection of specimens from one of the 17-4 PH multilayer samples

All the optical metallographic inspections were carried out by the LEICA DMi8A optical microscopy, and the LAS image analysis software was used for calculating the percentage of porosity.

To corroborate the percentage of porosity apparent density tests were performed according to Archimedes' method. The ASTM B311 standard was followed, 40 mm x 30 mm x 15 mm specimens of the deposited parts were weighed in air (A, mass in air, g) and then in water (C, mass in water, g); the density of water was assumed as a constant according to its temperature (E, density of the water), the measure of support in water (C, mass of the support inside the water, g) and the measure of both piece plus the support inside the water (B, mass of both support and piece in water, g). Figure 2.35 show the system employed.

The Equation 2.1 was used to calculate the apparent density of the specimen.

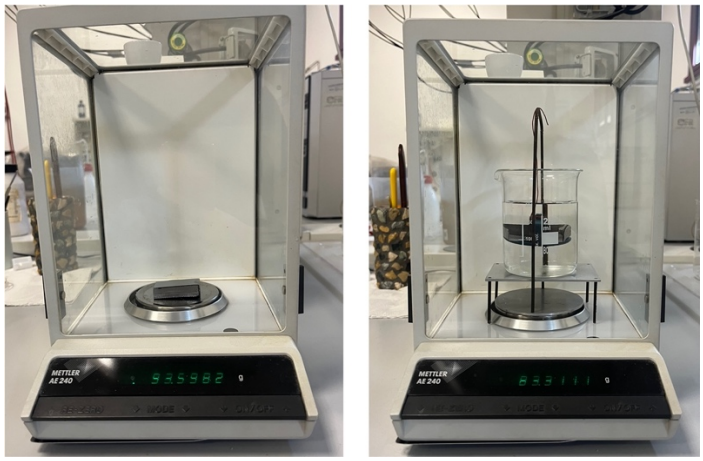

Figure 2.35 Archimedes' measuring system is employed for the determination of the apparent density of the samples.

Equation 2.1

$$D = A \Big/ \frac{[A-(B-C)]}{E}$$

Microhardness Vickers profiles at 50 gr_f (HV0.05) were also performed. XRD analyses of the deposited parts were carried out in the as-built condition as a comparison with the previous analysis conducted on single-track samples.

2.4 DISCUSSION OF THE MULTITRACK DEPOSITIONS RESULTS

2.4.1 Microstructural analysis without etching and density measurements

Porosity was detected in the material along both horizontal and vertical directions of the specimens (see Figure 2.36). In the same figure, examples of porosity measurements are reported. The porosity was mainly identified as gas porosity due to gas entrapped during the deposition of samples generated by the moisture of the powder.

According to Archimedes' measurements, the density of the materials was calculated as 7.62 g/cm^3 corresponding to a 98.32 % of the nominal density of a bulk 17-4 PH stainless steel (7.75 g/cm^3). Hence, despite the porosity observed in the specimens, the density of the depositions was considered acceptable, proof of the soundness of the parameters adopted in the L-DED process. In other studies, found in the literature, lower densities are reported with a 96 % of the nominal density of a bulk 17-4 PH stainless steel [46]. Table 2.14 demonstrate a comparison among the percentage of the porosity across the multilayer interface specimen with both techniques: image analysis and Archimedes method. As observed the difference between the two methods is high and this is due to the high error possibility of the image analysis one, however, the Archimedes method as mentioned before demonstrating to be still feasible for further applications.

Table 2.14 Porosity percent [Ap%] measured across the multilayer- deposition samples with the two different methods: image analysis and Archimedes 'method.

	Image analysis Ap %	Archimede's method Ap%
Multilayer 17-4 PH samples	0,00153	1,678

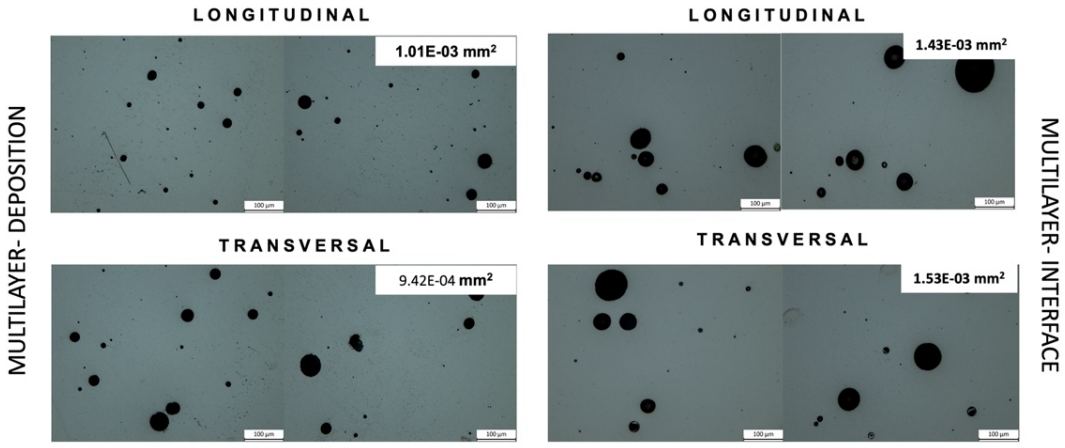

Figure 2.36 Porosity defect found across the diverse orientation of both 17-4 PH multilayer samples.

2.4.2 Microstructural analysis with etching

Through the visual analysis, the etched macrographs that conform the cubes shown across the next figures demonstrate the different melt pools as well as the layering direction, horizontally and vertically in accordance with the pattern followed during the deposition of the samples, which were deposited in multidirectional strategy. This kind of scanning strategy is usually employed to release and decrease a great quantity of heat input accumulation, giving the necessary time for the microstructure to grow and evolute during the solidification.

The microstructural analysis of the multilayer-deposition sample showed a very complex evolution across the specimens regardless of the analyzed direction since the size, shape, orientation, and distribution of the needle-like martensite changes a lot due to the interaction of the different layers. Figure 2.38 and Figure 2.39 demonstrates the analyzed sample in both directions that presents columnar martensite laths as well as a high presence of lathy δ-ferrite, which starts to grow from the interlayer between the melt pools and

towards the melt pool. This microstructural behavior is homogeneous across the whole piece, and it is affected by the high quantity of the heat input suffered during the layer deposition process and its consequent rapid cooling rate, effects that dictates the morphology evolution. Figure 2.37 demonstrate a micrograph of the top part of the multilayer-deposition sample, in which the contour zone was deposited in a unidirectional strategy.

Figure 2.37 Micrograph of the top part of the multilayer specimen, also known as contour area.

Across the two diverse analyzed directions of mentioned sample, it was observed that the layering deposition influence the growth morphology of the martensite as well as the one of the δ-ferrite, including its quantity. Figure 2.38 depicts the longitudinal analysis of the sample in which the change in the size, morphology, and distribution of the δ-ferrite beside the martensite shape it is observed as the distance from the top part increase (red arrows) which is consequence of the heat accumulation by the layering deposition and the cooling rate suffered during the process. It is observed as an example that the δ-ferrite in the furthermost zone of the top is larger and dispersive across the martensite laths, while in the top (Figure 2.40) which corresponds to the contour parameter presents a very strong growth of the needles of martensite with a lot of δ-ferrite within it are observed which is a consequence of the higher cooling rate.

In another hand, as Figure 2.39 show the same effects but in the transversal direction, the shape of the δ-ferrite phase as well as the martensite is show from the cross-sectional direction of the sample. Red arrows focus on the different microstructural morphology and size found in each zone.

Some spherical pores are depicted across the zones of both mentioned samples as are depicted. Figure 2.40 describes the representative micrographs of the microstructural analysis of the top part of the sample in which as described by the red arrows the growth of the columnar microstructure directions with a high presence of finer δ-ferrite phase is homogeneous across the zone.

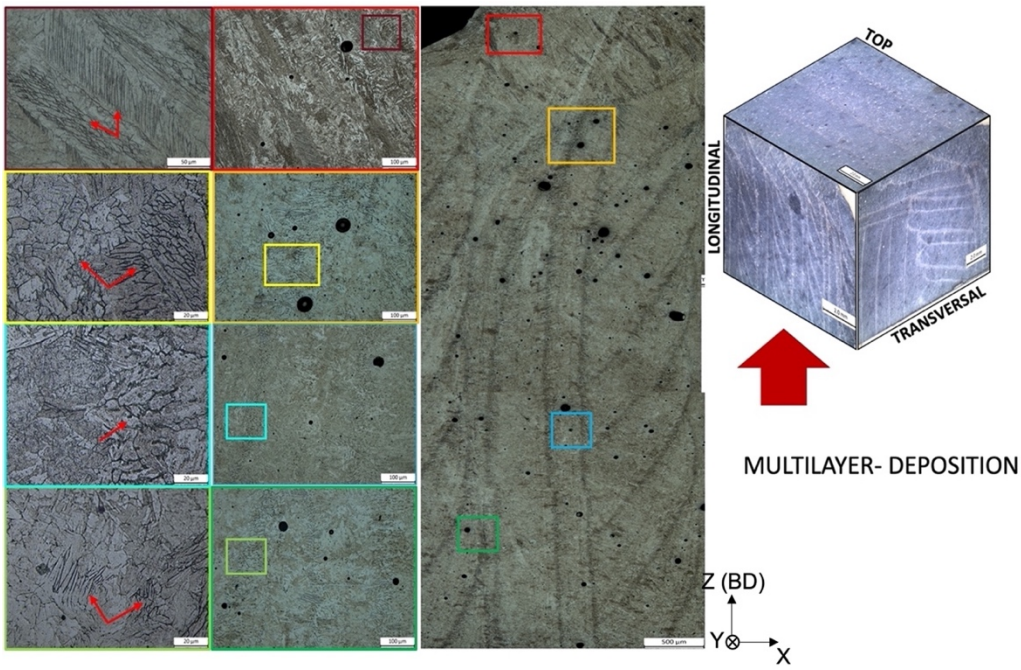

Figure 2.38 Microstructural analysis of the different zones of the longitudinal section of the multilayer deposited sample.

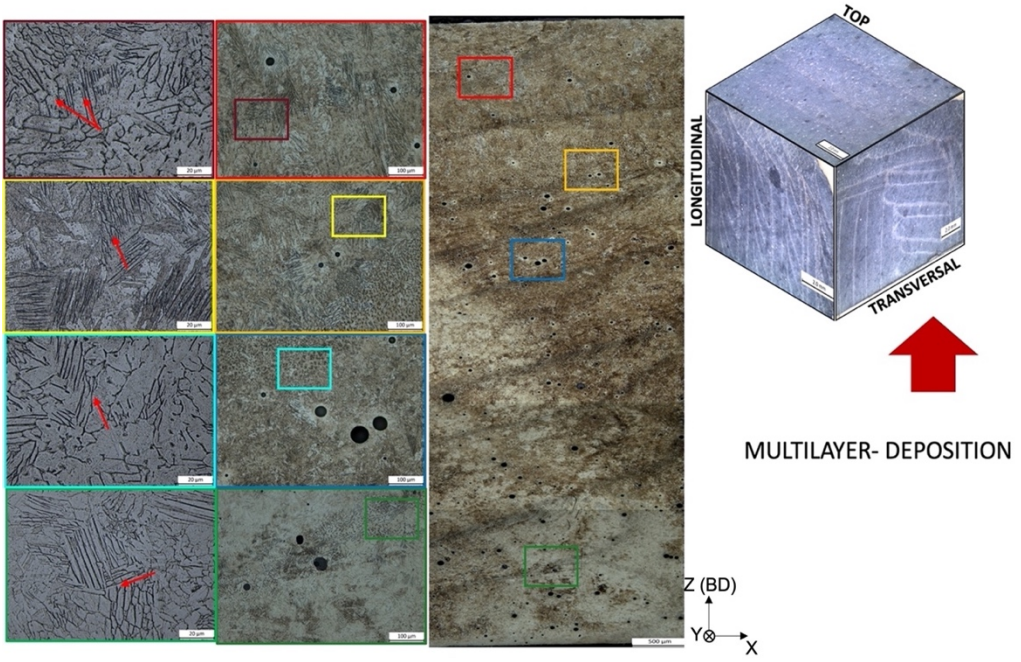

Figure 2.39 Microstructural analysis of the different zones of the transversal section of the multilayer deposited sample.

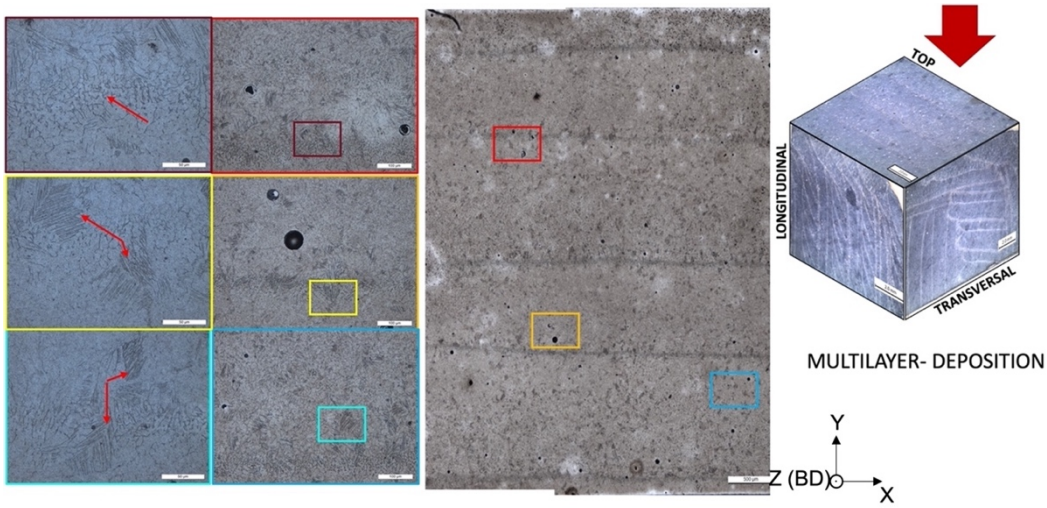

Figure 2.40 Microstructural analysis of different zones of the top part of the multilayer deposited sample.

Figure 2.41, Figure 2.42, and Figure 2.43 refer to the microstructural analysis of the multilayer-interface zone between the deposited layer and the substrate. The sequence of layering is clearly visible, the microstructure is characterized by a martensitic matrix even though high contents of δ-ferrite were detected just as in the previously analyzed zone. One of the points to highlight is that in Figure 2.41, the first deposited layers of the longitudinal section present a big lack of fusion across two deposited layers and a high quantity of open porosity, this effect as mentioned by the literature is commonly due to the stabilization of the material and the difference of the thermal condition among the first-second layer with the substrate. Meanwhile, across Figure 2.42 some pores filled with powder material were found (red arrows); this phenomenon commonly happens in additive manufacturing and in L-DED too [23]. Figure 2.43 instead shows the central part of the sample, in which in comparison with Figure 2.40 the microstructure seems less fine than in the top part, composed of martensite with the δ-ferrite.

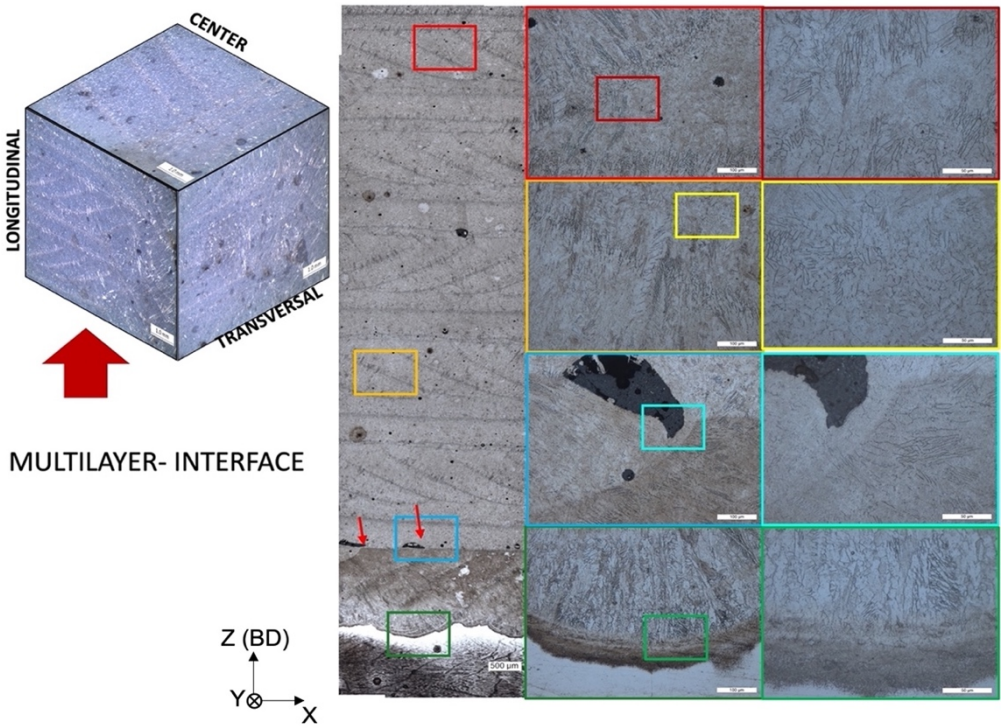

Figure 2.41 Microstructural analysis of the different zones of the longitudinal section of the multilayer-interface sample.

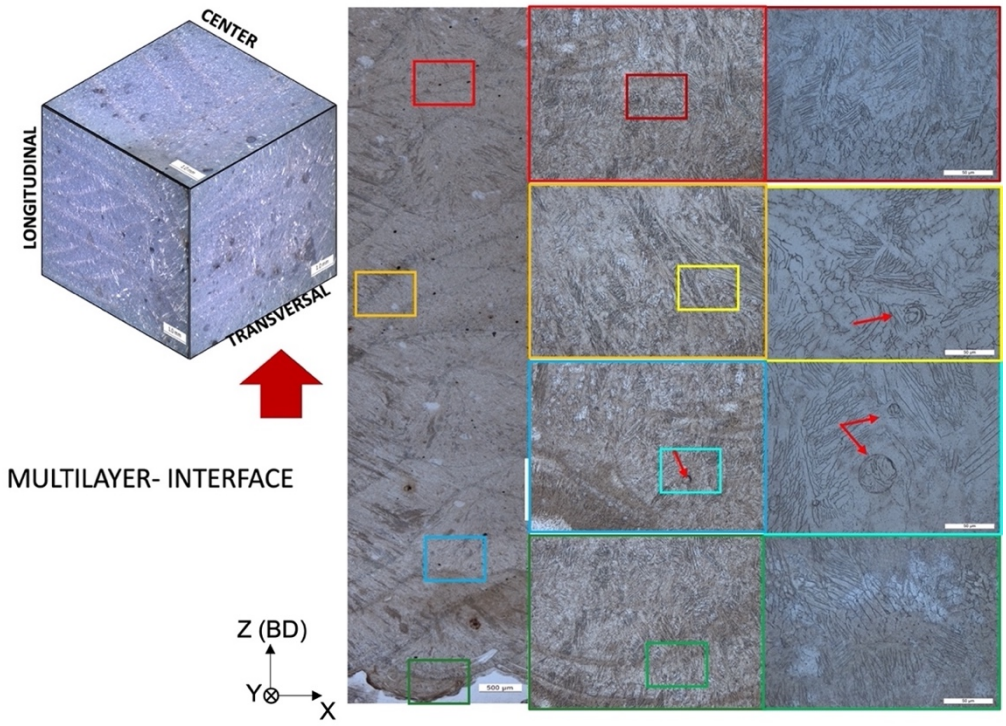

Figure 2.42 Microstructural analysis of the different zones of the transversal section of the multilayer-interface sample.

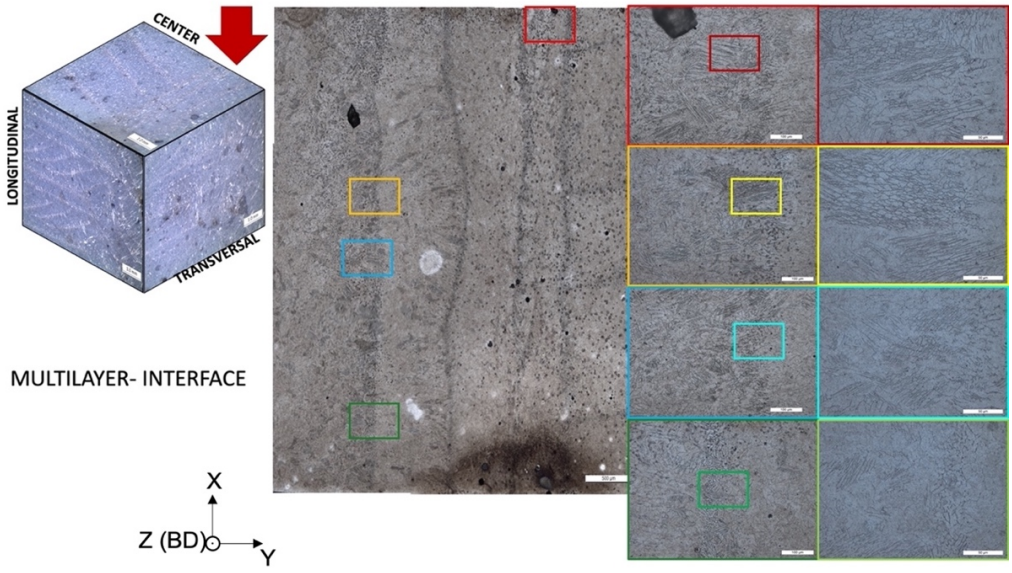

Figure 2.43 Microstructural analysis of different zones of the central section of the multilayer-interface sample.

An XRD pattern was also performed in the material (see Figure 2.44), demonstrating the presence of only martensite across the specimen. The δ-ferrite was not identified as separate peaks but confused in the ones of martensite. No austenitic peaks were identified.

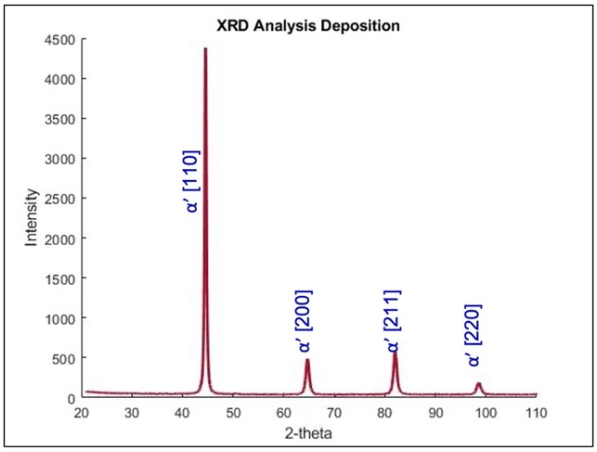

Figure 2.44 XRD pattern of the multilayer 17-4 PH sample.

2.4.3 Hardness analysis

Microhardness profiles with a 50 gr_f load were performed along the samples near the top of the deposition. Mean values of hardness of about 375 HV0.05 were measured, in good agreement with the as-built single-track depositions discussed at the beginning of this chapter. In Figure 2.45 two representative profiles, together with hardness measurements, performed along both longitudinal and transversal directions are shown. The scatter of data is high due to the variation of microstructure across the different layers. Some indentations felt inside the melt pool, others in the inter-track zones, showing significant differences in the hardness values. Figure 2.46 shows two representative hardness profiles performed at the interface between the substrate and the deposition; in this zone, the scatter of data is less than at the top of the deposition with mean hardness values in the range 330 – 350 HV0.05 for both transversal and longitudinal sections.

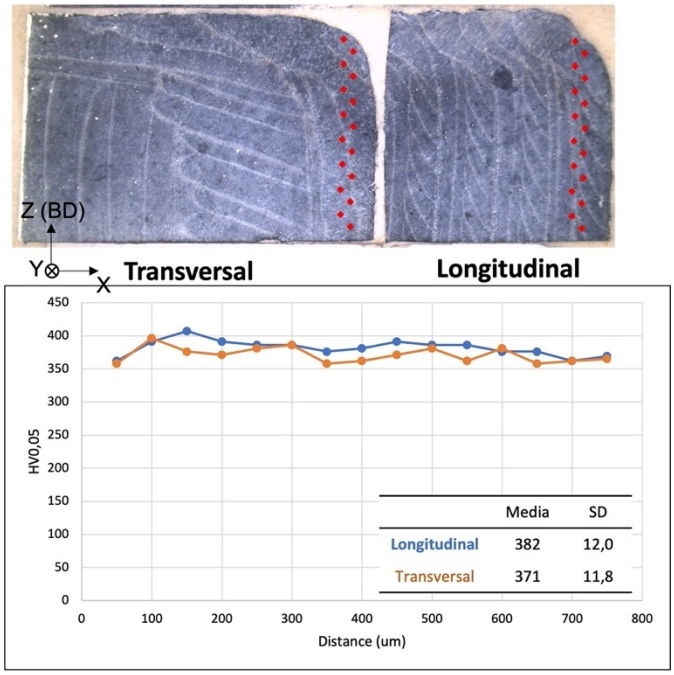

Figure 2.45 Hardness profiles of the transversal and longitudinal section of the multilayer deposited sample.

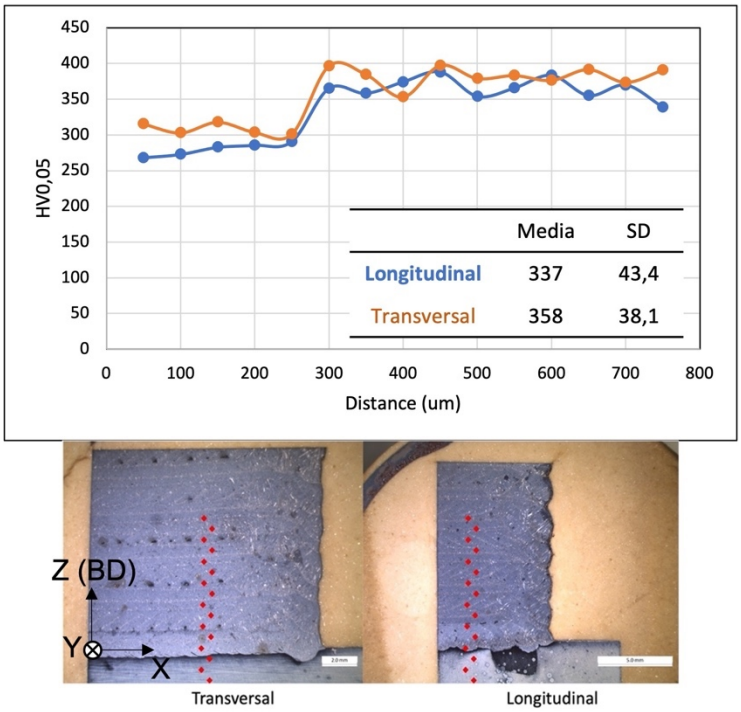

Figure 2.46 Hardness profiles of the transversal and longitudinal sections at the interface between substrate and deposition.

2.5 CONCLUDING REMARKS

17-4 PH stainless steel atomized powder was employed to deposit single-tracks on AISI 316 L stainless steel plates using different process parameter conditions by means of the L-DED technique. A preliminary analysis was performed on the eighty-one deposited tracks in order to check the presence of potential macro-defects and geometrical non-conformities. The research was the narrowed up and the study was focused on the most promising process parameters.

Four different process conditions with a laser energy density in the range of 39-52 J/mm^2 were selected according to the best performance in terms of low porosity, appropriate dilution, and low defect content across the tracks. Specimens were drawn from tracks fabricated with these four selected conditions and subjected to deep investigation. The most important geometrical features were measured in order to calculate dilution and the microstructure was further explored. The microstructure of the specimens in the as-built specimens was mainly characterized by an equiaxial lath martensitic matrix in which is embedded a high quantity of lathy δ-ferrite, mostly across the interface but also found along the deposited tracks. The effect of the process conditions significantly affected the quantity and distribution of the δ-ferrite. Hardness measurements and XRD analyses were also carried out to determine the most promising process parameters for fabricating feasible L-DED depositions. According to obtained results, S4 process parameters were demonstrated to be the most promising in terms of performance. In fact, in addition to the best results in terms of geometrical features and dilution, the microstructure of sample S4 showed less quantity (8,88 %) of δ-ferrite and a more defined martensitic matrix. As concerns the hardness, the lower amount of δ-ferrite was also responsible for the highest mean hardness values (393 ± 46) in the as-built condition. Unfortunately, the XRD analysis was not as much as successful in identifying the differences in terms of δ-ferrite contents and the small dimensions of the tracks did not permit to avoid the presence of the austenite peaks belonging to the AISI 316L substrate.

Some post-fabrication heat treatment routes were specifically designed starting from the time and temperature suggested for the conventional H900 heat treatment established for the 17-4 PH stainless steel. It was detected that microstructural changes occurred at the

different stages of the different designed heat treatment routes. If austenitizing at 1040 °C is performed on the material, the dissolution of the δ-ferrite occurs.

Two more heat treatment cycles were applied considering different times and temperatures of austenitizing and aging with respect to the H900 treatment. In particular, it was found that, when austenitizing is omitted, it is possible to obtain the highest hardness values after 3 hours of aging. The direct aging promotes in this case an increase in the hardness up to 523 ± 10 HV0.05. However, in terms of the aging time variation, the specimens that were directly aged within the range of 180-300 min of dwelling time, showed the most promising hardness values with an adequate microstructure behavior. Direct aging up to 100 hours was performed in order to check the precipitation of the Cu-rich nanoparticles by XRD analysis. Unfortunately, this dwelling time was not also enough to detect them in the XRD pattern. Further investigations are still ongoing with dwelling aging time for more than 1000 hours.

Finally, multilayer depositions were fabricated with the best process parameters found studying the single-track depositions and deeply analyzed. These depositions showed an apparent density value of 98.32%, measured by means of the Archimedes method. The density measured with this conventional method was also compared with the one estimated by image analysis of porosity. The microstructural analysis of the samples showed the presence of a high quantity of δ-ferrite inside the columnar lathy martensite grains. The highest amount of δ-ferrite phase was found across the interface along with the martensitic grains, whose dimension varies from coarse to finer across the different layers. The results obtained from these last inspections assess that preliminary studies performed on single deposited tracks are a good technique to find the most promising process condition to be used in multilayer depositions. The L-DED process applied to the 17-4 PH is less studied in the literature, but it has good potential for real and reliable applications.

Apart from the results presented in this doctoral thesis, this is an ongoing research and results will be soon submitted to be published in international journals.

2.6 REFERENCES

[1] Perrin. Walker and W. H. Tarn, *Handbook of Metal Etchants*. CRC Press, 1991.

[2] F. V. V. George, “Applied Metallography of Stainless Steels,” *JOM*, pp. 1–6, Mar. 1989.

[3] H. el Cheikh, B. Courant, S. Branchu, J. Y. Hascoët, and R. Guillén, “Analysis and prediction of single laser tracks geometrical characteristics in coaxial laser cladding process,” *Opt Lasers Eng*, vol. 50, no. 3, pp. 413–422, Mar. 2012, doi: 10.1016/j.optlaseng.2011.10.014.

[4] W. Elisabeth, “Metallographic preparation of stainless steel,” 2019.

[5] K. Small, D. Englehart, and T. Chritsman, “Guide to Etching specialty alloys,” 2008.

[6] R. Leal *et al.*, “Additive manufacturing tooling for the automotive industry,” *International Journal of Advanced Manufacturing Technology*, vol. 92, no. 5–8, pp. 1671–1676, Sep. 2017, doi: 10.1007/s00170-017-0239-8.

[7] S. Sreekanth, “Laser-Directed Energy Deposition : Influence of Process Parameters and Heat-Treatments,” University West, 2020.

[8] U. de Oliveira, V. Ocelík, and J. T. M. de Hosson, “Analysis of coaxial laser cladding processing conditions,” *Surf Coat Technol*, vol. 197, no. 2–3, pp. 127–136, Jul. 2005, doi: 10.1016/j.surfcoat.2004.06.029.

[9] P. Y. Lin, F. C. Shen, K. T. Wu, S. J. Hwang, and H. H. Lee, “Process optimization for directed energy deposition of SS316L components,” *International Journal of Advanced Manufacturing Technology*, vol. 111, no. 5–6, pp. 1387–1400, Nov. 2020, doi: 10.1007/s00170-020-06113-z.

[10] S. Shin, S.-M. Kwon, C. Kim, J. Lee, J. Hwang, and H. KIm, “Optimization of Direct Energy Deposition of 304L Stainless Steel through Laser Process Parameters,” *Journal of Welding and Joining*, vol. 39, no. 2, pp. 182–188, 2021, doi: 10.5781/jwj.2021.39.2.7.

[11] A. Dass and A. Moridi, “State of the art in directed energy deposition: From additive manufacturing to materials design,” *Coatings*, vol. 9, no. 7. MDPI AG, 2019. doi: 10.3390/COATINGS9070418.

[12] A. Dass and A. Moridi, “State of the art in directed energy deposition: From additive manufacturing to materials design,” *Coatings*, vol. 9, no. 7, 2019, doi: 10.3390/COATINGS9070418.

[13] L. Rovatti, J. N. Lemke, M. Colombo, O. Stejskal, and M. Vedani, “Effetti della diluizione sulla microstruttura e comportamento ad usura di una lega Fe-C-B-Cr-Mo,” *Metallurgia Italiana*, vol. 107, no. 3, pp. 15–22, 2015.

[14] A. Bayode, E. T. Akinlabi, and S. Pityana, “Microstructure and Microhardness of 17-4 PH Stainless Steel Made by Laser Metal Deposition,” in *World Congress on Engineering and Computer Science*, 2016, p. 1040.

[15] L. Peng *et al.*, “Direct laser fabrication of nickel alloy samples,” *Int J Mach Tools Manuf*, vol. 45, no. 11, pp. 1288–1294, Sep. 2005, doi: 10.1016/j.ijmachtools.2005.01.014.

[16] D. Svetlizky *et al.*, “Directed energy deposition (DED) additive manufacturing: Physical characteristics, defects, challenges and applications,” *Materials Today*, vol. 49, pp. 271–295, Oct. 2021, doi: 10.1016/j.mattod.2021.03.020.

[17] D.-G. Ahn, “Directed Energy Deposition (DED) Process: State of the Art,” *International Journal of Precision Engineering and Manufacturing - Green Technology*, vol. 8, no. 2, pp. 703–742, Mar. 2021, doi: 10.1007/s40684-020-00302-7.

[18] H. Gu, H. Gong, D. Pal, K. Rafi, T. Starr, and B. Stucker, “Influences of Energy Density on Porosity and Microstructure of Selective Laser Melted 17-4PH Stainless Steel.”

[19] P. Ferro, R. Meneghello, G. Savio, and F. Berto, “A modified volumetric energy density-based approach for porosity assessment in additive manufacturing process design”, doi: 10.1007/s00170-020-05949-9/Published.

[20] M. Liu, A. Kumar, S. Bukkapatnam, and M. Kuttolamadom, “A Review of the anomalies in Directed Energy Deposition (DED) processes and potential solutions.”

[21] H. Gu, H. Gong, D. Pal, K. Rafi, T. Starr, and Brent. Stucker, “Influences of Energy Density on Porosity and Microstructure of Selective Laser Melted 17- 4PH Stainless Steel,” in *24th Annual International Solid Freeform Fabrication Symposium*, 2013, pp. 474–489.

[22] M. Ghayoor, K. Lee, Y. He, C.-H. Chang, B. K. Paul, and S. Pasebani, “Selective Laser Melting of 304L Stainless Steel: Role of Volumetric Energy Density on the Microstructure, Texture and Mechanical Properties.”

[23] T. DebRoy *et al.*, “Additive manufacturing of metallic components – Process, structure and properties,” *Progress in Materials Science*, vol. 92. Elsevier Ltd, pp. 112–224, Mar. 01, 2018. doi: 10.1016/j.pmatsci.2017.10.001.

[24] L. Badi, “Effect of Process Parameters on the Quality of 17-4 PH Samples Produced by Directed Energy Deposition,” Politecnico di Torino, 2021.

[25] D. Herzog, V. Seyda, E. Wycisk, and C. Emmelmann, “Additive manufacturing of metals,” *Acta Mater*, vol. 117, pp. 371–392, Sep. 2016, doi: 10.1016/j.actamat.2016.07.019.

[26] M. Bahrami Balajaddeh and H. Naffakh-Moosavy, “Pulsed Nd:YAG laser welding of 17-4 PH stainless steel: Microstructure, mechanical properties, and weldability

investigation," *Opt Laser Technol*, vol. 119, no. June, 2019, doi: 10.1016/j.optlastec.2019.105651.
[27] A. Ziewiec, A. Zielińska-Lipiec, and E. Tasak, "Microstructure of welded joints of X5CrNiCuNb 16-4 (17-4 PH) martensitic stainlees steel after heat treatment," *Archives of Metallurgy and Materials*, vol. 59, no. 3, pp. 965–970, 2014, doi: 10.2478/amm-2014-0162.
[28] R. Saluja and K. M. Moeed, "The emphasis of the fase transformations and alloying constituents on hot cracking susceptibility of type 304L and 316L SS welds," *International Journal of Engineering Science and Technology,* vol. 4, no. 05, pp. 2206–2216, 2012.
[29] G. Jacob, "Prediction of Solidification Phases in Cr-Ni Stainless Steel Alloys Manufactured by Laser Based Powder Bed Fusion Process." Advanced Manufacturing Series (NIST AMS), National Institute of Standards and Technology, Gaithersburg, MD, Jan. 2018. doi: https://doi.org/10.6028/NIST.AMS.100-14.
[30] S. Sabooni *et al.*, "Laser powder bed fusion of 17–4 PH stainless steel: A comparative study on the effect of heat treatment on the microstructure evolution and mechanical properties," *Addit Manuf*, vol. 46, p. 102176, 2021, doi: https://doi.org/10.1016/j.addma.2021.102176.
[31] S. İRİZALP and B. KÖROĞLU, "Effect of high-energy laser welding parameters on the microstructure and mechanical properties of 304 stainless steel," *Dokuz Eylul University Faculty of Engineering Journal of Science and Engineering*, vol. 23, no. 67, pp. 179–194, 2021, doi: 10.21205/deufmd.2021236716.
[32] Z. Feng, "The Lattice parameter of gamma iron and iron-chromium alloys," 2015.
[33] P. D. Nezhadfar *et al.*, "Fatigue crack growth behavior of additively manufactured 17-4 PH stainless steel: Effects of build orientation and microstructure," *Int J Fatigue*, vol. 123, pp. 168–179, Jun. 2019, doi: 10.1016/j.ijfatigue.2019.02.015.
[34] I. Mathoho, E. T. Akinlabi, N. Arthur, and M. Tlotleng, "Impact of DED process parameters on the metallurgical characteristics of 17-4 PH SS deposited using DED," *CIRP J Manuf Sci Technol*, vol. 31, no. 2019, pp. 450–458, 2020, doi: 10.1016/j.cirpj.2020.07.007.
[35] ASTM International, "Standard Specification for Precipitation-Hardening Stainless and Heat-Resisting Steel Plate, Sheet, and Strip." [Online]. Available: www.astm.org,
[36] D. F. A. Ferreira, R. P. Rezende, and T. Turcarelli, "MICROSTRUCTURAL CHARACTERIZATION OF STAINLESS STEEL 17-4 PH USED IN THE CONTROL ELEMENT OF PWR-TYPE REACTORS SUBMITTED TO DIFFERENT HEAT TREATMENTS," in *2017 International Nuclear Atlantic Conference - INAC 2017*, 2017, pp. 1–10.
[37] S. N. el Moghazi, T. Wolfe, D. G. Ivey, and H. Henein, "Plasma transfer arc additive manufacturing of 17-4 PH: assessment of defects," *The International Journal of Advanced Manufacturing Technology,* vol. 108, pp. 2301–2313, 2020, doi: 10.1007/s00170-020-05540-2/Published.
[38] Y. Sun, R. J. Hebert, and M. Aindow, "Effect of heat treatments on microstructural evolution of additively manufactured and wrought 17-4PH stainless steel," *Mater Des*, vol. 156, pp. 429–440, Oct. 2018, doi: 10.1016/j.matdes.2018.07.015.
[39] L. Pan *et al.*, "Enhancement in hardness and corrosion resistance of directed energy deposited 17-4 PH martensitic stainless steel via heat treatment," *Journal of Materials Research and Technology*, Mar. 2023, doi: 10.1016/j.jmrt.2023.01.114.
[40] Z. Zhao *et al.*, "Effect of Solution Temperature on the Microstructure and Properties of 17-4PH High-Strength Steel Samples Formed by Selective Laser Melting," *Metals (Basel)*, vol. 12, no. 3, p. 425, Feb. 2022, doi: 10.3390/met12030425.

[41] H. R. Lashgari, C. Kong, E. Adabifiroozjaei, and S. Li, “Microstructure, post thermal treatment response, and tribological properties of 3D printed 17-4 PH stainless steel,” *Wear*, vol. 456–457, Sep. 2020, doi: 10.1016/j.wear.2020.203367.

[42] X. Ma *et al.*, “Spinoidal decomposition of precipitation hardening Fe-17Cr-4Ni-4Cu Stainless Steel at 475 C,” *Materiali in Tehnologije*, vol. 56, no. 2, pp. 193–199, 2022, doi: 10.17222/mit.2021.336.

[43] R. Bhambroo, S. Roychowdhury, V. Kain, and V. S. Raja, “Effect of reverted austenite on mechanical properties of precipitation hardenable 17-4 stainlesssteel,” *Materials Science and Engineering A*, vol. 568, pp. 127–133, Apr. 2013, doi: 10.1016/j.msea.2013.01.011.

[44] C. N. Hsiao, C. S. Chiou, and J. R. Yang, “Aging reactions in a 17-4 PH stainless steel,” *Mater Chem Phys*, vol. 74, no. 2, pp. 134–142, 2002, doi: https://doi.org/10.1016/S0254-0584(01)00460-6.

[45] L. Pham, G. Lu, and P. Tran, “Influences of Printing Pattern on Mechanical Performance of Three-Dimensional-Printed Fiber-Reinforced Concrete,” *3D Print Addit Manuf*, vol. 9, no. 1, pp. 46–63, 2022, doi: 10.1089/3dp.2020.0172.

[46] A. D. Akessa, W. M. Tucho, H. G. Lemu, and J. Grønsund, “Investigations of the Microstructure and Mechanical Properties of 17-4 PH ss Printed Using a MarkForged Metal X,” *Materials*, vol. 15, no. 19, Oct. 2022, doi: 10.3390/ma15196898.

CHAPTER 3 L-DED WC-Co HARD FACING DEPOSITIONS: MICROSTRUCTURAL AND HARDNESS BEHAVIOR

The purpose of the present chapter is to present the research activity carried on a WC-12Co composite material (commonly known as cermet or hard metal) fabricated by L-DED. The WC-Co investigation was divided into two parts. The first one consisted of the metallurgical characterization of depositions performed on two different substrates (a C4 carbon steel and a HSS 390 steel) considering the effect of the process parameters such as the laser power, the scanning speed, and the powder feed rate. In the second part, new samples were deposited maintaining the substrate material, the scanning speed, and the powder feed rate as constants, while adopting different laser power values. Only in the last part of the investigation, the effect of different scanning strategies was investigated.

3.1 EXPERIMENTAL PROCEDURE FOR THE WC-CO

Sintered WC powders with 12% of Co supplied by Il Sentiero International Campus (Magreta, Italy) were employed for manufacturing multitrack on 120 x 40 x 10 mm plates. A picture of one of the fabricated samples is reported in Figure 3.1. Two different materials were chosen as substrates: a low-carbon steel (C4) and an HSS 390 high-speed steel. Unfortunately, the powder used for fabricating the samples was not homogeneous; analyses performed by the supplier revealed a morphology of the powder mainly characterized by non-homogeneous spherical-shaped crushed particles (see Figure 3.2). As can also be noted by the micrographs reported in Figure 3.3, the powder is characterized by the presence of some agglomerates of carbides and a high quantity of porosity; this is due to their production processing, and in most cases strictly correlated to the general quality of the depositions [1], [2]. The powder chemical composition, determined via a semiquantitative analysis employing a Zeiss EVO MA 15 (Carl Zeiss, Jena, Germany) scanning electron microscope equipped with an Oxford Xmax 50 (Oxford Instruments, Abingdon-on-Thames, UK) microprobe for energy-dispersive spectroscopy (SEM/EDS) is shown in Table 3.1. In Table 3.2 are collected the chemical composition (wt. %) of both the materials employed as substrates.

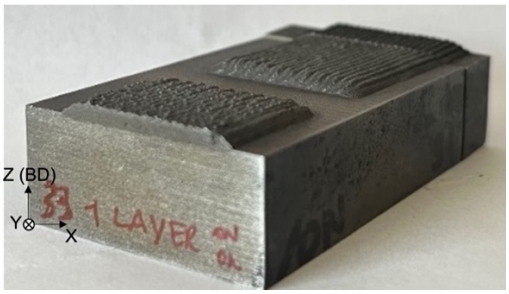

Figure 3.1 Example of fabricated WC-12Co depositions

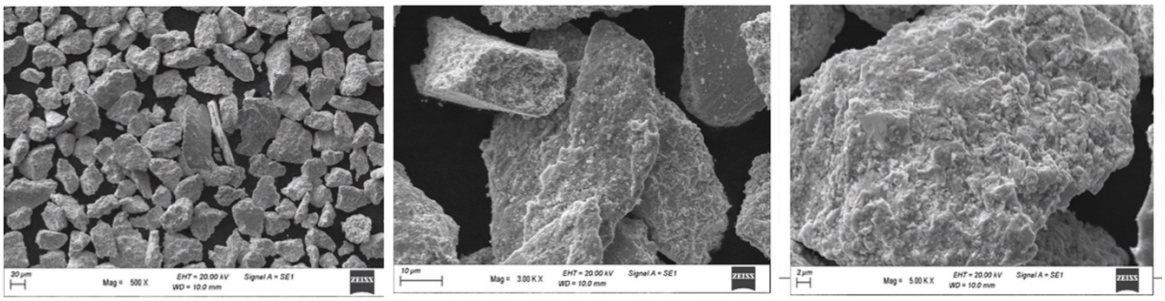

Figure 3.2 SEM micrographs of the WC-12Co powder particles.

Table 3.1 Chemical composition (wt.%) of the WC-12Co employed in this experimentation.

Chemical composition [wt.%]	C	Si	Mn	Cr	Mo	V	Co	Fe	W
WC-Co	5.49						11.94	0.022	Balance

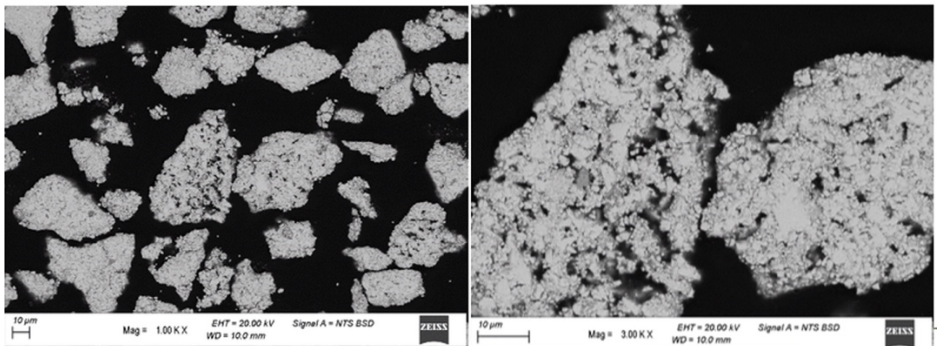

Figure 3.3 Cross-sectional WC-12Co powder particles SEM micrographs.

Table 3.2 Chemical composition (wt.%) of the employed substrates.

Chemical composition [wt.%]	C	Si	Mn	Cr	Mo	V	W	Co	Fe
Substrate 1 HSS 390	1.64	0.60	0.30	4.80	2	4.80	10.40	8	Balance
Substrate 2 Low carbon steel (C4)	0.07-0.13	0.4	0.3-0.6						

The same six-axis ABB IRB 4600 (ABB, Zurich, Switzerland) robot (Figure 2.3) available at the Birex Competence Center (Bologna – Italy) and equipped with a coaxial nozzle with 6 heads, a laser line source of 4.5 kW and argon as a carrier and shield gas in flow rates of 3 L/min and 6 L/min, respectively, was used to manufacture the samples. The robot was also equipped with a v2.0 CLAMIR camera (CLAMIR, Madrid, Spain), which was used to control the laser power and monitor the melt pool size during the process.

The experimental investigation was divided into two parts as depicted in Figure 3.4. In the first part different process parameters, different substrate materials, and number of deposited layers were considered. In the second part of the study, only the power and the scanning strategy were varied, while considering the other parameters as constants.
In Table 3.3 are collected the combinations of the process parameters employed in this investigation. In particular, the laser power (W) was in the range 900-1300 W, the scanning speed was in the range 8-10 mm/s and the PFR was in the range 6,7 -11,1 g/min. The codification of the fabricated sample is reported in Table 3.4.

As concerns the scanning strategy, it is worth noting that there are plenty of different types of scanning strategies that can be used in a laser deposition procedure but the most common are the raster, the unidirectional, the bi-directional, the fractal or multidirectional [3]–[5]. In the present study three diverse scanning strategies were employed to fabricate the samples; they were named ON_ON, ON_OFF, and CLAMIR according to the adopted management of the laser. In the ON_ON strategy is laser is continuously turned-on during the deposition, while in the ON_OFF strategy the laser is turned-on only during the deposition, then it is shutdown from the passage from layer to layer. Conversely, the CLAMIR strategy is an ON_OFF but with the advantage of the use of camera able to control the movement of the laser during the process.

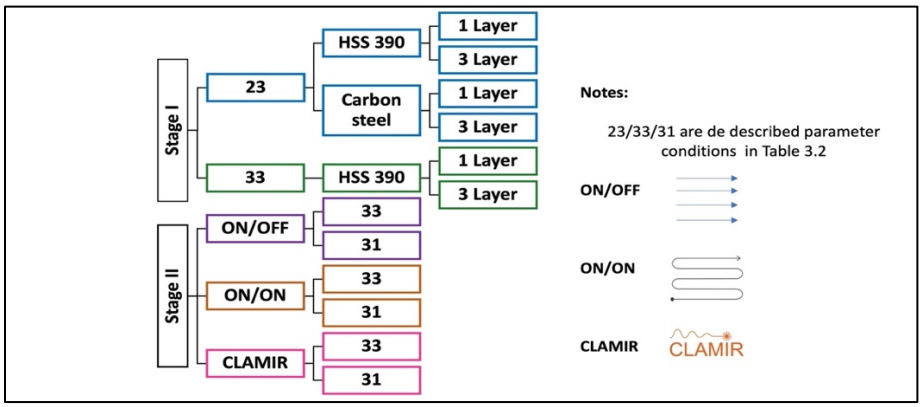

Figure 3.4 Process parameters plan adopted with WC-12Co.

Table 3.3 Process parameters conditions used during the experimental work.

Sample	Power [W]	Scanning speed [mm/s]	PFR [g/min]
Condition 23	1100	10	6,7
Condition 33	900	8	11,2
Condition 31	1300	8	11,2

Table 3.4 Codification of WC-12Co samples

Part	Substrate material	Scanning strategy	# of layers	Process parameters	Denomination
I	HSS	ON_ON	1	23	S1
	HSS	ON_ON	3	23	S2
	Steel	ON_ON	1	23	S3
	Steel	ON_ON	3	23	S4
	HSS	ON_ON	1	33	S5
	HSS	ON_ON	3	33	S6
II	HSS	ON_ON	1	31	S7
		ON_ON	1	33	S8
		ON_OFF	1	31	S9
		ON_OFF	1	33	S10
		CLAMIR	3	31	S11
		CLAMIR	3	33	S12

As already mentioned, in the first part of the investigation two different materials were used as substrates, while in the second part the HSS 390 steel was chosen as a substrate. and different scanning strategies were adopted (see Table 3.4). According to the literature, the appropriate selection of the scanning strategies has an important effect on the final quality of the fabricated samples [5]–[8].

After the sample production of each condition, the metallographic preparation and the subsequent chemical etching were performed on specimens drawn from the fabricated samples according to the ASTM E3 standard, following the steps described in Table 3.5. All the specimens were observed by means of a Leica MZ6 (Leica, Wetzlar, Germany) stereomicroscope, a Leica DMi8A (Leica, Wetzlar, Germany) optical microscope and a further analyzed via a Zeiss EVO MA 15 (Carl Zeiss, Jena, Germany) scanning electron microscope equipped with an Oxford Xmax 50 (Oxford Instruments, Abingdon-on-Thames, UK) microprobe for energy-dispersive spectroscopy (SEM/EDS). The kind of phases in the WC-12Co depositions were identified also by a D8 Bruker X-ray diffractometer (XRD). Moreover, Vickers hardness was measured by performing linear profiles across the substrate and the layers under a 0.2 kg_f load (HV0.2) and 15 s loading time by a Future-Tech FM1e Vickers micro indenter (Future-Tech Corp., Kawasaki, Japan) in accordance with the UNI EN ISO 6507-1:2018 standard.

Table 3.5 Metallographic preparation used for WC-12Co specimens.

	Metallographic Preparation
Grinding	80, 120, 220, 400, 600, 800, 1000, 1200 and 2500 SiC papers, lubricated with water
Polishing	I. 6, 3 and 1 μm diamond paste using lubricant for diamond II. Al_2O_3 0.03 μm using water and delicate soap as lubricant
Etching	I. Murakami's (10 g $K_3Fe(CN)_6$, 10 g KOH or NaOH 100 mL water) for 5-10 s II. Nital 8% for 5-10 s

3.2 DISCUSSION OF THE WC-12CO DEPOSITIONS RESULTS: EFFECT OF THE DIFFERENT PARAMETERS AND SUBSTRATE MATERIAL

3.2.1 Macrostructural analysis

Specimens were prepared from samples S1-S6 and preliminary macroanalyses were performed in order to check the presence of possible discontinuities, macro-defects and porosity.

In the images reported in Figure 3.5 the presence of defects can be observed, including some cracking across the interface (see blue dot squares) as well as the presence of gas porosity in the transversal face of most of the samples. According to [9], the presence of cracking defect and its relationship with the process parameters depend on the way the layers are deposited, since different heat exchanges promote different solidification conditions and so inducing specific microstructural evolution, being highly important to minimize voids, pores and to improve the DED density parts [10],[11].

The deposition technique used for samples S1, S3, S5 is based on the partial remelting of the previous layer following the deposited direction as observed in Figure 3.5 while for samples S2, S4, S6 the laser moves along the first layer is finished for the further deposition of the following deposited layer. After the first deposition, the second layer remelts the previous material to reduce the porosity, nevertheless, as observed some pores can coalesce into larger ones trapped across the solidification line. Samples with three layers (S2, S4, S6) present a high quantity of pores mainly detected across the interlayer and the molten pools from the second deposited layer which is related to the high energy density, and the non-controlled heat input accumulation during the deposition of the materials.

Besides these features, the size and morphology of the powders as well as their initial porosity have a strong effect on the porosity formation during the processing as mentioned in the simulation performed by [12].

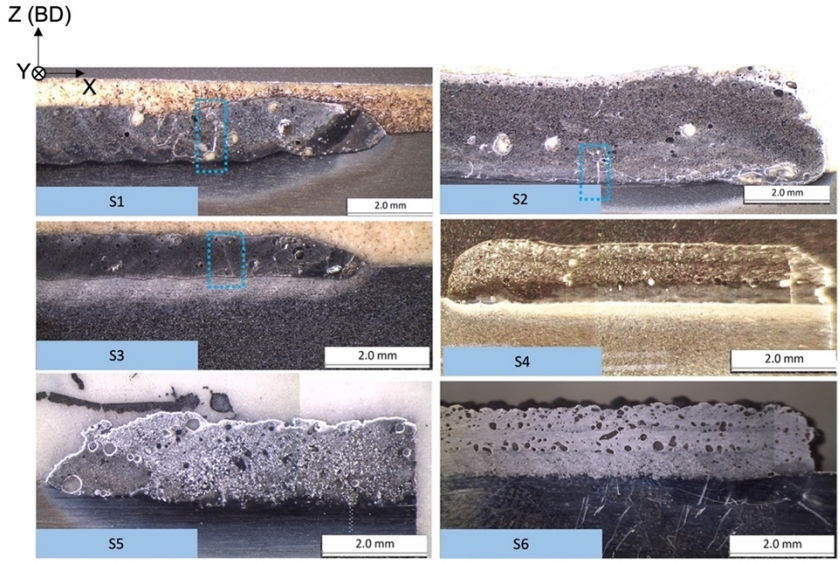

Figure 3.5 Representative macrographs of S1-S6 samples.

Cracking in most of the specimens are present whether across the layers or starting from the interface between the first layer and the substrate. Considering their path, these cracks are understandable to be a consequence of the remelting of the material and of the high quantity of stresses generated during the deposition process. In accordance with some studies [3], [13] these defects are related to thermal stresses suffered within the parts, inducing, as a consequence, residual stresses.

In [13], the residual stress mechanism is clearly explained. When the first layer is deposited internal stresses generate due to the solidification and subsequent cooling of the material, producing compression in the center of the deposition and high tensile stress on the surface. After the first layer solidifies, the second layer of powder is added and immediately melted by the laser beam, the bottom of the first layer contains stress, while the top part is exposed to the heat of the melted layer. The heat at top part expands, but it is limited by the cold bottom part of the first layer. These mixed mechanisms promote that the residual stresses become cracks if the material properties, scanning strategies, and features of the powder are not adequate.

Figure 3.6 shows the different defects found in sample S3 at higher magnifications. The presence of these cracks is related to the thermal expansion coefficient of the materials used as substrates. The thermal expansion coefficient of the carbon steel is higher than the one of the HSS steel (carbon steel thermal expansion coefficient is $12 \cdot 10^{-6}$ °C^{-1}, the one of the 390 HSS $10 \cdot 10^{-6}$ °C^{-1}, while the one of the W is $4 \cdot 10^{-6}$ °C^{-1}) being in the first case incompatible with the low thermal expansion of the WC. During the laser additive process, the high quantity of the heat accumulation needs to be dissipated in order to guarantee a good microstructural behavior of the deposition as well as a decrease of the cooling rates across the specimens.

When the carbon steel is used as a substrate, as in samples S3, S4, a lot of pores and cracks are formed along the interface between the substrate and the first deposited layer. While when the samples were deposited across the HSS substrate as in the case of S1, S2, S5, S6 a remarkable difference in the presence of the cracks is observed (see Figure 3.5).

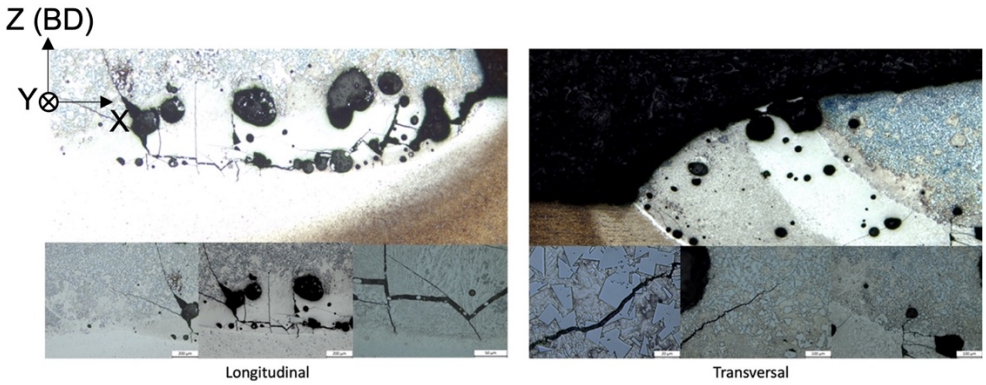

Figure 3.6 Defect found across sample S3.

In order to support the previous statements, a simple model of the residual thermal stresses induced in the materials due to the process is presented and developed in accordance with the study performed by [14]. According to [14], the residual stresses during the cladding process are promoted by the difference in the thermal expansion behavior of both parts. In Figure 3.7 is depicted a scheme used in the present model.

In Table 3.6 are collected the material's properties of the parts used for the samples' production considering Young's elastic modulus (E), Poisson rate (μ), and thermal expansion coefficient (α).

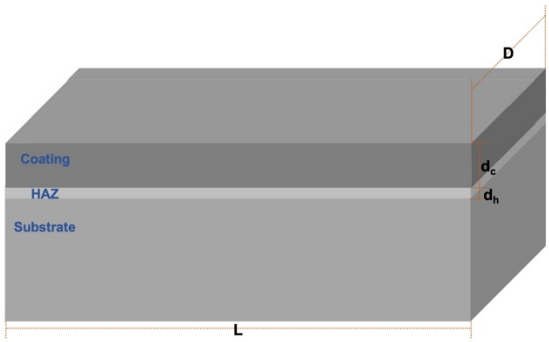

Figure 3.7 Scheme of the deposition assumed in the model.

Table 3.6 Material's properties used for the thermal stresses' calculation.

Coating (WC) properties		**Substrate properties**			
			C4 Steel		HSS 390
α_c	4,10e^{-6} °C $^{-1}$	α_{h1}	4,10e^{-6} °C $^{-1}$	α_{h2}	4,10e^{-6} °C $^{-1}$
μ_c	0,220	μ_{h1}	0,3	μ_{h2}	0,3
E_c	6,880e^{11} Pa	E_{h1}	1,967e^{11} Pa	E_{h2}	2,00e^{11} Pa
A	3,24			L	0,4 m
D	1 mm			d_c	0,8 mm

According to [14] the σ values for the C4 steel substrate and the WC coating were calculated as follows:

$$\sigma_H = -1{,}1778x10^{10}/(1 + 2{,}09P/\sqrt{V})$$

$$\sigma_c = 2{,}285x10^{10}/(1 - 0{,}47\sqrt{V}/P)$$

The σ values when the HSS 390 is used as a substrate and the WC as the coating were calculated as follows:

$$\sigma_H = -6{,}9041x10^{10}/(1 - 2{,}125P/\sqrt{V})$$

$$\sigma_c = 1{,}3187x10^{10}/(-1 - 0{,}47\sqrt{V}/P)$$

being V the scanning speed (mm/s) and P the laser power (W) employed as process parameters in each case.

In accordance with the previous expressions, it was confirmed that in the first case, the C4 steel suffers compressive stresses while the WC coating suffers tensile stresses. This justifies the high amount of cracks generated in the WC coating. Because of the lower thermal expansion coefficient of HSS 390 than C4 steel, the WC coating suffers compressive stresses.

3.2.2 Microstructural analysis

All the samples S1-S6 were subjected to microstructural analysis in three different zones, considering the interface, the center, and the top zones of the deposited layers. Figure 3.8 depicts a relevant evolution of the microstructure across the samples in accordance with the employed process parameters. As already described in the previous chapter, the laser energy density values for the different combinations of parameters were calculated in accordance with Equation 1.1, in order to evaluate the laser effect on the microstructure. The calculated laser energy densities and the corresponding process parameters are collected in Table 3.7.

Samples S1-S4 were produced using the same parameters (condition 23) but changing the substrate material and the number of the deposited layers. From the representative micrographs of these sample reported in Figure 3.8 it is clear that the size of the WC particles changes in accordance with the analyzed region, showing This changing is related to the different cooling rates experienced by the material in the different zones, being higher at the interface and lower at the top and inducing the refinement of WC carbide grains.

Conversely, samples S5-S6 were obtained with condition 33 and it can be observed that when the number of the deposited layers increases the microstructure becomes finer and with some un-melted zones. Moreover, it can observe the WC-rich dendritic carbide grains, identified with green stars across Figure 3.8.

Correlating the microstructural results with the laser density energies reported in Table 3.7, there is not so much difference among the values of the calculated laser energy density, however, it can be depicted that samples S5-S6 demonstrate more dissolution and regrowing of WC carbide with higher carbide formation happen than in S1-S4 where the lower energy density values were used. Even if the value of the laser energy as mentioned before is more or less the same across both samples, the effect of the quantity of the deposited layers is highly dominant on the microstructure refinement as well.

The previously mentioned statements related to the microstructure behavior are confirmed by the literature [15] [16] in which the study and control of the process parameters are fundamental to achieving high-quality deposited parts.

Table 3.7 Laser energy density and corresponding process parameters.

Sample	Power [W]	Scanning speed [mm/s]	PFR [g/min]	Laser Energy [J/mm^2]
Condition 23	1100	10	6,7	50
Condition 33	900	8	11,2	51.13
Condition 31	1300	8	11,2	73.86

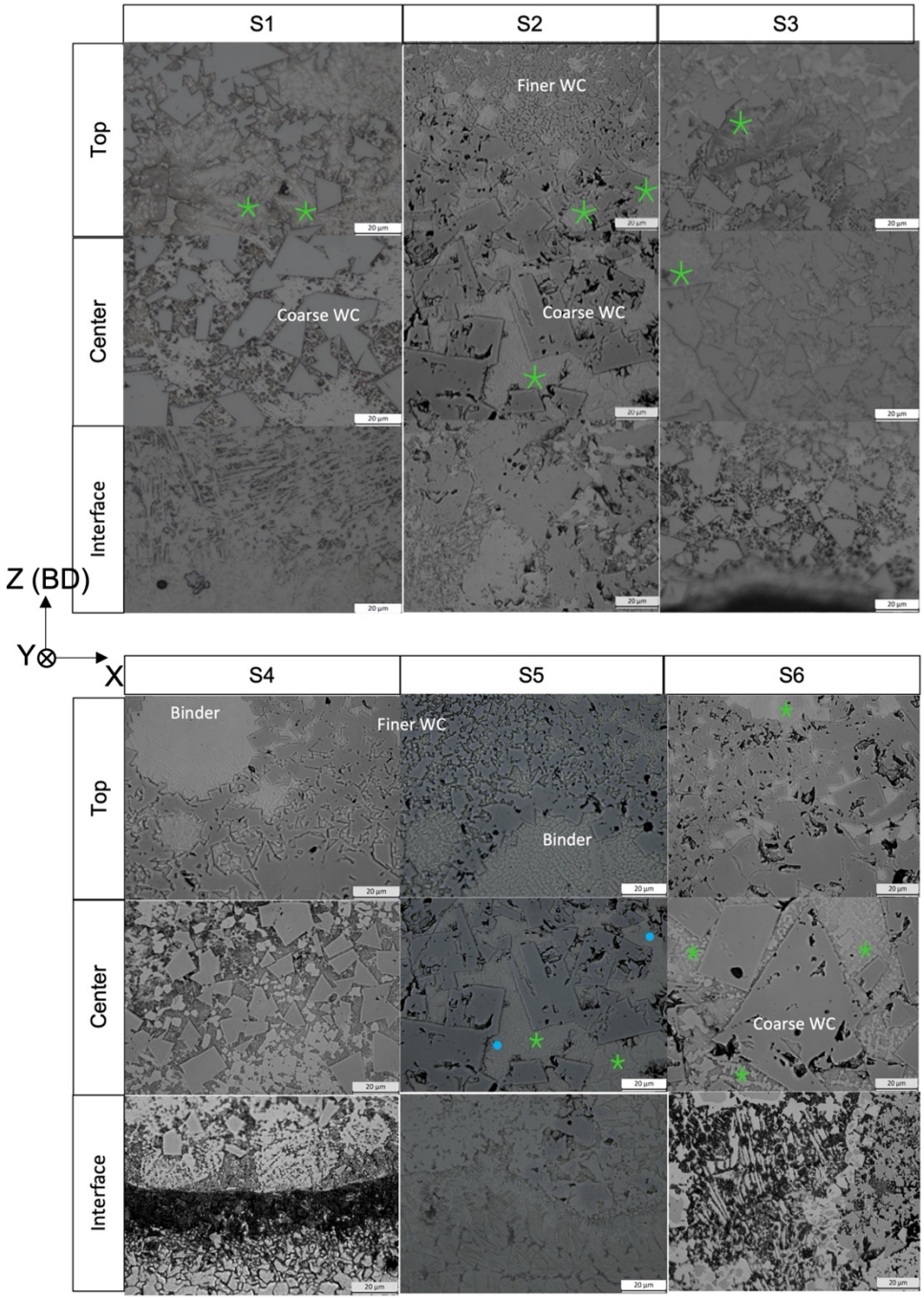

Figure 3.8 Microstructural evolution in samples S1-S6.

By means of the SEM analysis, the same zones of each sample were observed to analyze at higher magnification and at higher resolution the details of the microstructure. Comparing the micrographs of Figure 3.9 SEM micrographs of , in samples S3 and S4 the

low carbon substrate contributes to promote a more marked difference of the microstructure at the interface, conversely, in the case of the samples obtained by depositions over the HSS 390 steel a more uniform interface is observed because of a more interaction of the alloying elements between the two materials promotes the formation of carbides across this area.

The particle behavior generally across the samples show that these suffer a change in size, distribution, and presence in accordance with the analyzed zone of the specimen. This is highly related to the heat entrance and distribution of the non-uniform energy density during the process besides the extra rapid cooling rate across the samples. During the L-DED process, the high temperature of the laser usually exceeds the temperature of the Co melting point [1495 °C] and promoting a dissolution of the WC carbides, causing a C loss (decarburization). Hence, a transformation of the WC carbides to η-phase (usually Co_3W_3C Co_6W_6C) commonly happens, growing among the WC carbides and being produced by the interaction of Co with dissolved W and C [16].

As observed, generally the top part of the specimens shows a great quantity of finer re-precipitated polygonal WC carbides (see green stars in Figure 3.9) distributed into the Co matrix full of gray η-phase eutectic carbides in the shape of herringbone (see blue dots in Figure 3.9), whose formation is beneficial for enhancing the hardness but detrimental for the wear resistance properties of the final part. The same microstructure is shown in the central part of all the samples; nevertheless, the size of the WC carbides is higher, and the quantity of the herringbone carbides is less prominent than in the top. In the interface zone, besides the fact of the barrier mentioned before, a continuous presence of herringbone carbides can be observed as a consequence of the interaction between the elements of the substrate and the deposited layer.

To corroborate the presence of the different phases/carbides, EDS analyses were performed on the samples. In Figure 3.10 are collected the micrographs with evidence of the punctual analyses and of the results obtained from the EDS spectra. WC carbides, with their polygonal morphology and different size and distribution in the different zones, are characterized by a high quantity of W and C, with the Co arising from the arising matrix. In the case of the herringbone carbides (η-phase), it was found that Fe, W, Co, and C contents are highly present, characteristic of these particles, with the morphology of eutectic herringbone dendrites that changes as the zone advances from the substrate-powder interface to the top part of the sample.

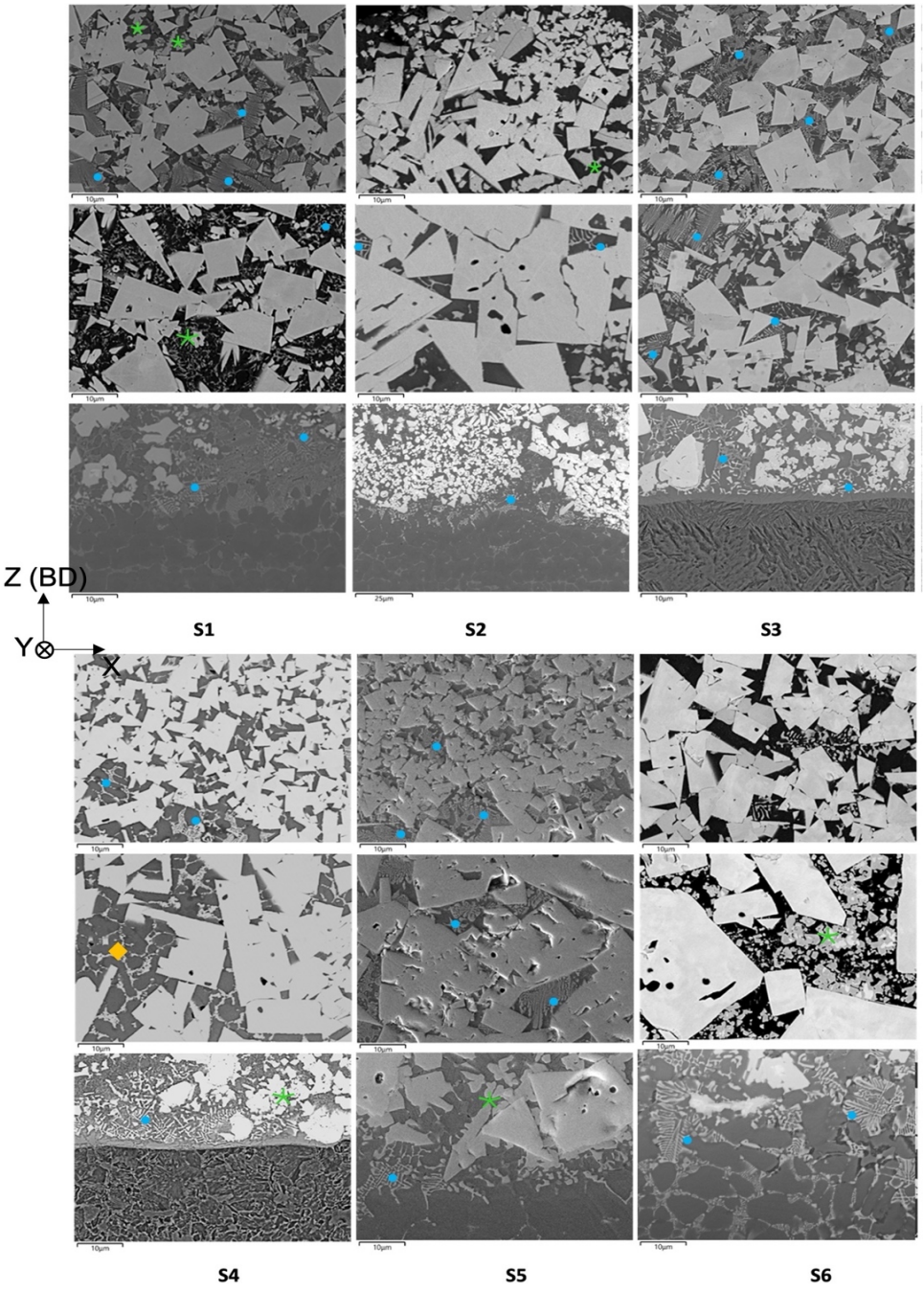

Figure 3.9 SEM micrographs of the samples S1-S6.

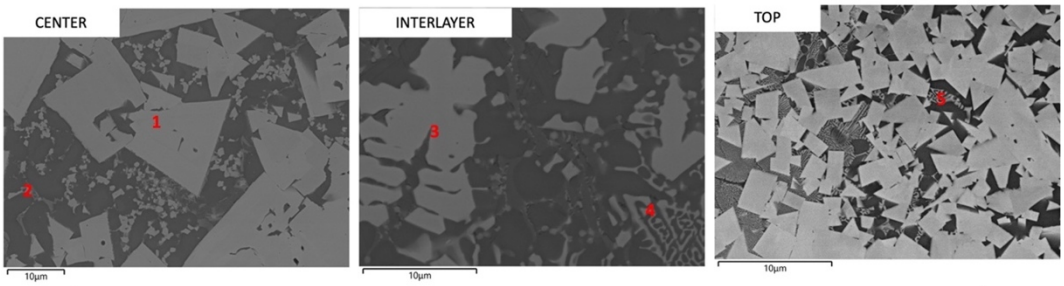

Particle	Fe	W	Mo	Cr	Co	V	Mn	C	Particle identification
1	4,4	78,6	-	0,5	5,1	-	0,1	11,4	WC carbide
2	16,5	43,6	0,9	2,9	23,9	0,7	0,2	11,3	W_2C carbide
3	55,4	20,2	3,2	5,6	4,8	1,4	0,4	9,0	Fe-rich WC carbide
5	61,3	18,3	1,9	2,5	5,2	0,8	0,3	9,6	η-phase M_3W_3C type (M=Fe)
6	4,3	44,7	-	0,9	35	-	0,1	14,9	η-phase $M_{12}WC$ type (M=Co)

Figure 3.10 SEM/EDS punctual analyses performed across S3 sample.

3.2.3 Hardness behavior

Vickers profiles were performed with a 0.2 kg_f load across the length of each sample (see Figure 3.11), from the substrate towards the deposited layers.

As expected, a marked increase in hardness was observed in the transition from the substrates to the deposited layers. The scatter of data in the WC-12Co hard facing material is very high but due to the presence of a non-uniform matrix and to the distribution of WC grain carbides. The highest hardness values were found in sample S6, in agreement with the finer distribution of WC carbides and the higher amount of herringbone particles.

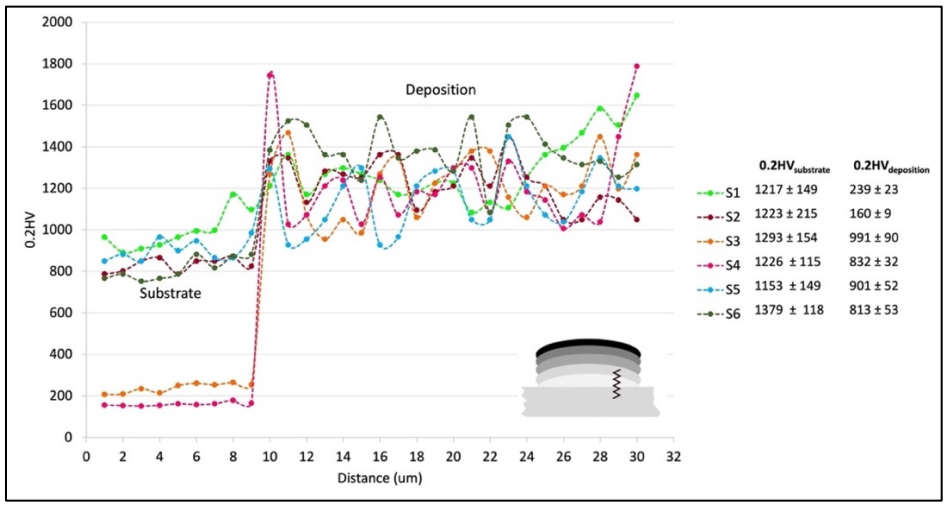

Figure 3.11 Representative hardness profiles performed in samples S1-S6.

3.3 DISCUSSION OF THE WC-12CO DEPOSITED RESULTS: EFFECT OF SCANNING STRATEGY VARIATION

3.3.1 Macrostructural analysis

The experimental results obtained analyzing samples S1-S6 suggested that the use of a compatible thermal expansion material as a substrate during the depositions fewer discontinuities such as residual stresses that promote a high quantity of cracks are present. In the present stage, the HSS 390 steel was used to deposit the different layers with other process parameters. Since it was observed previously that even if the thermal expansion of both employed materials as substrate wasn't different, the results obtained in terms of defects, microstructure distribution across the interface and its behavior across the deposition is favorable when this material is used.

In particular, samples S7-S12 already mentioned in Table 3.4were fabricated using conditions 31 and 33 but according to different scanning strategies.

In Figure 3.12a transversal section of each sample is shown as a collage of several micrographs. All the samples, independently on the conditions 31 and 33, i.e., with both high and low laser input, show a high quantity of defects including spherical porosity, cracking, and in some cases lack of fusion. The existence of these defects could be a consequence of many reasons. As mentioned in [3], [9] the porosity is identified as of two different types; irregular shape pores, which are mainly related to shrinkage and lack of fusion occurring the during the material processing, or spherical pores which are related to gas entrapment (mainly moisture in the powder and keyhole). Moreover, it is important to mention that these cemented carbide materials are naturally prone to crack formation due to the high quantity of stresses and shrinkage that develop during the process.

Besides the porosity formed during the solidification along the WC grains and the dendrites of herringbone carbides, a remelting layering can be observed across the samples, indicating the direction of the different depositions which are also related to the change in size and distribution of the dissolved and non-re-precipitated WC grain zones.

As concerns the effect of process parameters, samples S7 and S8 which were produced with the same ON_ON scanning strategy but with conditions 31 and 33, respectively, show a different microstructural evolution. Even if sample S7, which was deposited using a higher energy density, has a better and uniform distribution of the WC particles, it is affected by high quantity of cracks. Conversely, sample S8 shows less cracks and porosity across the layers but minor homogeneity of the microstructure due to the low VED value which is in this case is lower at the lower laser power employed. As mentioned in section 1.1.2, this factor is useful to determine the microstructural behavior of the depositions because it is a measure of the volumetric density of the input energy during the process.

Same considerations can be done when samples S9 and S10 are compared. These samples were deposited with the 31 and 33 process conditions, respectively, but with the same ON_OFF scanning strategy. This scanning strategy generates a higher quantity of defects but a better microstructural distribution at the lower energy density. In the case of samples S11 and S12 with CLAMIR camera control and multilayer (three deposited layers), it is observed that also in the case the effect of the laser is important for the microstructure homogeneity across the whole deposited part, as in the case of S12. Regardless, their high porosity presence.

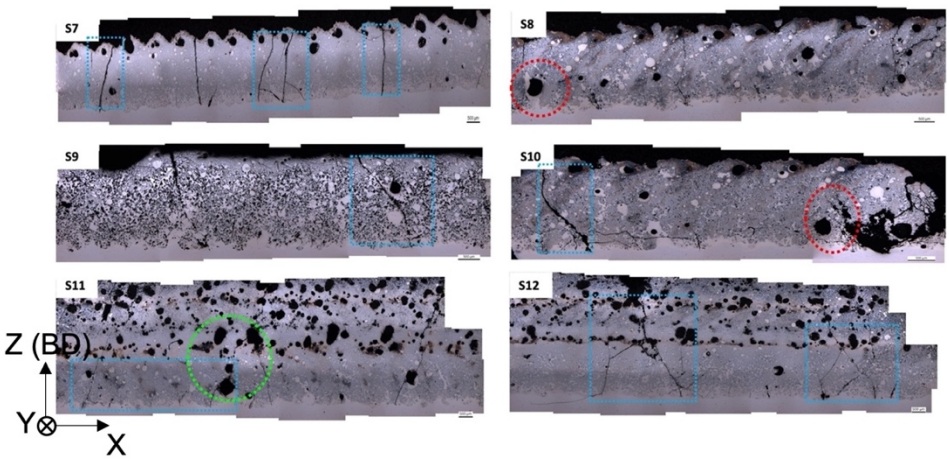

Figure 3.12 Optical reconstructed micrographs that depicts a wide panorama of samples S7-S12.

3.3.2 Microstructural analysis

All the specimens were analyzed by optical microscopy, focusing the attention on the following zones of the deposited material: the interface between the substrate and the WC-12Co, the center, and the top. The collections of micrographs corresponding to the different zones, for all samples S7-S12, are reported in Figure 3.13 and in Figure 3.14.

The microstructure is quite different in the samples, so according to process parameters and scanning strategies, and with respect to the abovementioned zones. In the interface zone the interaction with the substrate results in small size WC grains, while in the next two zones (center and top) distribution and size of WC grains changes, being coarser in the center with some kind of circled areas named residual WC-12Co regions (see orange dotted circles marked in each Figure 3.13 and Figure 3.14). Across Figure 3.15 the representative microstructure (green diamond of Figure 3.14) of these residual regions is depicted. While in the top, a mixture of fine and coarse particles can be observed.

Correlating the process parameters with the microstructural behavior, samples fabricated with condition 33 show a more refine microstructure than with condition 31. As well as in Figure 3.12, in terms of the scanning strategy, the laser power value has an important effect on the WC grains distribution, since more uniform distributed refined particles are observed since the behavior of the first layer that improves in the further deposited layers.

When the ON_OFF strategy is used, the dissolution and re-precipitating of the microstructure are less due to the loss of heat during the shutdown of the laser, an aspect that was not observed in the samples fabricated with the ON_ON strategy. In the case of CLAMIR samples, as observed in Figure 3.14 the different zones of each layer show different distribution and size of the WC particles. Due to the particles reaction to the heat accumulation provided by the laser, the finer microstructure is observed at the top with fewer herringbone carbides, however as depicted S12 show the finest with better homogenization among them. In this sense, the control of the CLAMIR camera has demonstrated better results that are coherent with the laser energy density values adopted during the process (see Table 3.7 Laser energy density and corresponding process parameters.

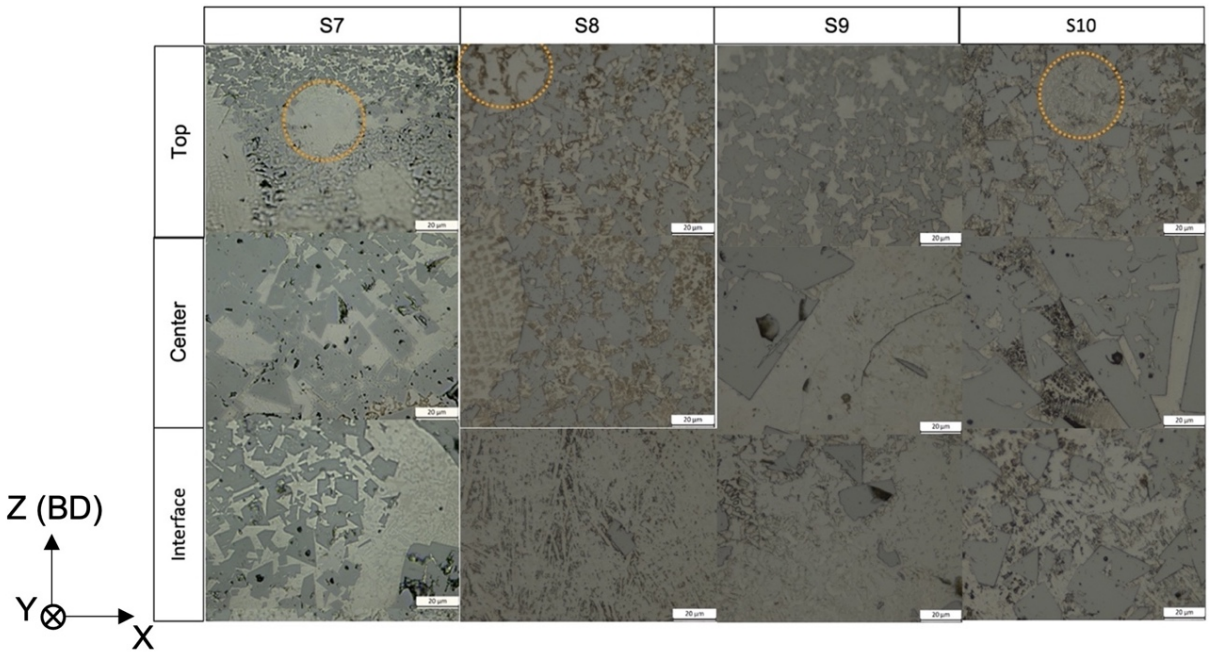

Figure 3.13 Microstructural evolution of samples S7-S10.

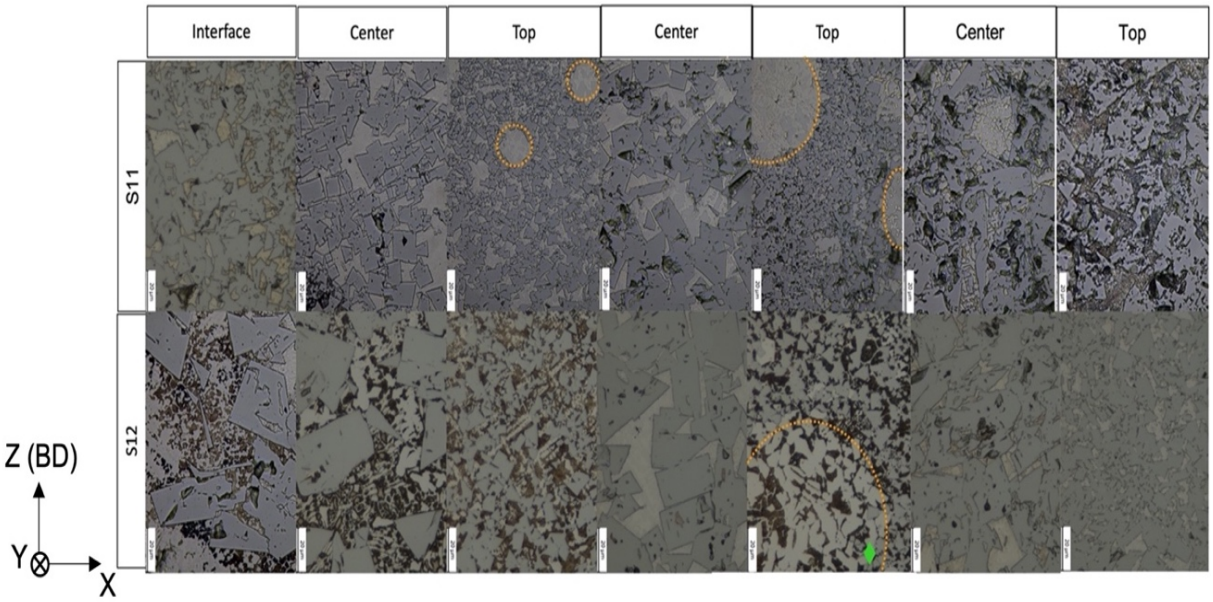

Figure 3.14 Microstructural evolution of sample S11-S12.

Figure 3.15 Microstructure present within residual WC regions of sample S12.

By means of the SEM analysis, the same zones of each sample were observed to analyze at higher magnification and at higher resolution the details of the microstructure (see Figure 3.16). The microstructure of WC-Co is inhomogeneous since the molten pool has reached enough temperature to melt the WC and evaporate the Co due to the non-uniform distribution of the energy density across the samples.

The high cooling gradient generated during solidification produced coarse WC grains layered structure alternating with fine grains along the upper part of each molt pool, i.e., as shown in Figure 3.16 indicated with the green dotted lines. As observed, most of all the samples show this behavior, however the top part of the S12 show a more uniform distribution.

When the energy density is higher, as in the case of samples S7, S9, and S11, brittle structures with small WC grains and low Co content can be observed (red dots across Figure 3.16). Conversely, when low energy densities are used, tough structures with large WC grains and high Co content can be detected across Figure 3.16 as in yellow dots leading to a more uniform structure and less η- phase formation.

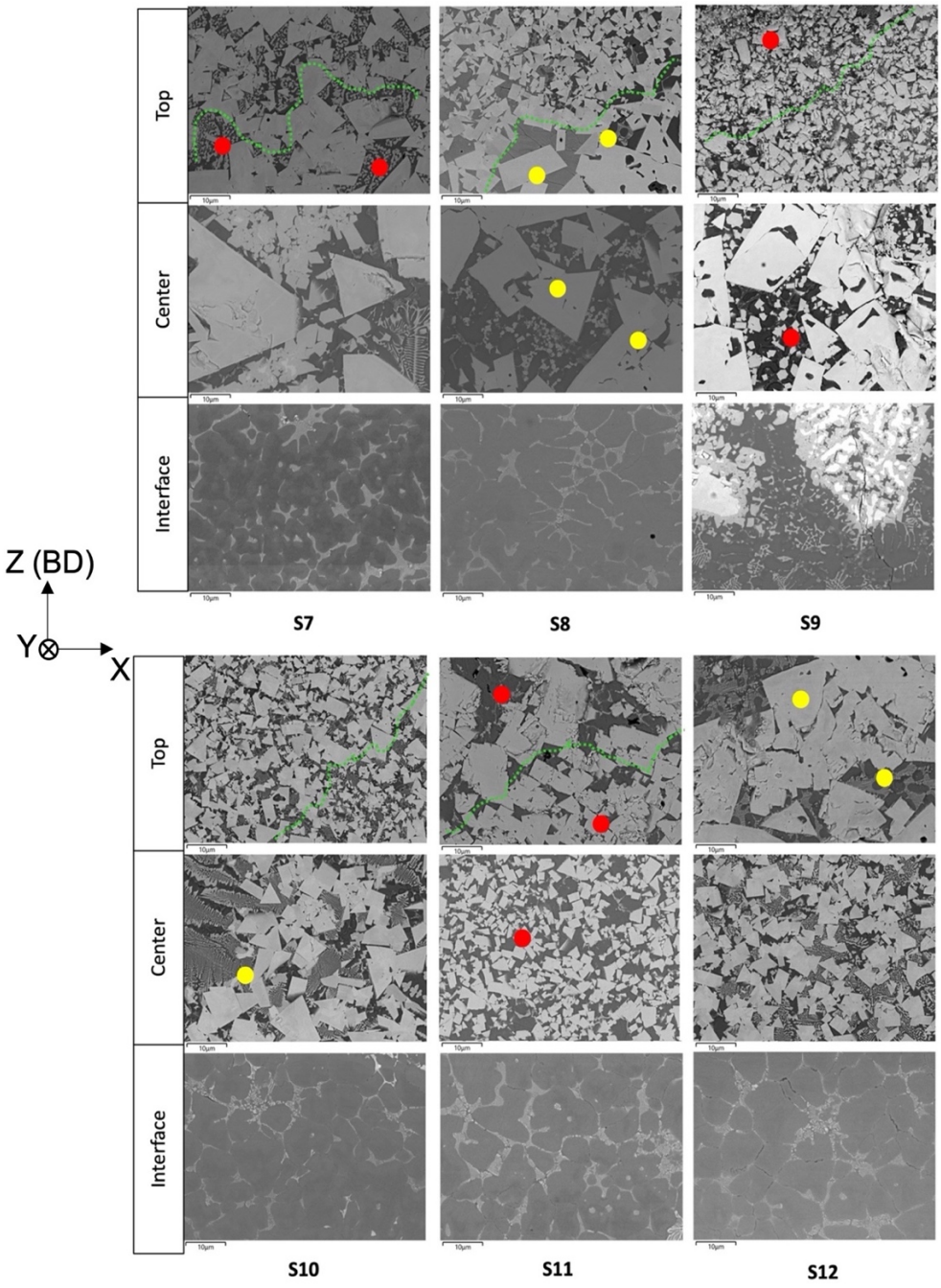

Figure 3.16 SEM micrographs of samples S7-S12

Samples S11 and S12 experienced completely different energy densities, but as mentioned before not only the laser energy is a key factor. According to the literature [17]–[20] when the VED factor that can be calculated with Equation 1.2 is higher, the amount of the η-phase carbides across the samples is higher too. Besides that, the presence of this phase is good for the increase of the hardness properties, but unfortunately, it is detrimental for the wear resistance since they promote a brittleness material, so low content of η-phase is the best option. In light of this, process parameters and scanning strategies used for fabricating sample S12 could be selected as the best choice majorly in terms of microstructural behavior and its effects across the hardness behavior.

In Table 3.8 the calculated values of VED are collected for samples S7-S12. When the power parameter increases the VED value is higher and, in particular, if increases the VED then also increases the presence of the M_3W_3C (M=Fe or Co) carbides as mentioned in [21].

Table 3.8 VED values for samples S7-S12.

Sample condition	Process parameters	VED (Volumetric energy density) [J/mm^3]
S7 S9 S11	Power: 1300 W Scanning speed: 8 mm/s PFR: 2.5 rpm 0.8 mm layer thickness 1 mm Hatch distance	203.1
S8 S10 S12	Power: 900 W Scanning speed: 8 mm/s PFR: 2.5 rpm 0.8 mm layer thickness 1 mm Hatch distance	140.6

On the basis of these considerations, sample S12 was selected to be deeply analyzed by SEM/EDS. The micrographs of Figure 3.17 show an enlargement of WC grains up to more than 10 μm surrounded by dark regions with high amounts of cobalt and netlike bonded structures of carbides and η- phase. The WC grain are coarse at the top, while appears finer at the center are. In the interface area the dark regions are larger than the WC grains.

Via EDS analysis some particles were analyzed, and their compositions (wt. %) confirmed that the irregular particles labelled with (1) are rich in W, C, and Fe since are produced at the interface with the substrate, while the herringbone netlike one (2) and (4) are richer in Fe, Co and W, characteristics of the precipitated carbides across the sample. At the center and at the top, the light grey particle labelled with (3) is richer in W and Co, so they are polygonal re-precipitated particles across the Co matrix; in this sense, particle labelled with (5) at the top of the sample is a fully recovered WC grain which was formed during the solidification of the deposited material.

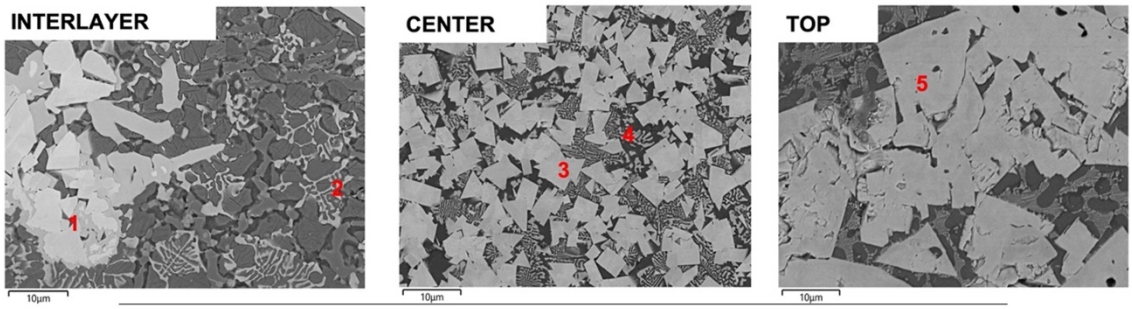

Particle	Fe	W	Mo	Cr	Co	V	Mn	C	Particle identification
1	18,2	65,8	1,6	1,3	1,3	1,6	0,1	11,1	WC carbide
2	55,9	25	3,3	2,9	4,0	1,2	3,3	7,3	η-phase M_3W_3C type (M=Fe)
3	13,1	54,5	0,1	0,8	22,1	0,2	0,1	9,1	WC refined carbide
5	16	44,9	0,1	1	26,7	0,2	0,1	11,1	η-phase $M_{12}WC$ type (M=Co)
6	0,3	78,7	-	0,1	7,4	-	0,1	13,4	WC carbide

Figure 3.17 SEM/EDS analysis of sample S12.

Besides the previous microstructural investigations, EDS linear analyses were performed on the transversal section of sample S12, in order to determine the dilution of the main elements. In Figure 3.18a is displayed the SEM image of the sample where the two EDS linear maps are depicted; as can be noted, the two lines have a certain degree of overlap that can be also detected through the comparison of the spectra reported in Figure 3.18 b. The quantity of W and Co is very stable across the three layers; a decrease in their content can be observed when the analysis crosses a pore. V, Fe, and Cr are higher across the first

layer. The same trend was also detected in the other samples; as mentioned before, the presence of the Cr, V, and Fe in the first layer is higher due to the dilution effect with the substrate, while starting from the middle of the second layer their dilution ends. These EDS analyses confirmed the wide heat effect produced by the laser.

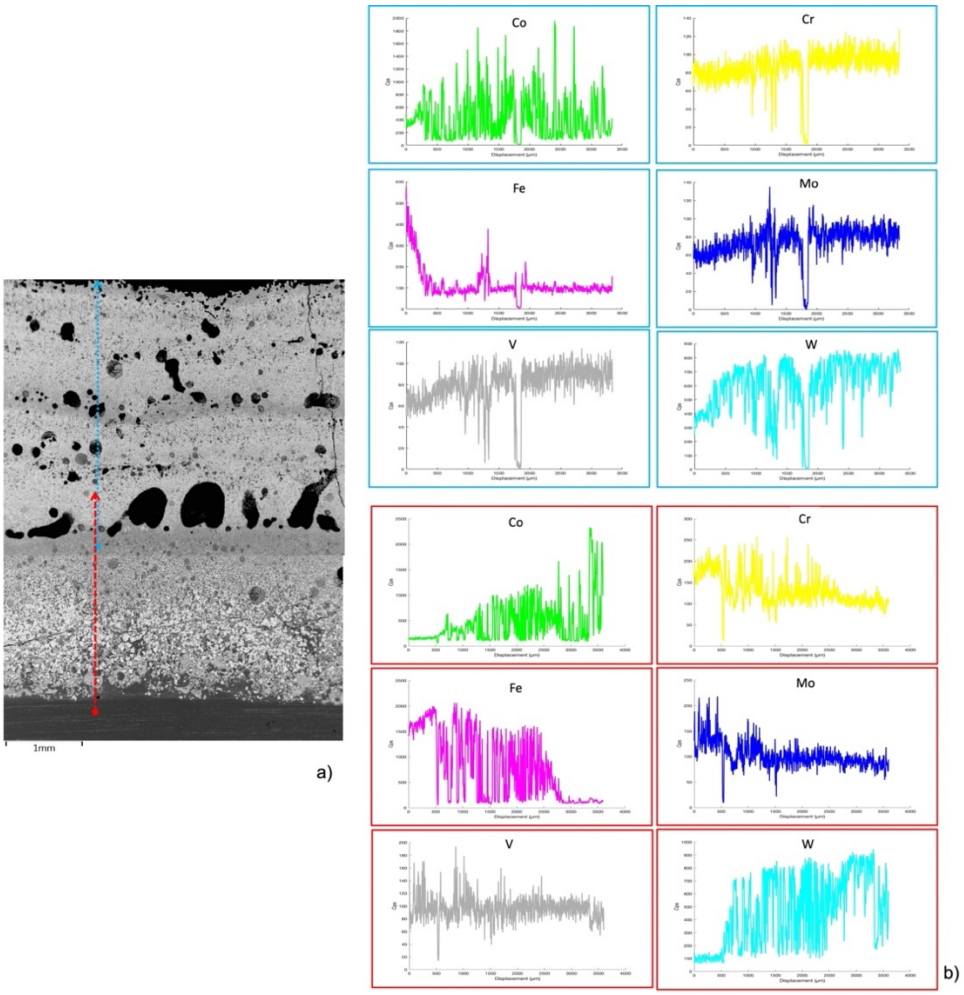

Figure 3.18 EDS line analysis of sample 12.

To corroborate both the previous EDS analysis and the VED statement, samples S11 and S12 were subjected to an XRD analysis (see Figure 3.19). The peaks of the η-carbides as well as of the secondary W_2C carbides are present across both samples, even though in S12 they are of lower intensity than in S11, in agreement the VED values reported in Table 3.8.

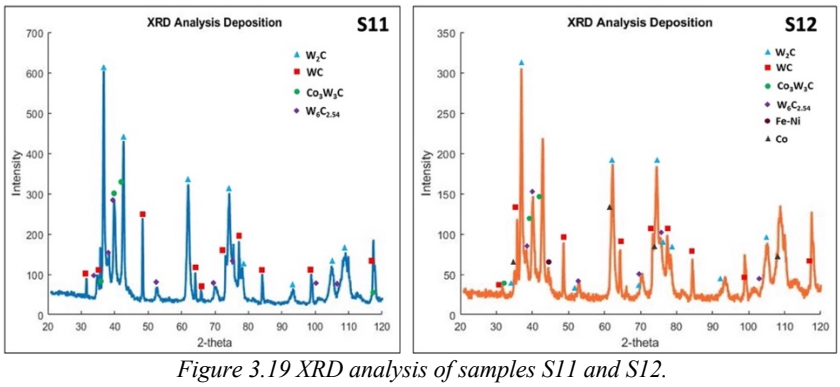

Figure 3.19 XRD analysis of samples S11 and S12.

3.3.3 Hardness analysis

Microhardness Vickers profiles were performed across each specimen with a 0.2 kg_f load Figure 3.20and in Figure 3.20 the representative profiles are plotted. The higher hardness values are found in samples S11-S12, the ones performed with the laser control camera scanning deposition. These results are in accordance with the microstructural analysis discussed in the previous section.

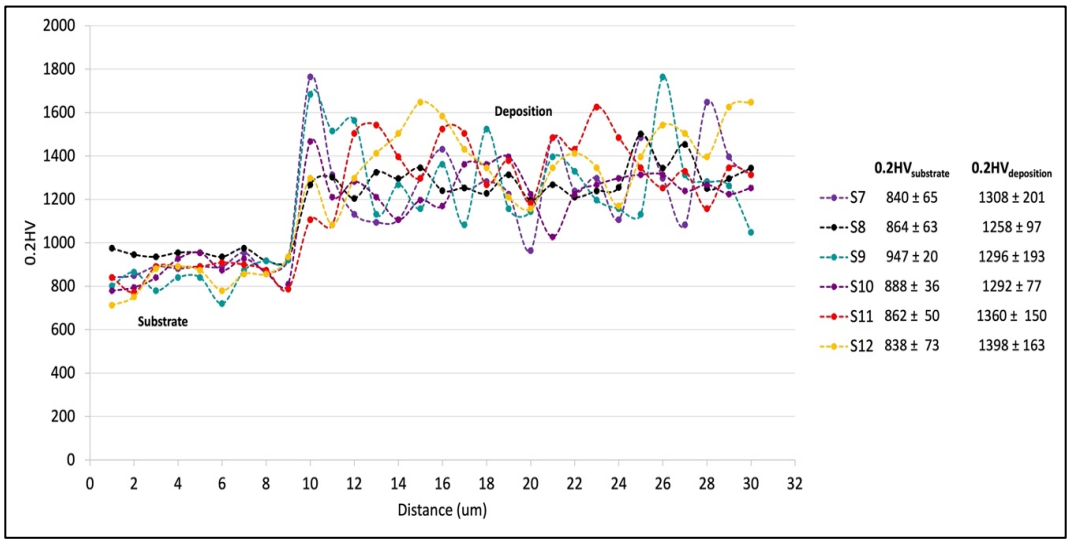

Figure 3.20 Vickers profiles performed across samples S7-S12.

As a complementary analysis, in Figure 3.21 it is depicted a specific particle micro indentation across sample S12 taken just as shown in the reconstruction of the macrographs of Figure 3.22. As observed, there is a strong variation of the microhardness value in accordance with the indented zone, as an example when the indentations were randomly taken as shown across the plot in the indentation number five and nine (see the green and orange dots respectively across Figure 3.21 and Figure 3.22) demonstrate higher values when the WC particles are present regardless its size or refinement, however across the top part which is composed by coarse re-precipitated agglomeration of WC carbides (blue dot in same figures) the hardness reach the higher values.

However, the hardness value changed drastically when the areas free of carbides are surrounded by polygonal WC particles are analyzed because is only the Co matrix with the initial carbide's formation, as observed in the highlighted blue zone, marked by a red dot across Figure 3.22, and marked by purple and white dots across the area of same figure and across plot of Figure 3.21. In accordance with the literature this hardness behavior follows the Hall-Petch relationship in which the finer grains are the hardest.

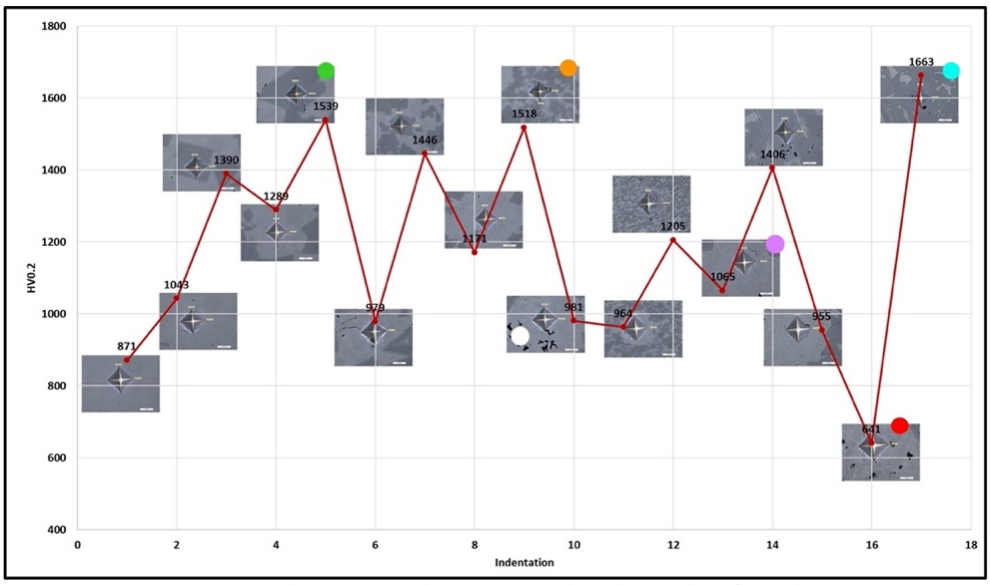

Figure 3.21 Vickers micro indentations in selected particles of sample S12.

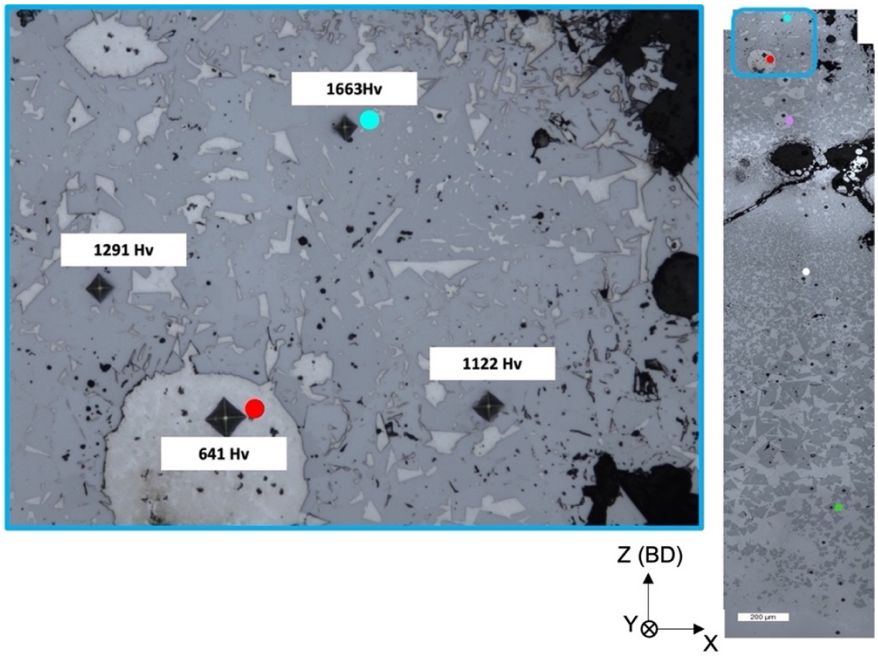

Figure 3.22 Microhardness indentations across specific zones of the sample S12

3.3.4 CONCLUDING REMARKS

WC-12Co powders were deposited via the L-DED process in two different substrates, i.e., a low carbon (C4) steel and an HSS 390 steel. Different process parameters were adopted for performing the depositions according to selected combinations of laser power, powder feed rate, scanning speed, and scanning strategies. The experimental approach was divided into two main parts. In the first one the laser power was considered as a variable, while the other parameters were maintained fixed in to test the effects of laser power and of the substrate. In the second part the effects of the scanning strategies and the laser power were investigated.

Based on the results obtained in the first part, the effect of the substrate material on the evolution of the microstructure is of high importance even though all the fabricated samples showed a high quantity of defects such as gas porosity and cracks in particular across the interface. The samples deposited on the carbon steel substrate showed a high quantity of cracking that spread from the interface to the end of the layer deposition, so extremely dangerous for the integrity of the sample. The presence of these cracks can be ascribed to the thermal expansion coefficient of the carbon steel is higher than the one of the HSS steel, being the first incompatible with the low thermal expansion of the WC. The difference between the thermal expansion coefficient of the carbon steel substrate and of the WC-12Co is responsible for the material cracking also considering the high cooling rate during the deposition process. The presence of crack undoubtedly contributes to the decrease of the mechanical properties and in particular of the toughness. Conversely, the depositions performed on the HSS 390 plates behaved better in terms of the presence of cracks, but with no advantages as concerns porosity. Even in samples S2, S4 and S6, where three subsequent layers were deposited, porosity did not decrease; sample S6 was the worst the among all the six different samples.

As a result of the microstructural investigations, the energy density was recognized to be an important combined parameter with a relationship with the expected microstructure. Especially in the case of samples S1-S4 it was found that when the laser energy density is higher, the microstructure is finer. While the other two samples S5-S6 promoted with high-speed steel substrate and slightly lower laser density demonstrated that finer microstructure is induced across the samples. Nevertheless, some unmelted WC zones were detected which are available zones for the further formation of the hardenable carbides.

In general, the microstructural investigation performed on the samples by optical microscopy and scanning electron microscopy (SEM/EDS) confirmed the presence of a Co matrix full of gray herringbone dendrites η-phase carbides and a high quantity of polygonal WC grains of different sizes. The hardness results were in good agreement with the microstructural findings since the higher hardness values were found for samples S5-S6 (1153-1350 HV0.2); these samples were performed with low density energy values and deposited upon an HSS substrate.

In the second part, considering the main results of the first part, more L-DED hard facing depositions were performed considering the conditions of parameters 31 and 33 but adopting different scanning strategies. The results showed that the different scanning strategies selected have marked effects in terms of the defects, microstructure evolution, and hardness behavior.

3.4 REFERENCES

[1] M. Mariani, D. Mariani, de Gaudenzi Gian pPietro, and Lecis Nora, “Effect of printing parameters on sintered WC-Co components by binder jetting,” *European Journal of Materials*, vol. 2, no. 1, pp. 365–380, 2022.

[2] S. Fries *et al.*, “Laser-Based Additive Manufacturing of WC–Co with High-Temperature Powder Bed Preheating,” *Steel Res Int*, vol. 91, no. 3, Mar. 2020, doi: 10.1002/srin.201900511.

[3] M. Liu, A. Kumar, S. Bukkapatnam, and M. Kuttolamadom, “A Review of the anomalies in Directed Energy Deposition (DED) processes and potential solutions.”

[4] A. Saboori, D. Gallo, S. Biamino, P. Fino, and M. Lombardi, “An overview of additive manufacturing of titanium components by directed energy deposition: Microstructure and mechanical properties,” *Applied Sciences (Switzerland)*, vol. 7, no. 9. MDPI AG, Aug. 28, 2017. doi: 10.3390/app7090883.

[5] K. S. B. Ribeiro, F. E. Mariani, and R. T. Coelho, “A Study of Different Deposition Strategies in Direct Energy Deposition (DED) Processes,” *Procedia Manuf*, vol. 48, pp. 663–670, 2020, doi: 10.1016/j.promfg.2020.05.158.

[6] H. Ali, H. Ghadbeigi, and K. Mumtaz, “Effect of scanning strategies on residual stress and mechanical properties of Selective Laser Melted Ti6Al4V,” *Materials Science and Engineering A*, vol. 712, pp. 175–187, Jan. 2018, doi: 10.1016/j.msea.2017.11.103.

[7] M. O. Gushchina *et al.*, “Effect of Scanning Strategy on Mechanical Properties of Ti-6Al-4V Alloy Manufactured by Laser Direct Energy Deposition,” *J Mater Eng Perform*, vol. 31, no. 4, pp. 2783–2791, Apr. 2022, doi: 10.1007/s11665-021-06407-7.

[8] W.-W. Liu *et al.*, “Review on scanning pattern evaluation in laser-based additive manufacturing,” *Optical Engineering*, vol. 60, no. 7, 2021, doi: 10.1117/1.

[9] T. Zhao *et al.*, “Some factors affecting porosity in directed energy deposition of AlMgScZr-alloys,” *Opt Laser Technol*, vol. 143, Nov. 2021, doi: 10.1016/j.optlastec.2021.107337.

[10] K. S. B. Ribeiro, F. E. Mariani, and R. T. Coelho, “A Study of Different Deposition Strategies in Direct Energy Deposition (DED) Processes,” *Procedia Manuf*, vol. 48, pp. 663–670, 2020, doi: 10.1016/j.promfg.2020.05.158.

[11] B. AlMangour, D. Grzesiak, and J. M. Yang, “Scanning strategies for texture and anisotropy tailoring during selective laser melting of TiC/316L stainless steel nanocomposites,” *J Alloys Compd*, vol. 728, pp. 424–435, 2017, doi: 10.1016/j.jallcom.2017.08.022.

[12] T. J. Jeon, T. W. Hwang, H. J. Yun, C. J. VanTyne, and Y. H. Moon, “Control of porosity in parts produced by a direct laser melting process,” *Applied Sciences (Switzerland)*, vol. 8, no. 12, Dec. 2018, doi: 10.3390/app8122573.

[13] Y. Chen, X. Peng, L. Kong, G. Dong, A. Remani, and R. Leach, “Defect inspection technologies for additive manufacturing,” *International Journal of Extreme Manufacturing*, vol. 3, no. 2. IOP Publishing Ltd, Apr. 01, 2021. doi: 10.1088/2631-7990/abe0d0.

[14] X. Zhou, H. Hu, and Yu Jiahong, “Residual thermal stresses of laser cladding of intermetallic ceramic composite coatings,” *Journal of University of Sciences and Technology*, vol. 4, no. 2, pp. 1–3, 1997.

[15] A. Angelastro, S. L. Campanelli, A. D. Ludovico, and S. Ferrara, “Direct laser metal deposition of tungsten carbide-cobalt-chrome (wc/co/cr) powder,” in *30th International Congress on Applications of Lasers and Electro-Optics, ICALEO 2011*, Laser Institute of America, 2011, pp. 1294–1300. doi: 10.2351/1.5062219.

[16] M. HU, J. cheng TANG, X. gui CHEN, N. YE, X. yue ZHAO, and M. miao XU, “Microstructure and properties of WC-12Co composite coatings prepared by laser cladding,” *Transactions of Nonferrous Metals Society of China (English Edition)*, vol. 30, no. 4, pp. 1017–1030, Apr. 2020, doi: 10.1016/S1003-6326(20)65273-6.

[17] H. Y. Chia, J. Wu, X. Wang, and W. Yan, “Process parameter optimization of metal additive manufacturing: a review and outlook,” *Journal of Materials Informatics*, vol. 2, no. 3, p. 16, 2022, doi: 10.20517/jmi.2022.18.

[18] K. Moussaoui *et al.*, “Effects of Selective Laser Melting additive manufacturing parameters of Inconel 718 on porosity, microstructure and mechanical properties,” *Materials Science and Engineering: A*, vol. 735, pp. 182–190, 2018, doi: 10.1016/j.msea.2018.08.037ï.

[19] A. Khaimovich, A. Balyakin, M. Oleynik, A. Meshkov, and V. Smelov, “Optimization of Process Parameters for Powder Bed Fusion Additive Manufacturing Using a Linear Programming Method: A Conceptual Framework,” *Metals (Basel)*, vol. 12, no. 11, p. 1976, Nov. 2022, doi: 10.3390/met12111976.

[20] P. Ferro, R. Meneghello, G. Savio, and F. Berto, “A modified volumetric energy density-based approach for porosity assessment in additive manufacturing process design”, doi: 10.1007/s00170-020-05949-9/Published.

[21] T. Schwanekamp and M. Reuber, “Additive Manufacturing of application optimized tungsten carbide precision tools,” in *Proceedings of 6th International Conference on Additive Technologies*, 2016, pp. 100–114. [Online]. Available: https://www.researchgate.net/publication/319965031

CHAPTER 4 CONCLUSIONS AND FUTURE WORK

The present Ph.D. thesis covered the investigations performed on hard facing depositions fabricated Laser-based Direct Energy Deposition (L-DED) in 17-4 PH stainless steel and WC-12Co cermet. The doctoral activities were carried out at the Department of Engineering of the University of Ferrara, but in collaboration with the Department of Industrial Engineering of the University of Bologna within a BIREX (project AN-MEC - L'Additive Manufacturing nella filiera produttiva dell'industria meccanica: dallo sviluppo del processo alla definizione del business model per la produzione di nuovi componenti", CUP C41J20000030008). The depositions were fabricated employing different process conditions studying the effects of laser power, scanning speed, scanning strategy, powder feed rate, and substrate materials. The investigations dealt with several aspects of the quality of the depositions, from the geometrical features, e.g., dilution, to microstructural and mechanical properties. Moreover, different specifically designed post-fabrication heat treatment routes were applied to the 17-4 PH single-track depositions to analyze their effects on their final microstructural and the performance of the material. From the obtained results, correlations between process parameters and material properties were established in order to suggest the most feasible combinations of parameters for future industrial applications. Considering the lack of knowledge in the literature relevant to the L-DED processing of 17-4 PH and WC-12Co materials, the writer hopes that this doctoral could be of any reference for further investigations.

This final section aims at drawing the most important concluding remarks of each topic and suggesting future developments.

4.1 17-4 PH L-DED DEPOSITIONS

Laser-based direct energy single-track depositions of 17-4 PH stainless steels were fabricated on AISI 316L stainless steel plates employing different process parameters in terms of laser power, scanning speed and strategy, and powder feed rate. The analysis of the geometrical features, together with macro and microstructural analysis performed on preliminary samples showed the presence of different levels of defects such as gas porosity, detachments, lack of fusion; nevertheless, from this initial screening, the most four suitable combinations of process parameters were adopted to perform other samples. According to the different solidification conditions due to the cooling rates and the thermal gradients induced by the process parameters, a microstructure composed of a martensitic matrix and different quantities of δ-ferrite across the interface zone were found in the fabricated samples.

After a deep geometrical, and macro and microstructural analysis of the new samples, the most feasible process condition (S4) was selected. The depositions fabricated according to its corresponding parameters allowed better dilution, less quantity of porosity, as well as a homogenized martensitic microstructure with lower ferrite contents. The microstructural results were also supported by the highest hardness values (396 ± 46 HV0.05). A correlation between the experimental results and both the laser power and the laser energy density was identified.

To enhance the hardness behavior of the samples, each one of them was subjected to three different post-fabrication heat treatment routes based on the 17-4 PH usual H900 treatment. The obtained results demonstrated that a direct aging route can be successful in enhancing the hardness of the material by taking advantage of the level of saturation of the hardening elements induced by the rapid cooling in L-DED process. When the samples were subjected to a direct aging treatment for 180 min without performing the austenitizing phase, the highest increase in hardness (481 ± 9 HV0.05) was established. Data scatters were also

significantly results with respect to the as-fabricated condition, because of a more homogeneous microstructure obtained with the heat treatment.

The optimal process conditions studied in the first part of this research were then used to perform and characterize multilayer depositions, and samples with high density up to 98.32 % were fabricated.

It is important to mention that the preliminary studies performed on single-tracks have been fundamental to find the suitable process conditions to be used in the subsequent quite full dense L-DED multilayers.

4.1.1 Future work

Although the obtained results are comforting, additional investigations need to be carried out to optimize the process parameters, to further reduce the defects and to improve the material properties. In light of this, the research work is still ongoing; process parameters and obtained results will be deeply studied by optimization tools such as neural networks.

Moreover, other heat treatment routes are under investigation on the multilayer depositions, together with ball-on-disk tests, in order to study the combined effect of process and post-fabrication heat treatments parameters on the wear behavior of these L-DED multilayers, considering the as-built condition as a reference.

As concerns microstructural analysis, EBSD and TEM investigations will be scheduled to validate the results discussed in the present doctoral thesis.

4.2 WC-CO L-DED DEPOSITIONS

Different Laser-based DED samples of WC with 12 % Co powders were deposited according to selected values of the powder feed rate and the scanning strategy and using two different steel plates as substrate.

In the first part of this study, samples were fabricated using a low carbon C4 steel and an HSS 390 steel combined with two different process conditions. The presence of pores and, even worst, of cracks was immediately noticed by macrostructural analysis of the deposited layers, as an effect of the laser power when the low carbon steel was used as substrate. This behavior was directly ascribed to the different coefficients of thermal expansion between the steel and the cermet. The high internal stresses generated at the interface between the substrate and the deposited material due to the process high cooling rates were considered the most influencing factor for the widespread formation and development of cracks. The HSS 390 steel substrate, by reason of its lower coefficient of thermal expansion and so more similar to the one of the WC-12Co than the low carbon steel, was effective in reducing the number of cracks.

Likewise, the microstructural inspection of the samples confirmed that when both the laser energy and the energy density parameter were lower, the microstructure was finer within the Co matrix, full of gray herringbone η-phase carbides and a high quantity of polygonal WC grains. This microstructural homogenization also promoted an increase in the hardness values (1150-1350 HV0.2).

Based on the results obtained in the first part of the study, research was then focused on the deposition of L-DED multilayers employing two different process conditions and three different scanning strategies. Moreover, ever according to previous results, only the 390 HSS steel was used as substrate.

Samples fabricated with the CLAMIR pattern strategy showed higher homogeneity in terms of defects, with still presence of pores but of lower size. The microstructure changed with the process conditions, accordingly. Low power laser with CLAMIR as scanning strategy permitted to obtain fine microstructural features. In this case, fine polygonal WC grains and lower-size herringbone carbides were found in the center and in the top zones of the deposition, so improving the hardness of the material up to 1400 HV0.2.

4.2.1 Future work

In this research with WC-Co depositions revealed that its low coefficient of thermal expansion could be a limiting factor for the deposition of hard-facing coatings by L-DED over several substrates. Nevertheless, new process parameters coupled with the CLAMIR scanning strategy will be investigated, strictly considering the physical properties of the substrate. Currently, a study on the effect of post-fabricating hard-facing heat treatments is ongoing. Even though the heat treatments cannot solve the problems of cracking occurring during the rapid solidification in L-DED, they can mitigate the negative effect on residual stresses and improve the hardness.

The following general conclusion can be drawn from this doctoral thesis:

- 17-4 PH stainless steel and WC-12Co can be 3D printed by the L-DED process.
- In both cases, the selection and management of the laser power and laser density energies are highly important to control the defects and the microstructural features, by which the mechanical properties of the L-DED depositions are mainly affected.
- As concerns the microstructural features and hardness values, satisfying results were obtained, even if better process parameters need to be designed in order to reduce defects, such as porosity and cracking phenomena.
- The performed post-fabrication direct aging seems to be promising in enhancing the microstructural and the mechanical processing of the 17-4 PH steel, highlighting and confirming that conventional treatment routes are not often so effective for additively manufactured materials.